DISSERTATION

HIGH RESOLUTION OPTICAL ANALYSIS OF NAV1.6 LOCALIZATION AND TRAFFICKING

Submitted by

Elizabeth Joy Akin

Graduate Program in Cell and Molecular Biology

In partial fulfillment of the requirements

For the Degree of Doctor of Philosophy

Colorado State University

Fort Collins, Colorado

Fall 2015

Doctoral Committee:

Advisor: Michael Tamkun
Co-Advisor: Gregory Amberg

Santiago Di Pietro
Diego Krapf
Susan Tsunoda

Copyright by Elizabeth Joy Akin 2015

All Rights Reserved

ABSTRACT

HIGH RESOLUTION OPTICAL ANALYSIS OF NAV1.6

LOCALIZATION AND TRAFFICKING

Voltage-gated sodium (Na_v) channels are responsible for the depolarizing phase of the action potential in most nerve cell membranes. As such, these proteins are essential for nearly all functions of the nervous system including thought, movement, sensation, and many other basic physiological processes. Neurons precisely control the number, type, and location of these important ion channels. The density of Na_v channels within the axon initial segment (AIS) of neurons can be more than 35-fold greater than that in the somatodendritic region and this localization is vital to action potential initiation. Dysfunction or mislocalization of Na_v channels is linked to many diseases including epilepsy, cardiac arrhythmias, and pain disorders. Despite the importance of Na_v channels, knowledge of their trafficking and cell-surface dynamics is severely limited. Research in this area has been hampered by the lack of modified Na_v constructs suitable for investigations into neuronal Na_v cell biology.

This dissertation demonstrates the successful creation of modified $Na_v1.6$ cDNAs that retain wild-type function and trafficking following expression in cultured rat hippocampal neurons. The $Na_v1.6$ isoform is emphasized because it 1) is the most abundant Na_v channel in the mammalian brain, 2) is involved in setting the action potential threshold, 3) controls repetitive firing in Purkinje neurons and retinal ganglion cells, 4) and can contain mutations causing epilepsy, ataxia, or mental retardation. Using single-molecule microscopy techniques, the trafficking and cell-surface dynamics of $Na_v1.6$ were investigated. In contrast to the current

dogma that Na_v channels are localized to the AIS of neurons through diffusion trapping and selective endocytosis, the experiments presented here demonstrate that $Na_v1.6$ is directly delivered to the AIS via a vesicular delivery mechanism. The modified $Na_v1.6$ constructs were also used to investigate the distribution and cell-surface dynamics of $Na_v1.6$. Somatic $Na_v1.6$ channels were observed to localize to small membrane regions, or nanoclusters, and this localization is ankyrinG independent. These sites, which could represent sites of localized channel regulation, represent a new Na_v localization mechanism. Channels within the nanoclusters appeared to be stably bound on the order of minutes to hours, while non-clustered $Na_v1.6$ channels were largely mobile. Novel single-particle tracking photoactivation localization microscopy (spt-PALM) analysis of $Na_v1.6$-Dendra2 demonstrated that the nanoclusters can be modeled as energy wells and the depth of these interactions increase with neuronal age.

The research presented in this dissertation represents the first single-molecule approaches to any Na_v channel isoform. The approaches developed during the course of this dissertation research will further our understanding of $Na_v1.6$ cell biology under both normal and pathological conditions.

ACKNOWLEDGEMENTS

This journey would not have been possible without the endless support of family, friends, and colleagues. Thank you so much to my mentor, Mike Tamkun, for the constant support through the past years. It was a privilege to be able to follow in your footsteps and contribute to the field of Na_v channels. From difficult experiments in the lab to rigorous backpacking escapades to building an igloo, this has been a true adventure. Thank you for taking a risk with both me and my project. Your immense knowledge and willingness to push the boundaries of science are inspiring. I could not be where I am today without such a great role model and mentor, and for that I will be forever grateful. Thank you to my committee members, Greg Amberg, Susan Tsunoda, Diego Krapf, and Santiago Di Pietro. I appreciate your support, great ideas, and for pushing me to always do better. Thank you for taking the time to invest in my graduate training.

My fellow Tamkunites, how can I say thank you? You have made my time in Fort Collins absolutely unforgettable. Phil Fox, thank you for putting up with my silly questions and mistakes over the years, and for remaining a source of wisdom and insight. I truly value our friendship and am grateful for our many conversations about science and life. I also learned to never underestimate the value of some good duct tape and pocket food. Laura Solé, llámame, possible? It is an incredible blessing to have such a friend and colleague. Thank you for taking on the difficult challenge of continuing the Na_v project. I look forward to many more good times together, both here and in Catalonia. Ben Johnson, Ashley Leek, and Emily Maverick, you are all incredibly talented scientists and I am excited to see where your journeys take you. Keep saving the world, banishing ghosts, and exploring The House on the Hill. We are all counting on you.

And remember, don't blink! Aubrey Weigel, as an honorary Tamkunite, thank you for remaining such a good friend despite the miles, and for all the Beers, Bears, and Science. Yaping Moshier, Rob Loftus, Chris Haberkorn, Emily Deutsch, Michaela Schumacher, Tracie VanHorn, Jason Platt, and all the others who have spent time in the Tamkun Lab, thank you for an amazing journey made rich by each of you. To all Tamkunites present and future, above all else make sure you keep the tiki torch! Thank you to Albert Gonzales for the steadfast support, insight, and many volleyball tournaments. To all those that made my graduate career so amazing, Krystle Frahm, An Dang, Mallory Shields, Christina Dennison, Max Vallejos, Ryan Tooker, Reagan Pennock, and so many others that I do not have space to mention.

To the Krapf Lab, Diego Krapf, Sanaz Sadegh, Eric Xinran Xu, and Jenny Higgins, thank you for sharing your expertise on all things biophysics. I would be lost without your help and I have learned an immense amount from all of you. Thank you to our collaborators, Steve Waxman and Sulayman Dib-Hajj for the $Na_v1.6$ clone to start my project, and for the advice and support through the arduous journey of publishing.

None of this would have been possible without the tireless encouragement of my family. Thank you to my mom, Nancy Akin, for being an unwavering pillar of support and love. Thank you for instilling in me the courage to overcome all obstacles. Thank you to my dad, Dave Akin, for kindling a sense of curiosity in me and an awe of nature. Thank you for teaching and coaching me through the years. Both of you have pushed me to follow my dreams and always believed in me, and I certainly would not have made it this far without you. To Andrew Akin, my brother and friend, thank you for being such a great role model and inspiration. No one could ask for anyone better to share growing up with. Thanks to both you and Mr. Douglas for help with the dissertation writing. Jeff and Aimee Jensen, my adopted parents, I cannot even begin to

express my gratitude for sharing this journey with me. Thank you for sharing your home, pets, food, cars, and love with me. It was above and beyond what anyone could ask for and is a testament to the amazing people you are. To my Grandma Dorothy for starting the tradition of education in our family, I love you and miss you dearly. Uncle Don Akin, thank you for being such an inspiration. You showed that it is possible to live life completely and selflessly, and that it is important to always be present for those you love. I will miss your jokes, but am glad I inherited your determination to never back down from a challenge. To all my grandparents, aunts, uncles, and cousins, thank you for being such an amazing family and for your support.

DEDICATION

In loving memory of Dorothy Dunn Durham (1926-2013)

and Donald Ray Akin (1947-2015).

TABLE OF CONTENTS

Chapter 1

Introduction

1.1 Excitable Membranes

Electrical Signaling

Mammalian cells maintain an internal environment of high potassium (K^+) and low sodium (Na^+) concentrations relative to the external environment, maintained by the hydrophobic plasma membrane (PM) encompassing the cell. These ion gradients are established by transmembrane proteins embedded into the PM, such as the sodium-potassium ATPase that uses energy to pump potassium ions into the cell and sodium ions out. The membrane is selectively permeable to potassium at rest, which establishes a negative membrane potential in relation to the external environment in most cells. Electrically excitable cells such as nerve and muscle cells are specialized such that they can alter their relative permeability to these ions on a millisecond timescale, synchronously altering the membrane potential of the cell. The electrical messages, or action potentials, that neurons use as their major form of intercellular communication are precisely orchestrated changes in ion permeability that create spatially and temporally controlled electrical currents. (Hille, 2001)

The key to the action potential, and thus to a considerable amount of physiology, is the voltage-gated sodium (Na_v) channel. The concerted opening of these channels within the axon initial segment (AIS), the neuronal axon proximal to the soma, creates a transient (1-2ms) influx of sodium that provides the depolarizing current of the action potential (Fig. 1.1). A slower activating potassium efflux serves to repolarize the nerve membrane, bringing it back towards

Nernst equilibrium for potassium. The propagation of this signal down the axon is dependent on the ability of the neuronal membrane to act as an electric cable such that the localized depolarization can spread passively to nearby regions where it can initiate the active response of the voltage-gated ion channels present in adjoining membrane, and thus propagating the signal. (Hille, 2001)

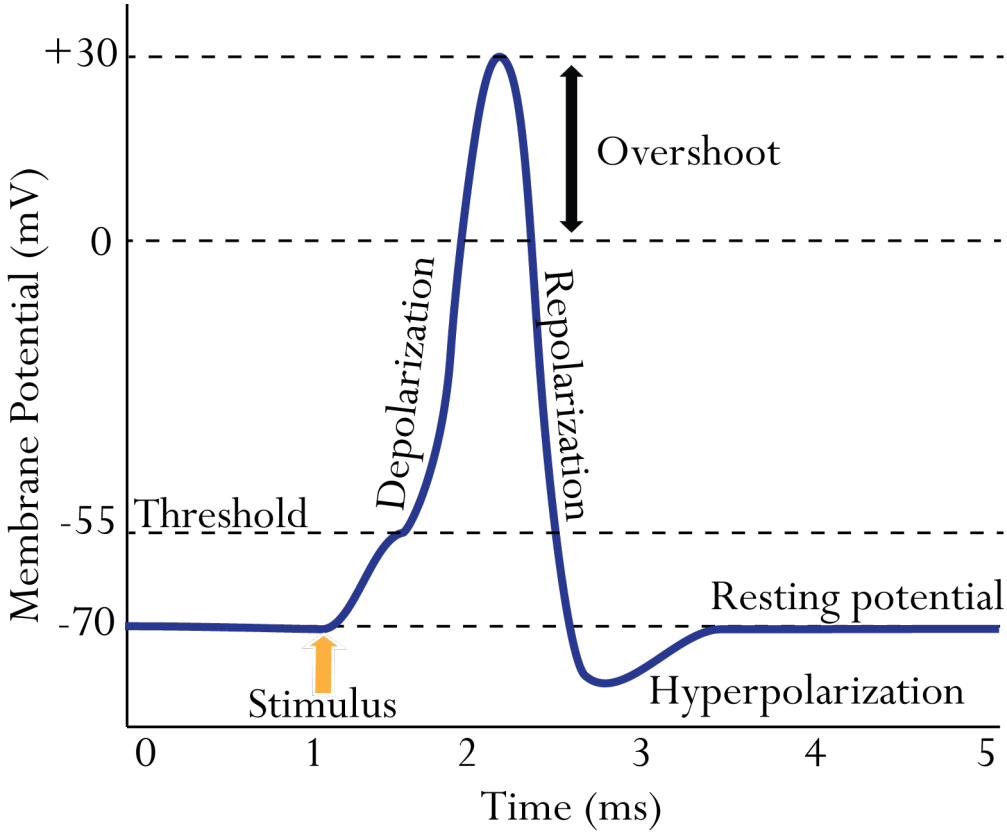

Figure 1.1. Action potential waveform.

The typical nerve cell generally has a resting membrane potential of approximately -70mV. When a stimulus is applied that increases the membrane potential above the threshold, voltage-gated sodium (Na_v) channels open. The influx of Na^+ through the channels underlies the depolarization phase of the action potential. Na_v channels have both fast activation and fast inactivation. Voltage-gated potassium channels (K_v) activate to repolarize the membrane potential. Slow closing of the K_v channels can cause the membrane potential to reach close to Nernst equilibrium for K^+, which is often at a voltage below the resting membrane potential and results in hyperpolarization. The increase of the membrane potential past 0 mV, or the overshoot, provided evidence that the membrane potential is selectively permeable to Na^+ ions during the rising-phase of the action potential.

This current understanding of electrical signaling is based on over a century of discovery in which the basic principles of the plasma membrane, electric potential, and, crucially, the identity of ion channels were established.

A Historical Perspective

As early as the late 1800s, it was understood that ions are a critical component of nerve and muscle function. Notably, Sidney Ringer demonstrated using experiments on frog hearts that sodium, potassium, and calcium (Ca^{2+}) ions are essential for heart function (1881-1887). Additional contributions included evidence that cells contain a bioelectric potential (Nernst, 1888) established by separation of charge, and that permeability to potassium over other ions sets the resting membrane potential (Bernstein, 1902, 1912). Julius Bernstein conjectured that excitation was dependent on an increased permeability of the PM to other ions and proposed a mechanism of "membrane breakdown" whereby the PM itself undergoes a change to allow the passage of ions. At the time, there was quite a bit of resistance to these kinds of ideas as the identity, and even the presence itself, of the PM was uncertain and there was debate as to whether the membrane was entirely separate from the cytoplasm. (Behrends, 2012)

Howard Curtis and Kenneth Cole (1939) sought to test Bernstein's hypothesis of membrane breakdown and, while confirming the increase in membrane conductance during an action potential, noted that the capacitive aspect of the membrane, which can be considered a measure of membrane integrity, showed almost no change (Cole and Curtis, 1939). Thus, they correctly conjectured, the increase in ionic permeability was due to a localized phenomenon rather than extensive membrane breakdown. Another major breakthrough occurred when it was discovered that the squid giant axon was of ample size to allow the intracellular insertion of a

micropipette, which enabled the measurement of the first full action potential. This showed, surprisingly at the time, that the depolarizing phase of the action potential did not stop at 0 mV as predicted by a general membrane breakdown, but rather surpassed it by tens of millivolts. These observations were made nearly concurrently by the Americans, Curtis and Cole, and their British counterparts, Alan Hodgkin, Andrew Huxley, and Bernard Katz. It was, however, the group in Cambridge that was able to decipher that this overshoot was due to selective permeability to sodium ions thereby changing the membrane potential towards that of sodium equilibrium. They demonstrated that sodium flux is the key component of the axon potential in further experiments where they decreased the concentration of sodium ions in the extracellular solution and showed a decrease or removal in the overshoot and a delay in the onset of the nerve impulse in a concentration dependent manner. In a transatlantic collaboration, Cole, Curtis, Hodgkin, Huxley, Katz and others developed the pioneering technique of voltage-clamp to measure ionic current at known membrane potentials. Using this technique they were able to demonstrate that the axon potential is carried by two major, independent components consisting of a transient inward Na^+ current and a slow-onset outward K^+ current. The series of papers published by Hodgkin and Huxley in 1952 describing these voltage-clamp experiments formed the basis for the ionic theory of membrane excitation, which asserts that electrical signals are formed by changes in permeability to ions (Hodgkin and Huxley, 1952a; Hodgkin et al., 1952; Hodgkin and Huxley, 1952b, c). This revolutionized neuroscience, providing many of the key concepts still used today. Incredibly, they were able to develop equations to describe and model action potentials with astounding accuracy based on the relative permeability of the neuronal membrane to sodium and potassium ions, as well as describe many of the characteristics of the

mechanism responsible for sodium flux including the time course of inactivation and voltage dependence.

Sodium permeation pathway

Understanding of the ionic basis of the action potential began the search for the pathway by which ions cross the membrane. At the time, it was known that the mechanisms for ion permeation must respond to membrane voltage, must be selective for different ions, and must not affect overall membrane structure. In their 1949 paper describing sodium as the major depolarizing ion, Hodgkin and Huxley first imagined sodium ions bound to charged carrier molecules that could only pass through the membrane when the membrane potential was depolarized (Hodgkin and Katz, 1949). In their 1952 experiments, they found this theory incompatible with their data and equations and subsequently predicted ion selective passageways through the membrane whose activity was gated by charged particles (Hodgkin and Huxley, 1952a). However, the molecular identity of these passageways remained elusive for several more decades. In the meanwhile, many different theories emerged spanning from ideas of lipid-lined pores present in the plasma membrane itself, to the idea of transmembrane proteins with water filled passageways.

The discovery that specific toxins and inhibitors act to alter individual ionic currents provided key insights into the method of ion permeation. First, the ionic permeation pathways could be separated pharmacologically such that the Na^+ current could be removed via toxins such as tetrodotoxin (Narahashi et al., 1960; Narahashi et al., 1964; Nakamura et al., 1965) and the K^+ current could be removed with the addition of tetraethylammonium (TEA) (Hille, 1967), each without affecting other ionic currents. This strongly supported the idea of distinct pathways with

components containing different chemical structures, and suggested spatial separation of these components as well. Second, Bertil Hille demonstrated that both TEA and TTX had an effect in a dose-dependent manner that indicated a one-to-one interaction, indicating binding to a specific receptor (Hille, 1967, 1968). Studies into which ions permeate the pore provided insight into the proposed selectivity filter for the channel. Based on the size and molecular structure of permeable and non-permeable ions suggested a pore size of approximately 3A by 5A in cross-section (Hille, 1971, 1972).

Despite these data, the idea of a single conduction pathway persisted into the early 1970s. During an axon potential the outward potassium current starts at the point when the inward sodium current diminishes, sparking the idea that these two currents were two phases of the same molecule. To address this, Rojas and Armstrong (1971) were able to remove Na^+ channel inactivation by perfusing squid giant axons internally with pronase, an unspecific proteolytic enzyme. The removal of Na^+ channel inactivation increased the overall membrane conductance (ROJAS and ARMSTRONG, 1971). If the Na^+ and K^+ currents were linked within the same molecule, alterations to one conduction pathway would alter both. Thus, these experiments supported the hypothesis that these ions flow through distinct pathways, as well as demonstrating that sodium current is dependent on a protein, although the specifics were still uncertain. Soon after, the gating current associated with the voltage sensor was measured (Armstrong and Bezanilla, 1973, 1974) which agreed with Hodgkin's and Huxley's predication of charged particles that move in response to changes in membrane potential as the activation gates for Na^+ current. This was accomplished by using drugs to remove all ionic currents and subtracting leaking and capacitive currents, giving enough sensitivity to see the gating currents.

Sodium influx through individual channels was observed using the newly pioneered cell-attached voltage-clamp technique on rat myocytes, which demonstrated discrete transitions from open to closed states of the channel. The single channel conductance was estimated to be approximately 18 pS (Sigworth, 1980). This translates into approximately 10^7 ions/sec, which is much faster than the rate of an ion carrier (10^4 ions/sec) and predicts an ion channel. By measuring the kinetics of channel activation and inactivation of single channel recordings, it was determined that Na_v inactivation is linked to its activation such that the channel must be activated before inactivation can occur (Aldrich et al., 1983). This differs from the ideas of Hodgkin and Huxley that channel activation and inactivation were independent processes.

Sodium channel as a protein

Together, these experiments predicted an integral membrane protein that formed an ion-conducting channel, gated by voltage. However, the identity of the sodium channel was not discovered until the early 1980s, nearly three decades after the establishment of the ionic theory of membrane excitation. William Catterall and Daniel Beneski (1980) were able to purify the sodium channel using photoactivatable covalent labeling of the channels with modified ^{125}I-labled scorpion toxin (Beneski and Catterall, 1980). They found three polypeptides, a large α subunit (260 kDa) and two β subunits (30-40 kDa) that consisted of a non-covalently associated β1 and a disulfide-linked β2 (Hartshorne and Catterall, 1981; Hartshorne et al., 1982; Hartshorne and Catterall, 1984). Isolation of these polypeptides did not confirm that they represented the entire, functional voltage-gated ion channel. In order to demonstrate this, purified protein from rat brain was reconstituted into phosphatidylcholine vesicles. These experiments demonstrated that the purified saxitoxin receptor was sufficient for selective sodium channel flux. These reconstituted proteins demonstrated voltage-sensitivity, single channel conductance, and

pharmacology nearly identical to the native sodium channel, and thus represented the entirety of the voltage-gated ion channel (Talvenheimo et al., 1982; Tamkun et al., 1984; Hartshorne et al., 1985). During a similar timeframe, the sodium channel was purified from the electric eel (Agnew et al., 1980) and from skeletal muscle (Barchi, 1983).

Cloning of sodium channels

Purification of the sodium channel protein enabled cloning of the channel and analysis of the nucleic acid structure. Short peptide sequences were identified from sodium channel isolated from the electroplax of *El. electricus*, enabling screening of cDNA clones (Noda et al., 1983). Identification of the full-length nucleotide sequence revealed a 7,230-nucleotide sequence. Several striking features of the sequence allowed a remarkable prediction of the overall sodium channel structure, including the presence of four repeated units, each containing a region of nearly evenly spaced positive residues that could serve as the predicted voltage-sensor. Cloned cDNA injected into Xenopus oocytes elicited sodium current, demonstrating that the α subunit alone is sufficient for Na^+ conduction (Noda et al., 1986a). Similar nucleotide sequences were found in other tissues, including two different clones from rat brain (Noda et al., 1986b). Before the turn of the century, ten genes encoding the sodium channel alpha subunit were identified (Goldin, 2001). Expression in heterologous systems and mutagenesis techniques then began a new era of understanding channel structure/function.

1.2 Structure/Function of Voltage-Gated Sodium Channels

Our current understanding of voltage-gated sodium channels based on the last sixty years of experiments was recently confirmed and expanded when a high-resolution (2.7 A) crystal structure was obtained of the bacterial sodium channel, NavAb (Payandeh et al., 2011). This

channel is a homotetramer in contrast to the more complicated homomers of its mammalian counterparts, facilitating the crystallization process. This section outlines our current understanding of Na_v channel structure and function.

Alpha subunit

Voltage-gated sodium channels are composed of a pore-forming alpha subunit and regulatory beta subunits. Nine similar alpha subunits have been discovered and defined as a superfamily and the nomenclature of $Na_v1.x$ was adopted by the International Union of Pharmacology according to the primary permeating ion, Na^+, followed by the primary regulator of channel activity, voltage, followed by the family and isoform. Other superfamilies such as voltage-gated potassium channels have several families based on sequence similarities, however the amino acid sequence of mammalian Na_v channel isoforms are all more than 50% identical and are classified within a single family ($Na_v1.1$-$Na_v1.9$) (Catterall et al., 2005). While members of the other families within the voltage-gated ion channel superfamily, Ca_v and K_v channels, have a variety of different waveforms, all nine isoforms of the Na_v family have remarkably similar waveforms that are characterized by fast activation followed by fast inactivation. The subtle differences between the isoforms include the voltage-dependence of activation and inactivation. A tenth channel with similar structure, Nax, has been shown to be involved in salt regulation (Hiyama et al., 2002), although it seems to be lacking properties such as voltage-sensitivity.

The α-subunit is the principle subunit, both necessary and sufficient for sodium conductance. It is a large, 260 kDa transmembrane protein (approximately 2000 amino acids) organized into four repeating domains (I-IV), each composed of six transmembrane segments (S1-S6). It has a central pore surrounded by the S5-S6 segments from each domain with S6

lining the intracellular portion of the water-filled cavity. The pore region is surrounded by the S1-S4 segments (Fig. 1.2A). The crystal structure shows that there is a domain-swapping arrangement such that the voltage-sensing domain is associated with the pore-forming module of

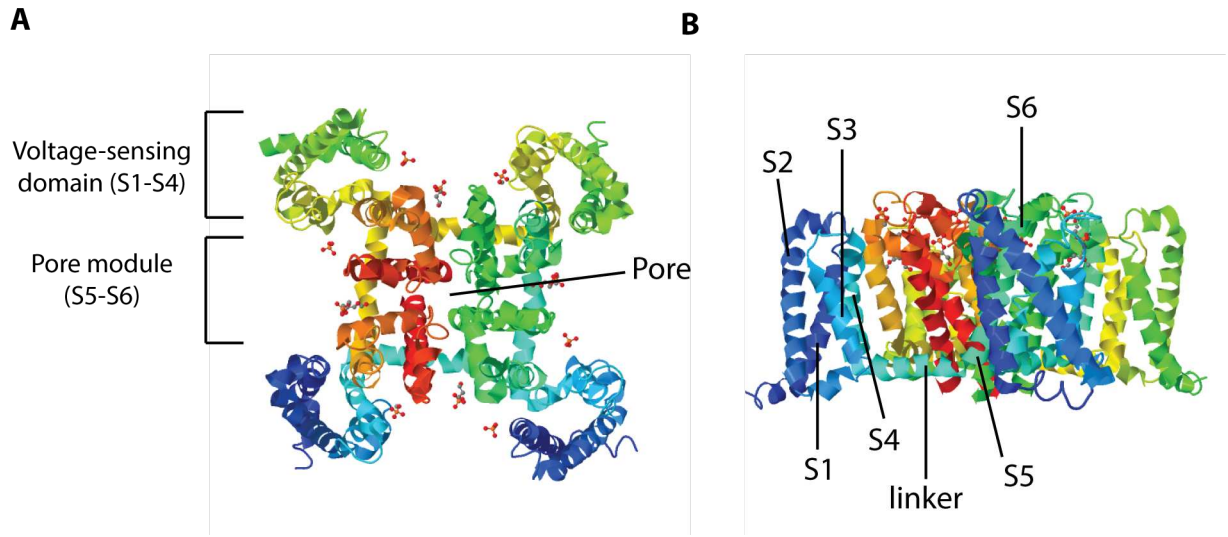

Figure 1.2. Crystal structure of NavAb.

A) Top view of the bacterial Na_v channel crystal structure. The voltage-sensing domain composed of the S1-S4 segments is located peripherally to the pore module. The S4 segment contains charged amino acids and is the voltage-sensor. The S5-S6 segments, as well as the P-loop between them, form a central pore that opens in response to depolarization. **B)** Side view. The voltage-sensing domain is associated with the pore module of the neighboring domain in a domain-swapping arrangement. Movement of the S4 segment is conferred to the pore module through the S4-S5 linker for activation of the channel. (Crystal structures were created using RCSB Protein Database based on structural data from Payandeh et al., 2011).

the neighboring domain (Fig. 1.2B) (Payandeh et al., 2011). Interestingly, lipids potentially penetrate the central cavity of the channel through fenestrations in the wall of the pore module, which could explain the access point for some drugs and anesthetics.

Selectivity filter

The selectivity filter that permits sodium entry over other ions is formed via a reentrant loop (p-loop) from the extracellular end of the S5-S6 contributed by each domain. The key

amino acids of the selectivity filter are DEKA (domains I-IV). Interesting, this can easily be mutated into a calcium permeant pore through a single point mutation where the K in domain III is mutated to an E to mimic the Ca_v selectivity filter (Heinemann et al., 1992). The crystal structure elucidates that there is large extracellular vestibule, which narrows down to the ion selectivity filter, then reopens to a central cavity bounded by the activation gate. Na^+ molecules move through the selectivity filter in a mostly hydrated form such that the Na^+ ion is surrounded by a square array of water molecules in contrast to K^+ ions that move through K_v channels nearly fully dehydrated (Payandeh et al., 2011). As a testament to the rigorous studies of the preceding decades, this is in good agreement with the ideas proposed by Bertil Hille based on ion permeation studies in the 1970s (Hille, 1975).

Voltage-sensor

The S1-S4 is considered the voltage-sensing region, with the transmembrane S4 segment containing 4-7 repeats of a positively charged amino acid followed by two hydrophobic residues. This aligns with the model predicted by Hodgkin and Huxley of "electrically charged particles" to gate channel activity. The prevalent model for S4 movement is the sliding helix model. At rest, the positive residues are stabilized by interactions with negative residues. During depolarization, as the inner environment becomes more positive and thus repulsive to the voltage sensor, the negative interactions are exchanged for a new set of interacting partners as the S4 segments rotate and move towards the extracellular region (Catterall, 2010). This model has been supported by both the Na_vAb crystal structure, caught in the activated but pore-closed conformation, and by disulfide linkage studies (DeCaen et al., 2008; DeCaen et al., 2011). This in turn causes a conformation change in the pore region which opens the channel and allows sodium flux. The structure showed that, similar to what was observed for potassium channel

structures, the S4-S5 linkers pivot around a hinge at the base of the pore, which dilates and opens the pore.

Inactivation gate

Na_v channels quickly inactivate after activation, ensuring cessation of the rising phase of the action potential and facilitation of repetitive firing. Fast inactivation of Na_v channels is mediated by the intracellular loop between domains III-IV. The key amino acid motif is IFM (West et al., 1992), part of a structure hinged on a pair of glycine residues that folds into and binds the pore upon channel activation, blocking ion flux as a hinged lid (Kellenberger et al., 1996; Kellenberger et al., 1997a; Kellenberger et al., 1997b). Addition of peptides containing the IFM motif can restore fast inactivation to channels in which the channel inactivation gate has been mutated (Eaholtz et al., 1994).

Beta subunits

Na_v α subunits are generally complexed with one or more small, regulatory β subunits. For mammals there are 5 different subunits. β 1- β 4 are type-1 proteins with a single transmembrane domain, a small intracellular C-terminus, and a large extracellular N-terminus containing an immunoglobulin (Ig) loop. β 1B is a splice variant of β 1 that does not contain a transmembrane domain and is thus a soluble protein. Complexes with the α subunit are either through a disulfide linkage (β 2/ β 4) or non-covalently (β 1/ β 3). All of the β subunits are able to modify the activity of α subunits through changes in gating or kinetics such as activation kinetics or voltage-dependent activation. These modifications are cell-type specific and depend on the α and β isoforms present. (Brackenbury and Isom, 2011)

Tissue specific expression

The Na_v α subunit isoforms are expressed in different tissues. The major isoforms of the central nervous system (CNS) are $Na_v1.1$, $Na_v1.2$, $Na_v1.3$ and $Na_v1.6$. $Na_v1.4$ is the major isoform in skeletal muscle and $Na_v1.5$ is the primary isoform found in cardiac tissue. $Na_v1.6$, $Na_v1.7$, $Na_v1.8$, and $Na_v1.9$ are found in the dorsal root ganglion (DRG) (Goldin, 2001). These are generalized distributions, with small amounts of each isoforms found in a variety of tissue types. The expression of the various isoforms is also regulated during development. In some neurons, $Na_v1.2$ is expressed early in development but is later replaced by $Na_v1.6$ as the cell matures (Kaplan et al., 2001).

Importance of Na_v research

Voltage-gated sodium channels provide the rising phase of the action potential in most neurons. As such, mutations, altered expression, or, of major relevance to this dissertation, mislocalization and altered trafficking of these channels, often lead to disease. Na_v channels have been implicated in epilepsy (Meisler and Kearney, 2005; Catterall et al., 2010), chronic pain (Dib-Hajj et al., 1999; Amir et al., 2006; Cummins et al., 2007; Dib-Hajj et al., 2010), multiple-sclerosis (Craner et al., 2004; Waxman, 2006), movement disorders (Hamann et al., 2003), and many more disease states. Their location as integral membrane proteins makes them accessible to drugs, and as regulators of neuronal output, Na_v channels are often drug targets for a variety of pain (Dib‐Hajj et al., 2009) and anti-epileptic drugs (Catterall, 1987).

The subcellular localization of Na_v channels is tightly regulated and mislocalization contributes to disease. For example, some forms of epilepsy are caused by Na_v channel trafficking or localization defects (Wimmer et al., 2010b; Wimmer et al., 2010a). Neuronal

dysfunction after ischemic injury is contributed to by loss of appropriate Na^+ channel localization to the axon initial segment (Heinemann et al., 1992; Schafer et al., 2009), implicating that prevention of this relocalization could be a future treatment for stroke. The length and molecular composition of the AIS is remodeled following traumatic brain injury (Masel et al., 2012) and Na_v channel blockers have been demonstrated to be neuroprotective in models of central nervous system trauma (Morris et al., 2012). Together these studies highlight Na_v channels and their localization to the AIS as targets for therapeutic treatments.

1.3 $Na_v1.6$

This dissertation explores the cell biology of $Na_v1.6$. $Na_v1.6$ is encoded by the gene Scn8a, which was identified in the rat by the Caldwell lab (Schaller et al., 1995) and in mouse by the Meisler lab (Burgess et al., 1995). In humans it is present on chromosome 12q13 (Plummer et al., 1998). The $Na_v1.6$ isoform is of particular interest for several reasons. It is widely expressed in the central nervous system, demonstrates distinctive subcellular distributions in neurons, displays unique biophysical characteristics, is functionally regulated by a variety of proteins, and is implicated in a wide battery of pathologies.

Tissue expression

$Na_v1.6$ is widely expressed in the mammalian nervous system. It is expressed in hippocampal pyramidal and granule cells, motor neurons of the spinal cord and brain stem, axons in the retina, and dendrites or cerebral cortical pyramidal cells (Schaller et al., 1995). In the cerebellum it is localized to Purkinje cells, granule cells, parallel fibers, and to lesser extent in other neurons such as the molecular layer (Caldwell et al., 2000). $Na_v1.6$ has also been found in glial cells such as astrocytes and Schwann cells (Schaller et al., 1995). It is also the major Na_v

isoform at nodes of Ranvier and a minor contributor to cardiac currents and DRG neurons (Herzog et al., 2003; Rush et al., 2005; Du et al., 2007).

Subcellular localization

$Na_v1.6$ demonstrates a unique sub-cellular distribution within hippocampal neurons. It is localized at a high density within the AIS and nodes of Ranvier, but also with a lower density distribution within the somatodendritic region (Caldwell et al., 2000; Lorincz and Nusser, 2010). This localization enables initiation, propagation, and backpropagation of the action potential, respectively. The mechanisms underlying this differential distribution is not understood, nor understanding of compartment specific regulation of channel activity.

Biophysical Characteristics

$Na_v1.6$ shows unique biophysical properties. Whole cell currents of $Na_v1.6$ show a persistent current of approximately 10% of the total current, although this is cell type specific, demonstrating modulation by yet unknown factors (Rush et al., 2005). Persistent current is most likely due to lack of inactivation for a subset of the channels, again suggesting specific regulation of certain channels. It seems to be important for action potential initiation at membrane potentials near the threshold of firing, and thus are important in neurons that undergo repetitive firing (Crill, 1996). Pathologically enhanced persistent current leads to neuronal hyperexcitability and epilepsy (Veeramah et al., 2012). Interestingly, interactions with ankG may decrease $Na_v1.6$ persistent current (Shirahata et al., 2006).

$Na_v1.6$ also displays resurgent current. This is when a secondary depolarization after the initial event elicits a small, transient current. This could lead to increased neuronal excitability,

and has been proposed to be involved in multi-peak action potentials in Purkinje cells. Again, this property is cell-type specific (Raman et al., 1997).

$Na_v1.6$ interactions and regulation

$Na_v1.6$ has a variety of identified binding partners involved in channel trafficking, subcellular localization, and modulation of biophysical properties.

Map1b It was recently discovered that $Na_v1.6$ interacts with the light chain of microtubule associated protein Map1b via the N-terminal tail of $Na_v1.6$. Yeast 2-hybrid and pull-down assays suggest that the interaction is specific to the $Na_v1.6$ isoform. Evidence suggests that Map1b is involved in protein trafficking to the cell membrane since mutation of the putative Map1b binding site abolishes $Na_v1.6$ current and co-transfection of $Na_v1.6$ with Map1b increases the current by 50% (O'Brien et al., 2012). Map1b is expressed early in development where it helps with axon elongation and turning, and functions to stabilize the microtuble network.

Fibroblast Growth Factor Homologous Factors (FHF) Yeast-2-hybrid screens were used to identify fibroblast growth factor homologous factor (FHF) proteins as interacting partners with Na_v channels using the C-terminus of $Na_v1.6$ and $Na_v1.9$ as bait. The FHF family has four members (FHF1-4) that comprise an intracellular fibroblast growth factor (iFGF11-14) subfamily. In contrast to the other FGF family members, they are unable to interact with FGF receptors. They undergo alternative splicing of exon 1 such that the length of the N-terminus is varied, but the rest of the five-exon structure is similar. They all contain a conserved Na_v channel-binding surface that interacts with the Na_v C-terminus. Both the A and B isoforms of FHF2 and 4 have been identified to interact with $Na_v1.6$ with differing functional effects either

increasing or decreasing current density and depolarizing inactivation (Rush et al., 2006; Yan et al., 2014).

Mitogen Activated Protein Kinase (MAPK) One group of MAPKs, p38, is activated by inflammatory cytokines and environmental stress. $Na_v1.6$ and p38 are expressed within the same cells in rat brain and activated p38 phosphorylates $Na_v1.6$ at a single site, S553, within a PGSP motif in the L1 loop (between domains I and II). Phosphorylation causes a reduction in $Na_v1.6$ current density in the neuroblastoma cell line ND7/23 (Wittmack et al., 2005). This modification of $Na_v1.6$ activity could be involved in neuronal response to injury.

Neural Precursor Cell Expressed Developmentally Down-Regulated (Nedd) Related to p38 modulation of $Na_v1.6$ is Nedd4, which is part of the E3 ubiquitin ligase family. It requires phosphorylation of the aforementioned S553 residue in L1 as well as a PXY motif found in the C-terminus to effect a decrease in current density (Gasser et al., 2010). Thus, it is a multilevel form of channel regulation and suggests an interaction between the p38 and Nedd 4 pathways.

Protein Kinase CK2 This protein kinase has been shown to be concentrated within the AIS of neurons from the hippocampus and cerebellum, as well as at nodes of Ranvier (Bréchet et al., 2008). It phosphorylates $Na_v1.6$ at the highly conserved residue E1100 within the ankyrin-binding motif, thereby enhancing channel binding to ankyrin and stabilizing the interaction (Gasser et al., 2012). Strangely, CK2 and Na_v channel enrichments at the AIS seem to be interdependent such that loss of Na_v channel axonal localization or lack of CK2 phosphorylation prevents AIS localization of both proteins (Hien et al., 2014).

$Na_v1.6$ and disease

There are numerous mutations discovered in $Na_v1.6$ that are associated with human diseases. Furthermore, upregulation of $Na_v1.6$ expression after injury has been shown to contribute to subsequent pathologies.

Ataxia and epilepsy The first reported human mutation in Scn8a was found within a screen of 151 patients that presented with inherited or sporadic ataxia. This mutation carrying patient showed ataxia, cerebellar atrophy, and mental retardation, all of which was attributed to the presence of a premature stop codon in the pore-loop of domain IV, predicted to result in loss of function (Trudeau et al., 2006). A de novo mutation in Scn8a was discovered in a human patient suffering from severe epileptic encephalopathy, which presented itself with intellectual disability, autistic-like features, and early-onset seizures. It resulted in sudden, unexpected death in epilepsy (SUDEP). The mutation (N1768D) is at the base of the domain IV S6, is highly conserved across Na_v isoforms, and causes increased excitability through enhanced persistent current and impaired fast-inactivation (Veeramah et al., 2012). Two spontaneous mutations of Scn8a in mice that resulted in null mutations have been reported, $Scn8a^{med}$ and $Scn8a^{med\text{-}Tg}$. This loss of $Na_v1.6$ activity causes juvenile lethality, before which mice display a phenotype of paralysis and muscle atrophy (Burgess et al., 1995; Kohrman et al., 1996). It also results in ataxia, tremor, and prolonged cardiac action potentials (Noujaim et al., 2012). Other mutations cause minor tremor, ataxia, muscle weakness, and severe dystonia. The induced mutation $Scna8a^{ataxia3}$ has a similar phenotype to the null mutations, although the mice retain partial hindlimb function. Lack of channel function from this mutation has as been attributed to a trafficking defect in which the channel is retained within the Golgi complex (Sharkey et al., 2009).

Traumatic Brain Injury and Nerve Damage Increased expression of Na_v isoforms after injury has been implicated in chronic pain and may be a common mechanism of post-injury pathologies (Hains et al., 2003). In a fluid percussion traumatic brain injury model in adult rats, expression of $Na_v1.6$ was increased immediately following injury and protein levels remained elevated at 72 hrs post injury. This increase was localized to neurons within the hippocampus (Mao et al., 2010). In a model of hemisection injury of the spinal chord in adult rats, it was found that some axons were demyelinated and this was associated with a diffuse distribution of $Na_v1.6$ in contrast to the normally precise localization to nodes of Ranvier. This caused decreased excitability with a longer latency for action potential propagation (Hunanyan et al., 2011).

1.4 Axon Initial Segment

Neuronal action potentials originate in the proximal axon, the axon initial segment (AIS). The protein composition and architecture of this region are highly specialized, including a unique cytoskeletal architecture and vast complement of ion channels including Na_v channels (Boiko et al., 2003), K_v channels (Pan et al., 2006; Kole et al., 2007; Sarmiere et al., 2008), and extracellular matrix proteins such as Neurofascin (Jenkins and Bennett, 2001; Hedstrom et al., 2007) (See Fig. 1.3). Of principle interest to the current discussion is the high density of Na_v channels that provide the depolarizing stimulus for the action potential (Kole et al., 2008). In addition to its role of action potential initiation, the AIS has been defined as a molecular barrier that establishes neuronal polarity, namely the axonal versus somatodendritic regions (Rasband, 2010).

AIS structure

The intricate structure of the AIS is just starting to be unraveled with a diverse complement of proteins, unique to each type of neuron that shapes excitability and action potential properties. AnkyrinG (ankG), a cytoskeletal anchoring protein, is considered to be the "master organizer" of the AIS since lack of ankG prevents formation of this region, demonstrated both by lack of AISs in ankG knockout mice (Zhou et al., 1998; Jenkins and Bennett, 2001; Pan et al., 2006) and that knockdown of ankG in cultured neurons prevents axon formation (Hedstrom et al., 2007). It is also possible to disassemble an already established AIS via knockdown of ankG in a neuronal culture system, which confers dendritic properties onto the former axon such as accumulation of MAP2 and the formation of protrusions resembling dendritic spines (Hedstrom et al., 2008). In this way, ankG seems to be responsible for both establishing and maintaining the identity of the AIS. Its major function is as an anchoring protein within the scaffold that links integral membrane proteins to the actin cytoskeleton. On the intracellular side, it binds βIV-spectrin (Jenkins and Bennett, 2001; Yang et al., 2007; Susuki and Rasband, 2008), which in turn binds to the actin cytoskeleton, while on the membrane side it binds and localizes several classes of transmembrane proteins that contain ankG binding motifs, including Na_v channels, K_v channels and extracellular matrix proteins (Ango et al., 2004; Pan et al., 2006).

AIS assembly

Assembly of this unique region has been studied mostly through the paradigm of cultured hippocampal neurons as established by Gary Banker. (Dotti et al., 1988) Dissociated hippocampal neurons will extend several neurites upon plating, one (occasionally several) of

which, within hours, will begin to grow rapidly to become the axon while the rest to become dendrites. Neurons are able to develop an AIS in these culture systems, in contrast to nodes of Ranvier that require interactions with Schwann cells. Molecular components of the AIS, such as ankG, can be detected as early as three to four days in culture (Boiko et al., 2003). It is not

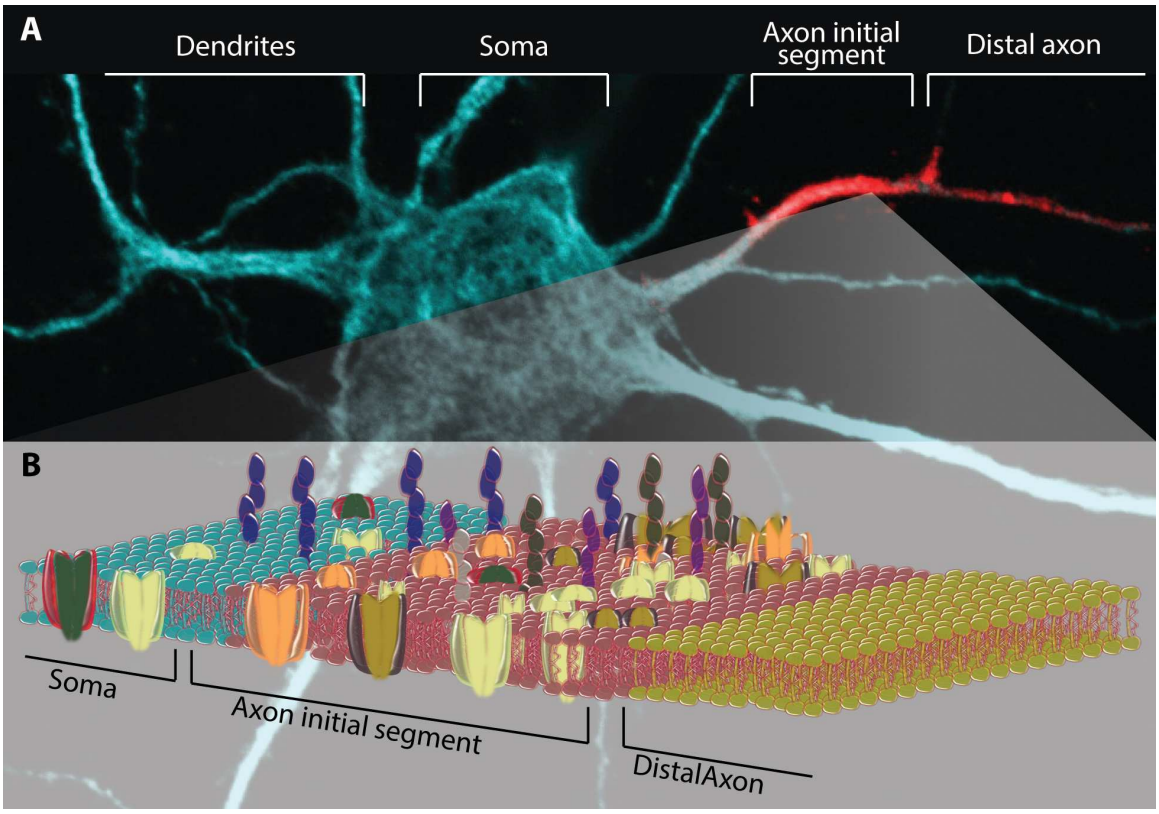

Figure 1.3. Neuronal architecture and molecular composition of the axon initial segment.

A) Neurons are polarized cells. Map2 (blue) is localized to the somatodendritic region while Na_v channels (red) are localized to the axon at a high density. The cell body, or soma, contains the nucleus. Dendrites extending from the cell body collect information from upstream neurons through synaptic connections. Signals are integrated within the proximal region of the axon, the axon initial segment (AIS). If signals are strong enough to generate an action potential, it is initiated in the AIS and then propagated down the distal axon. **B)** There is a high density of proteins within the AIS including Na_v channels, K_v channels and extracellular matrix proteins. The high density of Na_v channels is essential for action potential initiation and propagation.

completely known how ankG, as the AIS organizer, is recruited to the AIS where it then recruits its various binding partners. Part of the answer was discovered to be the formation of an intra-

axonal barrier where a different ankyrin isoform, ankyrinB, fills the distal portion of the axon and ankG subsequently fills in the more proximal region (Galiano et al., 2012). However, the signaling pathways and other mechanisms that ultimately regulate the formation of the AIS are just beginning to be understood. Despite containing a very similar molecular make-up to that of the AIS, nodes of Ranvier are formed by a very different mechanism. Neurofascin-186 is clustered by glia, where it then recruits ankG, which in turn clusters Na_v and K_v channels (Hedstrom et al., 2007).

Na_v localization and trafficking to the AIS

A high density of Na_v channels within the AIS is essential for axon potential initiation (Zhou et al., 1998; Kole et al., 2008). This localization is dependent on binding to ankG through a 9-amino acid ankG binding motif (ABM) located on the intracellular loop between domains II-III (LII-III) which consists of a 9-amino acid sequence (Garrido et al., 2003; Lemaillet et al., 2003). This motif interacts with ankG in pull-down assays (Lemaillet et al., 2003) and is sufficient to localize chimeric reporter proteins such as CD4, Neurofascin-186, and K_v2.1 to the AIS of cultured hippocampal neurons. Most importantly, the full-length Na_v1.6 protein with a fluorescent reporter was used to demonstrate that the ankyrin-binding motif is both necessary and sufficient to localize Na_v1.6 to both the AIS and nodes of Ranvier (Gasser et al., 2012). Interestingly, all nine of the Na_v alpha subunits identified to date contain a variation of the ankG-binding motif, including what have been demonstrated as the essential residues, although not all of them demonstrate ankG-binding (Gasser et al., 2012). A surprising finding by the Rasband Lab is that in ankG cerebellar knockout mice, the ankyrin isoform found most often in erythrocytes, ankyrinR, can substitute for ankG and cluster Na_v channels at nodes of Ranvier in

the CNS. While ankG usually binds BIV-spectrin, the switch to ankR was also accompanied with a switch to B1-spectrin (Ho et al., 2014).

The trafficking route to the AIS taken by Na_v channels after channel biosynthesis has not been fully elucidated. Initial studies used chimeric reporter proteins containing an ankyrin-binding motif to address how these proteins accumulate at such high densities in the AIS (Garrido et al., 2001; Garrido et al., 2003; Lemaillet et al., 2003; Fache et al., 2004). A CD4 chimera containing the $Na_v1.2$ II-III intracellular loop accumulated at the AIS through domain specific retention in the AIS and selective endocytosis in the somatodendritic regions, mediated by an internalization signal also located within the II-III linker (Fache et al., 2004). In a 2014 review it was stated that there is no direct targeting of Na_v channels to the AIS, based off of these chimeric studies (Leterrier and Dargent, 2014). Full-length Na_v proteins were not used. Chapter 3 of this dissertation discusses experiments done using a fluorescent-protein and extracellular tagged $Na_v1.6$ channel in live-cell, real-time trafficking studies that provide evidence of directed trafficking to the AIS of hippocampal neurons.

AIS cytoskeletal architecture

It has long been understood that the axon, particularly the AIS, has a unique cytoskeletal composition (Arnold and Gallo, 2014). Electron microscopy (EM) micrographs have demonstrated a unique cytoskeletal composition in the AIS (Jones et al., 2014). Recently, the super-resolution microscopy technique STochastic Optical Reconstruction Microscopy (STORM) was used to create a 3D rendering of the actin cytoskeleton with resolution below the diffraction limit (Xu et al., 2013). These experiments demonstrated that the actin based cytoskeletal network in the AIS is organized into periodic rings spaced approximately 190 nm

apart. They found that adducin, an actin-capping protein, co-localizes with the actin rings, while spectrin spans the rings most likely to provide support for the network as well as defining the spacing (Xu et al., 2013).

1.5 High-resolution microscopy in living cells

In addition to Na_v channels, neurons contain thousands of proteins involved in complex biochemical interactions. Such interactions influence the localization and function of $Na_v1.6$. Understanding the processes that exist within neurons, and all living cells, with both spatial and temporal information requires a unique set of tools. The discovery of the jellyfish green fluorescent protein (GFP) revolutionized the ability to relatively non-invasively observe the behavior of a specific subset of proteins in a living cell (Tsien, 1998; Shimomura, 2009). The first 4D studies, or protein localization and dynamics over time, employed techniques such as fluorescence recovery after photobleaching (FRAP) or the use of photoactivatable fluorophores to determine the kinetics and span of protein movement based on exchange of fluorescently and non-fluorescently tagged proteins (Lippincott-Schwartz and Patterson, 2003). Such experiments have given insight into protein localization, movement, protein-protein interactions, and a myriad of other information for unraveling the complexities of cell biology. Variations on these reporters have enabled visualization of other biological processes such as changes in membrane potential with voltage-sensitive reporters such as ArcLight (St-Pierre et al., 2014), and localized changes in internal calcium concentrations with genetically encoded calcium indicators such as GCaMP (Sun et al., 2013). Experiments using these tools have further enhanced our understanding of not only basic protein localization, but of complex signaling cascades and localized responses to stimuli in real-time.

More recent advances in imaging technologies have opened up a new set of tools specifically for looking at integral proteins on the plasma membrane. The plasma membrane serves to define the boundaries of the cell and separate it from the external environment while also providing the bridge that connects the rest of the cell to the extracellular environment via integral membrane proteins and signaling cascades (Laude and Prior, 2004). Relevant to this dissertation, it establishes the ionic gradients within the cells and houses the numerous ion channels necessary for electrical signaling (Hille, 2001). Each of these functions is highly regulated. In terms of neuronal ion channels, the subcellular localization of each protein species is of utmost importance for proper electrical signaling (Zhou et al., 1998; Van Wart and Matthews, 2006). Most ion channels are also regulated by protein-protein interactions and protein modifications (Chahine and O'Leary, 2014). If left to random diffusion, the probability of regulatory proteins finding their target would be incredibly limited within the complex lipid-protein environment of the plasma membrane. Thus, specificity of interactions is in part regulated through confinement of proteins and their regulatory partners within a limited spatial environment.

Single-molecule imaging

A powerful method to understand these types of complex protein interactions and membrane organization is single-molecule tracking of integral membrane proteins in which the diffusion of individual molecules can be imaged with high spatiotemporal resolution. The diffusion of an individual molecule can convey information about the forces it encounters and the biochemical interactions it experiences. For a comprehensive review, see (Krapf, 2015). Particles that have unrestricted movement, or Brownian motion, are considered to have normal diffusion. The area "explored" by a particle can be described by its mean squared displacement

(MSD). For normal diffusion the MSD, on average, increases linearly with time, while particles with MSDs that increase faster or slower than the linear solution show anomalous diffusion. Actively transported molecules are often superdiffusive, and thus will exhibit MSDs that increase faster than with normal diffusion. In contrast, there are a multitude of processes that hinder free diffusion in the biological context of the plasma membrane and result in subdiffusion. These include macromolecular crowding (Banks and Fradin, 2005; Mika and Poolman, 2011), cytoskeletal compartmentalization (Kusumi and Sako, 1996; Tamkun et al., 2007; Andrews et al., 2008), and interactions with anchoring proteins (Nakada et al., 2003; Brachet et al., 2010) or clathrin-coated pits (Weigel et al., 2013).

Single-molecule tracking can be accomplished with a multitude of tools, including fluorescent proteins (Shimomura, 2009), organic fluorophores (Liu et al., 2015), gold nanoparticles (Lasne et al., 2006), and quantum dots (Michalet et al., 2005; Cutler et al., 2013)). Organic dyes are often brighter and more photostable than fluorescent proteins, making them an attractive option for imaging with single-molecule sensitivity. These can be attached to the protein of interest by a variety of methods such as antibody tagged epitopes or biotin-streptavidin attachment schemes (Chen et al., 2005; Howarth et al., 2005; Liu et al., 2015). Quantum dots and gold-nanoparticles avoid photobleaching issues and can be used to follow individual proteins for long times at high imaging rates, although their large molecular size raises concerns about artifacts from frictional forces and steric hindrance, or issues with attachment to the protein of interest (Michalet et al., 2005). Single-molecule tracking allows measurements of individual protein diffusion and localization, providing information about protein heterogeneity within a population.

The amount of information obtained from single-molecule experiments is dependent on the labeling and imaging strategy used. Labeling a sparse number of proteins with bright, non-photobleaching QDs provides long tracks with both high spatial and temporal resolution. However, this strategy only provides information about the subset of proteins that were labeled. Labeling too many molecules results in lack of spatial separation, thus preventing accurate molecule tracks. Thus, information about a broader population of channels relies on the ability to stochastically visualize a subpopulation of fluorescent probes. Photoactivation-localization microscopy (PALM) uses photo-convertible or photo-switchable fluorophores such that a renewing subset of particles cycle through activation and photobleaching. When combined with tracking, single-particle tracking-PALM (spt-PALM) becomes a powerful tool to achieve a high-density of single-particle tracks (Manley et al., 2008; Hoze et al., 2012). uPAINT (universal point-accumulation-for-imaging-in-nanoscale-topography) is a similar strategy that uses probes such as antibodies that bind to extracellular targets, providing a renewable set of fluorescent probes (Giannone et al., 2010; Masson et al., 2014). For each of these strategies it is possible to obtain molecule tracks for thousands of proteins within a few minutes, which can reveal local diffusive properties and describe forces that influence molecule movement.

Super-resolution microscopy

Another advantage of single-molecule imaging is the ability to break the diffraction limit. In general, fluorescence microscopy has limited spatial resolution compared to other imaging techniques such as electron microscopy (EM). A point source of light visualized by light microscopy is seen as diffraction pattern, and thus structures smaller than or two objects within the Abbe diffraction limit (~200-300nm) cannot be clearly resolved (Abbe, 1873; Mccutchen, 1967). Various super-resolution techniques have been developed to overcome the diffraction

barrier including techniques to sharpen the point spread function of the microscope, for example using stimulated emission depletion (STED) microscopy (Hell and Wichmann, 1994). Other techniques localize individual, spatially separated fluorescent molecules. Photoactivation localization microscopy (PALM) and stochastic optical reconstruction microscopy (STORM) use cycles of activation and deactivation of molecules to maintain an optically resolvable subset of fluorophores, using photoactivatable fluorescent proteins or organic dyes, respectively (Rust et al., 2006). These and other techniques allow for visualization of structures with sub-diffraction-limit accuracy of less than 20nm (Huang et al., 2010; Kanchanawong et al., 2010). The accuracy of localization depends mainly on the signal-to-noise ratio, thus localization precision can be enhanced with brighter fluorophores or reducing background noise such as with total internal fluorescence reflection (TIRF) microscopy (Liu et al., 2015).

Together, these technologies and imaging strategies have greatly enhanced our knowledge of protein localization, dynamics, regulation, and macromolecular interactions. As new technologies are developed and new protein populations analyzed, the mysteries of cell biology that underlie all of life will continue to be unveiled.

1.6 Overview of this dissertation

As the first ion channel to be discovered both theoretically and by purification and cloning techniques, voltage-gated sodium channels have a proud place in the history of neuroscience. Poised as the indispensable depolarizing mechanism in nearly every excitable cell, they can be considered the most important group of proteins in the brain. A vast knowledge of their identity, structure/function, and role in human pathologies has been elucidated over the past six decades. However, while the cell biology of many other proteins, and indeed most other ion

channels, have been investigated using various aspects of live-cell imaging, technical difficulties of working with the large and relatively unstable Na_v cDNAs have left the voltage-gated sodium channels out of this important biological revolution.

Understanding sodium channel cell biology is of the utmost importance to our general knowledge of many neurological traumas and pathologies. Neurons precisely regulate the temporal and spatial expression of all of the sodium channel isoforms, and deviations from this result in conditions such as epilepsy or neuropathic pain. As major therapeutic targets, it is important to understand the membrane dynamics, localization, and turnover of these proteins.

When this dissertation project was initiated, very few publications included fluorescent protein- or epitope-tagged Na_v channel constructs (Mohler et al., 2004; Lee and Goldin, 2009), (Zimmer et al., 2002b). Even then these studies did not investigate the live cell dynamics of the channels, but rather imaged fixed neurons. Labeled TTX molecules have been used previously to determine the mobility of Na_v channels in the AIS and soma (Nakada et al., 2003). However, these studies were limited to channel diffusion, and also could not distinguish between different isoforms. A recent study used fluorescently-labeled saxitoxin to measure single-molecule diffusion and localization using super-resolution microscopy techniques (Ondrus et al., 2012). During the course of this study other publications demonstrated the use or creation of either fluorescent protein or epitope-tagged sodium channel constructs (Gasser et al., 2012; Reinhard et al., 2013), however few studies have used these constructs to study the real-time dynamics of Na_v channels. The aim of this dissertation was to perform live-cell, high resolution imaging on a specific Na_v isoform in order to investigate its live cell dynamics, including protein trafficking and mobility.

Chapter 2 demonstrates the successful tagging of $Na_v1.6$ with GFP and an extracellular biotin acceptor domain (BAD) tag to enable live cell labeling of the surface population of channels. Neither of these modifications overtly altered channel activity or localization, making it a suitable tool for investigating the live-cell dynamics of $Na_v1.6$. To the best of our knowledge, this is the first sodium channel construct containing a successful extracellular tag used for single-molecule, live-cell imaging studies.

Chapter 3 demonstrates the use of the constructs to provide evidence for direct trafficking of $Na_v1.6$ to the axon initial segment of neurons during the formation of this excitable membrane. $Na_v1.6$ protein delivery to the plasma membrane was observed with single-molecule sensitivity in real-time. Directed delivery to the AIS depends on interactions with ankyrin, although ability to bind ankyrin does not confer directed delivery to other proteins.

Chapter 4 investigates the somatic distribution of these channels. To the best of our knowledge, this is the first time that the somatic distribution and membrane dynamics of an individual Na_v isoform has been visualized in living neurons. High-density, single-molecule tracks were used to investigate the characteristics of unique nanolocalization of $Na_v1.6$, which occurs in an ankyrin-independent manner.

Chapter 2

Creation of tagged $Na_v1.6$ for live cell imaging

2.1 Introduction

Action potential initiation and waveforms are dependent on the dense concentration of voltage-gated sodium (Na_v) channels at the axon initial segment in most neurons. The number, identity, and precise localization of the Na_v isoforms present greatly influence the electrical properties of neurons. Despite the importance of this topic, relatively little is known about how these proteins are trafficked to and maintained within different neuronal compartments, especially in terms of how the dense localization at the AIS is achieved. Lack of constructs suitable for live-cell imaging have hindered our knowledge of Na_v channel cell biology and live-cell dynamics.

A major deterrent to the creation of such constructs is that Na_v channel cDNAs are notoriously difficult to work with. Since the large, Na_v cDNA contains four homologous repeating domains it is predisposed to recombination events within bacteria. Strategies to avoid these types of events include transforming the DNA into recombination deficient bacteria and growing at reduced temperatures (28°C). When the current project was first initiated, I first tagged the zebrafish (*Danio Rerio*) $Na_v1.6$ cDNA obtained from Lori Isom (University of Michigan) based on suggestions that this was the most stable Na_v clone to work with. Despite the successful introduction of the GFP coding sequence onto the c-terminus of $zNa_v1.6$ cDNA, this construct never expressed in mammalian cells including neurons and HEK cells. We then obtained a mouse (*Mus musculus*) $Na_v1.6$ cDNA from the Waxman Lab at Yale University. pcDNA3.1-$mNa_v1.6R$ (Herzog et al., 2003) was modified to propagate at a low-copy number in

bacteria to minimize the risk of recombination events. The R denotes that this construct contains a Tyr371Ser mutation that renders the channel insensitive to TTX, allowing isolation of the channel from the endogenous TTX-sensitive current in electrophysiological recordings. While this dissertation project was in progress, other labs also successfully modified pcDNA3.1-mNa_v1.6R, including a GFP tag on the c-terminus and the Meisler Lab introduced various functional mutations into the channel (Gasser et al., 2012; O'Brien et al., 2012).

Before this dissertation project was initiated, a handful of Na_v cDNAs were modified previously. The first epitope-tagged Na_v channel was used in the 1990s to provide evidence that the S1-S2 loop was truly extracellular during a time when the orientation of the transmembrane segments of Na_v channels was unknown. An amino acid minimal epitope from an acetylcholine receptor α subunit was inserted into various sites within the predicted domain II S1-S2 of the Na_v1.4 extracellular linker or within the predicted transmembrane segments themselves. Insertion of the epitope tag into the extracellular loop resulted in proper function and trafficking of the channel, while incorporation into either transmembrane domain hindered channel function and reduced surface labeling (Kraner et al., 1998). There have been several additions of an epitope tag to the D1 S5-S6 extracellular loop of Na_v1.5 including a FLAG-tag (Baroudi et al., 2001; Baroudi et al., 2002) and a HA tag (Mohler et al., 2004; Hallaq et al., 2006). However, a recent paper demonstrated that the addition of the FLAG tag in this location altered channel kinetics (Reinhard et al., 2013) and, to the best of our knowledge, these constructs have not been used for high-resolution imaging studies. Na_v1.5 has also been tagged with GFP, YPF, and CFP (Zimmer et al., 2002a; Zimmer et al., 2002b; Biskup et al., 2004; Hallaq et al., 2006). Na_v1.8 was tagged with EFGP and Venus (Schofield et al., 2008) and Na_v1.2 and Na_v1.6, as well as chimeras containing swapped regions between these proteins, have been tagged with EFGP or ECFP on

the N-terminus (Lee and Goldin, 2009). However, the published images of these constructs did not show dramatic AIS localization, which suggested potential hindered trafficking.

Even with the presence of these constructs, still lacking in the field of Na_v channel cell biology were studies of the live-cell dynamics and trafficking of the channel. This chapter outlines the methods used to create novel $Na_v1.6$ constructs containing fluorescent protein and extracellular tags to enable live-cell imaging. A fluorescent protein tag allows for visualization of the total recombinant protein expressed within a transfected cell, while an extracellular tag allows labeling and imaging of the integral membrane protein population present within the plasma membrane. The first construct, and the one discussed in this chapter, contained a GFP and an extracellular biotin acceptor domain (BAD), the minimal sequence of amino acids recognized by a bacterial biotin ligase (birA). Co-transfection with birA results in the biotinylation of the lysine residue in the center of the BAD and allows visualization with streptavidin-conjugated fluorophores.

Since modification of proteins can easily lead to issues with expression, function, or trafficking of a protein (Maue, 2007), great care and multiple strategies were employed when designing and creating the modified proteins. For example, some proteins will tolerate the addition of the fairly large, barrel-shaped structure of GFP on one amino-acid terminus better than the other. For this reason, two constructs were attempted with fusion of GFP to either the N- or C-terminus. In terms of the extracellular tag, two different strategies were attempted. One incorporated the BAD tag into the S5-S6 linker of domain III and the other into the S1-S2 linker of domain IV. Ultimately, the C-terminal tag for the GFP tag and the DIV S1-S2 loop for the BAD tag showed AIS localization in neurons. The function and expression of this $mNa_v1.6$-BAD-GFP construct was then investigated thoroughly. Immunocytochemistry and

electrophysiological studies demonstrated that mNa$_v$1.6-BAD-GFP maintains functional characteristics and localization similar to that observed for endogenous or untagged Na$_v$1.6 in cultured hippocampal neurons. Thus, this construct is suitable for high-resolution, real-time studies of Na$_v$1.6 cell biology.

2.2 Methods

Creation of pcDNA3.1-mNa$_v$1.6R-EGFP

The cDNA clone pcDNA3.1-mNa$_v$1.6R was obtained from the Waxman lab (Yale University). This construct was previously rendered TTX–resistant via a Y371S substitution (Herzog et al., 2003). The XmaI-HpaI fragment encompassing the C-terminal region of the channel and a small portion of the pcDNA3.1 vector was subcloned into pBK to aid in ease of modification since the pcDNA3.1 vector is nearly 14Kbp. Overlap extension PCR was used to introduce KpnI and PacI restriction enzyme recognition sites into the DNA sequence immediately preceding the stop codon. EGFP was PCR amplified with primers that added KpnI and PacI restriction sites such that EGFP was in frame with mNa$_v$1.6 after ligation. The modified XmaI-HpaI fragment was reintroduced into pcDNA3.1-mNa$_v$1.6R and sequenced to verify the expected product.

Creation of pcDNA3.1-mNa$_v$1.6R-BAD-GFP

These regions were identified as regions of low sequence conservation between mouse Na$_v$1.1-Na$_v$1.9 were identified using an amino acid alignment (Figure 2.1). Additionally, these extracellular loops were longer than the corresponding sites in the other homologous domains and contained fewer potential glycosylation sites.

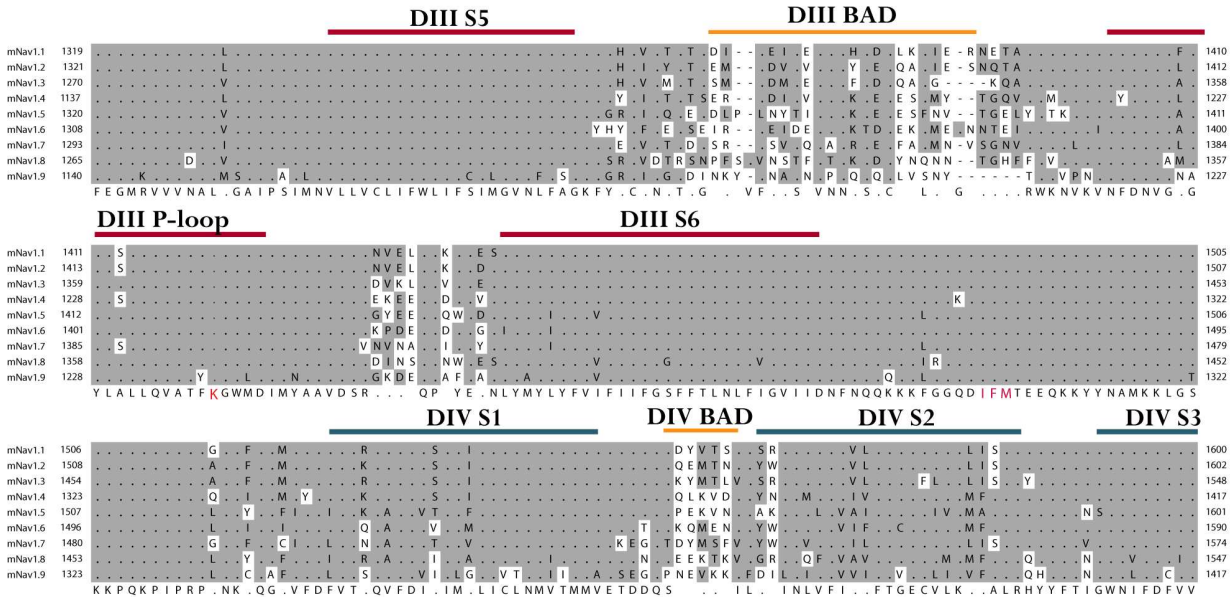

Figure 2.1 DIII S5-S6 and DIV S1-S2 loops show low conservation between Mus musculus $Na_v1.x$ isoforms.

Protein sequence alignment of partial sequence of mouse isoforms $Na_v1.1$-$Na_v1.9$**.** $Na_v1.x$ isoforms demonstrate high conservation in the transmembrane domains and pore region. The grey background denotes amino acid conservation (dots) or similarity (letters). White background represents lack of conservation. The red K in the DIII P-loop denotes the amino acid involved in the selectivity filter and the red IFM amino acids in the DIII S6-DIV S1 intracellular loop are involved in $Na_v1.x$ fast inactivation.

The XmaI-HpaI pcDNA3.1-m$Na_v1.6$R fragment contained the domain IV S1-S2 loop to be modified for addition of the biotin acceptor domain (BAD). Another round of overlap extension PCR was used to introduce NotI and SacII sites between S1545 and K1546. The BAD sequence and surrounding glycine linker was PCR amplified from GFP-$K_v2.1$-BAD with primers to introduce NotI and SacII sites such that the BAD tag was in frame with m$Na_v1.6$. The modified XmaI-HpaI fragment was again introduced into pcDNA3.1-m$Na_v1.6$ to form pcDNA3.1-m$Na_v1.6$ and verified by sequencing.

Cell culture

ND7/23 cells (Sigma-Aldrich, St. Louis, MO, USA) were plated on glass-bottom 35mm dishes (MatTek, Ashland, MA, USA) that had been previously coated with Matrigel (BD Biosciences, San Jose, USA) and cultured in DMEM plus 10% fetal bovine serum supplemented with GlutaMax (Gibco, Life Technologies, Grand Island, NY, USA) and non-essential amino acids (Hyclone, GE Heathcare Life Sciences, Logan, UT, USA). Neuronal cultures were used as previously described (Tamkun et al., 2007). Animal use was according to protocols approved by the Institutional Animal Care and Use Committee of Colorado State University (Animal Welfare Assurance Number: A3572-01). This Institutional Animal Care and Use Committee (IACUC) committee specifically approved this study. Embryonic hippocampal tissue was collected after anesthesia with isoflurane followed by decapitation. Neuronal transfections were performed after days in vitro (DIV)4–6 in culture as indicated for each experiment. Transfections for both cell types were performed with Lipofectamine 2000 (Invitrogen, Life Technologies, Grand Island, NY, USA) and the indicated $Na_v1.6$ (1μg) or GFP-$K_v2.1$-BAD-Na_vABM (0.5μg) channel DNA. When indicated, human β1 in pcDNA3.1Mygro(+), rat β2 in pcDNA3.1VS-HisTopoTA, pSec-BirA (bacterial biotin ligase to biotinylate the $Na_v1.6$ or $K_v2.1$-$Na_v1.2$ proteins), or pEGFP-C1 (to mark transfected cells) were added. When neurons were used following transfection depended on the specific experiment (DIV of transfection/DIV of experiment): Immunolabeling- DIV4 or 6/DIV6,8, or 12 as indicated; surface labeling for AIS to soma ratio and FRAP- DIV4/DIV6,8,10, or 12 as indicated; electrophysiology- DIV4/DIV6; insertion site experiments- DIV4/DIV6 (imaged 36–44 hrs post-transfection for $Na_v1.6$ constructs or 12–16 hrs post-transfection for GFP-$K_v2.1$-BAD-$Na_v1.2$ABM). Endogenous $Na_v1.6$ did not appear consistently in our neuronal cultures until DIV10.

Immunofluorescence

Neurons were fixed in 4% formaldehyde in PBS for 15 min, incubated in PBS + 10% TX-100 + 10% goat serum for 30 min, and labeled with rabbit anti-$Na_v1.6$ antibody (Caldwell et al., 2000) (1:100), mouse monoclonal anti-ankG (NeuroMab; 1:1000), or mouse monoclonal anti-MAP2 (Sigma, 1:1000) diluted in PBS containing 10% goat serum and 1% TX-100. Goat anti-rabbit or goat anti-mouse secondary antibodies conjugated to AlexaFluor-488, 594 or 647 (Molecular Probes, Life Technologies, Grand Island, NY, USA) were diluted 1:1000 in 10% goat serum and PBS.

Electrophysiology

Transfected ND7/23 cells were patch-clamped 24–48 hrs after transfection in a neuronal external solution consisting of (in mM): 110 NaCl, 20 TEA-Cl, 2 MgCl2, 1.2 NaH2PO4, 11.1 glucose, and 10 HEPES, pH 7.4 (adjusted with NaOH), 301 mOsm. 300 nM TTX was added to the bath. The pipette solution contained (in mM): 125 CsCl, 10 NaCl, 1.5 MgCl, 5 HEPES, 0.5 EGTA, pH 7.4 (adjusted with CsOH), 278 mOsm. Pipettes had resistances of 1.4–2.3 MΩ and Ra was 5 MΩ or less. Whole-cell Na^+ currents were recorded at room temperature using an Axopatch 200B amplifier (Molecular Devices, Sunnyvale, CA, USA). Ionic currents were capacitance and series resistance compensated by 70–90%, sampled at 10 kHz (Digidata 1440; Molecular Devices, Sunnyvale, CA, USA), filtered at 2kHz, and leak subtracted online using the P/4 method in pClamp10. Cells were held at -80 mV, stepped to -120 mV for 50 ms to release channels from inactivation, then depolarized to potentials between -70 and +75 mV for 100 ms in 5 mV steps. Activation curves were plotted by converting peak ionic currents (I) to conductance (G) using the relationship: G = I/(V—ENa). ENa was calculated to be +60 mV. Steady-state

inactivation was determined using a 100 ms prepulse ranging from -140 to 40 mV (10mV increments), then stepping to a potential of -10 mV for 40 ms to measure the non-inactivated channels. Peak inward currents were then normalized to the maximal peak current (Imax). Curves were fit with a Boltzmann: y = A2 + (A1—A2)/ (1+exp[(V—V1/2)/k] where A1 is the initial value, A2 is the final value, V is the test potential, V1/2 is the voltage midpoint, and k is the slope factor. Whole cell currents from transfected neurons (DIV6, 2 days post-transfection) were measured as described above.

Image acquisition, presentation, and data analysis

Neurons expressing fluorescent protein–tagged constructs were imaged with either an Olympus FV1000 confocal or a Nikon TIRF microscope as previously described (Deutsch et al., 2012a). Volocity 6.1.1 (PerkinElmer, Waltham, MA, USA) software was used to determine fluorescent intensities, adjust contrast, and quantitate fluorescence. For the surface density ratios, the AIS and soma ROIs were automatically detected using the object finder in Volocity. OriginPro 8.5 (OriginLab, Northampton, MA, USA) was used to analyze and fit numerical data. All measurements of fluorescence intensities were background subtracted from an ROI of similar size to the region being measured. For the ratio of surface density of AIS to somatic $Na_v1.6$, signal in the soma was often only moderately above that of background. For these experiments, background was determined by taking the mean of two background ROI's. Images presented contain identical adjustments for brightness and contrast except where noted. For all imaging experiments with live cells, the stage and objective were heated to 37°C.

Statistics

Data are presented as mean ± s.d. unless otherwise stated. Statistical analysis was performed in Sigmaplot (Systat Software, Inc., San Jose, CA, USA) using an unpaired t-test, paired t-test, or a Mann-Whitney Rank Sum Test for non-parametric data. $p<0.05$ was considered significant.

2.3 Results

$Na_v1.6$-EGFP localizes to the AIS of cultured neurons

To create a construct that enables live cell imaging of $mNa_v1.6$, fusion proteins were created using recombinant DNA techniques to add GFP to either the N- or C-terminus since the large structure of GFP will often be tolerated better on one terminus than the other. Indeed, the N-terminal tag displayed poor trafficking, while the C-terminal tag showed strong AIS localization and robust currents (not shown). Thus, this construct was used for all subsequent experiments.

Identification of candidate loops for the BAD tag

Amino acid alignments were performed for $Na_v1.6$ sequences across several species, as well as between the different Na_v isoforms ($Na_v1.1$-$Na_v1.9$) to identify sites of low conservation in the extracellular loops. These provided candidate regions that might tolerate the introduction of the BAD without altering channel trafficking or function. Based on lack of conservation, two candidate sites were located, the S5-S6 loop of domain III and the S1-S2 loop of domain IV (Fig. 2.1). Although both strategies were tried, only the D4 S1-S2 tag showed robust localization at the AIS and surface labeling with streptavidin-conjugated fluorophores.

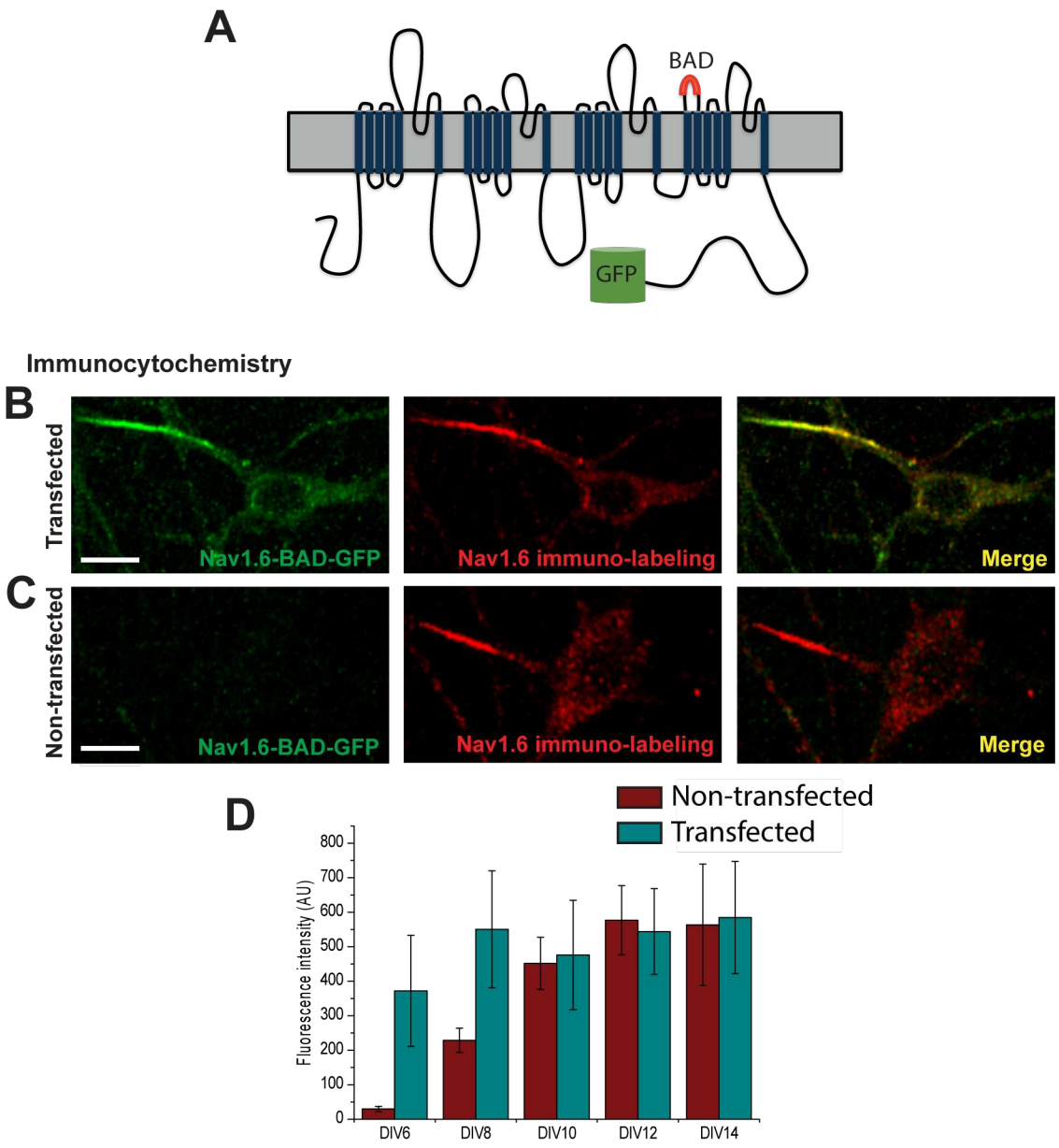

Figure 2.2. $Na_v1.6$-BAD-GFP expression mimics that of the endogenous channel in cultured rat hippocampal neurons.

A) Schematic of the $Na_v1.6$-BAD-GFP construct showing location of the biotin acceptor domain (BAD) and fusion of GFP to the channel C- terminus. (**B-C)** Comparison of anti-$Na_v1.6$ immunolabeling in transfected and non-transfected DIV 12 hippocampal neurons. Compressed confocal z-stack of GFP fluorescence (left panel) and anti-$Na_v1.6$ immunolabeling (middle panel) from a $Na_v1.6$-BAD-GFP transfected neuron **(B)** or a non-transfected neuron **(C)**. Overlay (right panel). Fluorescence intensity of immunolabeling for transfected vs endogenous AIS $Na_v1.6$ expression was not significant (t-test, $p = 0.132$). **D)** Quantitation of mean **f**luorescence intensity of $Na_v1.6$ immunolabeling in the AIS of transfected and non-transfected neurons from DIV 6, 8, 10, 12, and 14. Scale bars represent 10 μm.

$Na_v1.6$-BAD-GFP shows AIS localization and expression levels similar to endogenous

Figure 2.2A is a schematic of the final $mNa_v1.6$-BAD-GFP construct. In order to demonstrate that the overall trafficking, localization, and function of the modified channel mimic those of the unmodified $mNa_v1.6$, we performed immunocytochemistry and electrophysiology

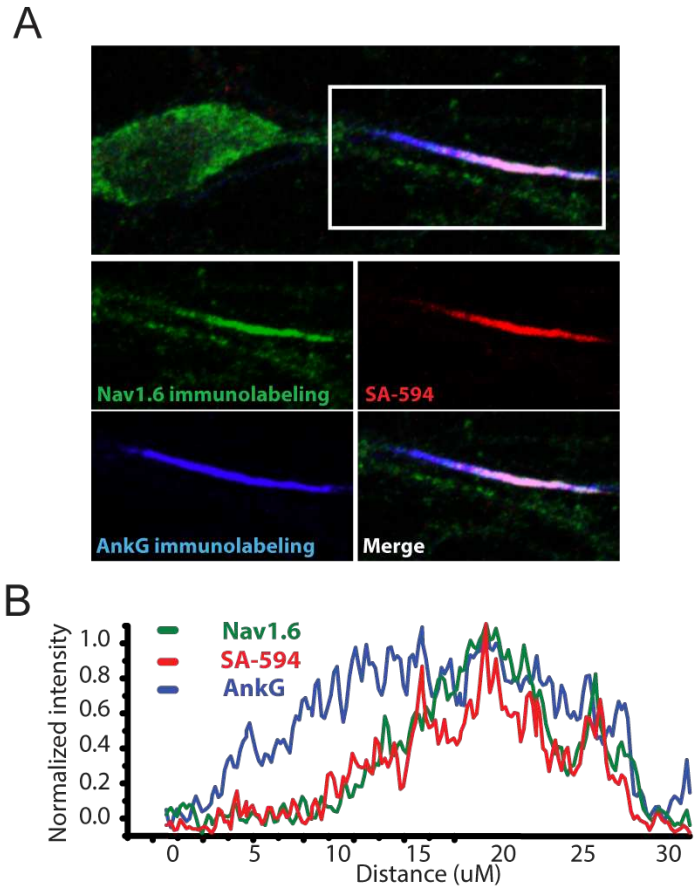

Figure 2.3. $Na_v1.6$-BAD localizes to the distal AIS.

A) Compression of confocal z-stacks of DIV 12 rat hippocampal neuron transfected with $Na_v1.6$-BAD and immunolabeled for $Na_v1.6$ (green) or ankG (blue). $Na_v1.6$-BAD was labeled with SA-594. **B)** Line profile of the AIS showing the simultaneous increase of total $Na_v1.6$ immunolabeling (green) and transfected $Na_v1.6$-BAD SA-594 surface label (red), distal to the rise of ankG intensity (blue).

experiments. $Na_v1.6$-BAD-GFP was expressed in cultured rat hippocampal neurons (rHN) and visualized via confocal and TIRF microscopy. To confirm that the expression levels and localization of the transfected $Na_v1.6$ resembled that of the endogenous $Na_v1.6$, immunolocalization studies were performed using an antibody specific for $Na_v1.6$ (Caldwell et al., 2000). Fig 2.2B shows a compressed confocal z-stack of the GFP fluorescence (left panel) and antibody labeling (middle panel) observed in DIV12 rHN cultures 6 days post-transfection. This time was chosen since the endogenous $Na_v1.6$ channel does not appear until older neuronal cultures. Fig 2.2C shows the antibody labeling of endogenous $Na_v1.6$ at DIV12 (middle panel). The anti-$Na_v1.6$ immunolabeling intensity levels are nearly identical between the transfected and non-transfected neurons in this example, and for the population of transfected neurons we detected only 1.3-fold more $Na_v1.6$ at the AIS, 501±321 arbitrary units (a.u.) (n = 18), than that found endogenously, 375±204 a.u. (n = 14) (ns;t-test), minimizing concerns about artifacts due to overexpression of the recombinant channel.

We then determined how expression of the transfected channel compared with that of the endogenous over the development of our neuronal cultures. Neurons were transfected with $mNa_v1.6$-BAD-GFP on DIV4 and then imaged on either DIV 4, 6, 8, 10, 12, or 14. On the day of imaging, plates that were transfected as well as a non-transfected control plate were immunolabeled for $Na_v1.6$ and ankG to mark the AIS. Figure 2.2D is a graph of intensity of immunolabeling of $Na_v1.6$ in transfected versus non-transfected neurons. Since $Na_v1.6$ expression was based off of immunofluorescence, signal from transfected channels represents both endogenous and transfected $Na_v1.6$. Transfected neurons showed strong $Na_v1.6$ expression at the AIS in DIV6 neurons, and the expression level did not significantly increase even up to DIV14. We found that that endogenous $Na_v1.6$ is not strongly expressed in our hippocampal

cultures until approximately DIV10. Thus, any experiments with the transfected mNa_v1.6 must be interpreted with the caveat that it is early expression for this channel. Presumably other isoforms such as Na_v1.2 are present before this time point since endogenous Na_v current can be measured in young neurons, although the time course of expression and localization of other isoforms has not been established in our culture system.

Na_v1.6 has been reported to localize to the distal region of the AIS (Lorincz and Nusser, 2008). To determine whether the modified Na_v1.6 construct also localizes to the distal region we investigated the distribution of Na_v1.6-BAD in relation to ankG immunolocalization. Fig. 2.3A shows a compressed confocal z-stack of a DIV12 rHN transfected with Na_v1.6-BAD. Na_v1.6 was visualized with immunofluorescence (green) while the surface expression of Na_v1.6-BAD was visualized with SA-594 (red). Immunofluorescence can detect both endogenous and transfected channels. Both of these signals were distal to start of the AIS as determined by ankG immunolocalization (blue). Fig. 2.3B is a line scan of the AIS showing that both the immunolocalized and surface labeled Na_v1.6 demonstrated increased fluorescence intensity in the distal portion of the AIS. Importantly, these two signals increased together, suggesting that both transfected and endogenous Na_v1.6 channels localize to the same portion of the AIS when expressed in the same neuron.

We next investigated whether neurons transfected with Na_v1.6-BAD, and thus expressing both endogenous and transfected Na_v1.6 channels, have the same distribution of Na_v1.6 within the AIS as neurons expressing only endogenous channels. Fluorescence intensity of immunolocalized Na_v1.6 (endogenous and transfected channels) was determined in relation to ankG, as demonstrated by the line scan in Fig. 2.3B. Fig. 2.4 shows the summary data from transfected versus non-transfected neurons. For DIV12 rHNs, immunolocalized Na_v1.6 was

concentrated in the distal region of the AIS as defined by ankG for both populations of neurons (Figure 2.4A). However, for DIV6 rHNs the transfected channel was concentrated in the distal AIS in only half of the cells examined (Figure 2.4B). This variability is not surprising since the AIS is changing rapidly during this developmental period. Expression of the $Na_v1.6$-BAD did not alter AIS length, for the immunolocalized ankG averaged 18.1±4.0 and 17.3±4.7 µm (n = 9 and 8, ns; *t*-test, p = 0.7) for DIV12 transfected and non-transfected neurons, respectively.

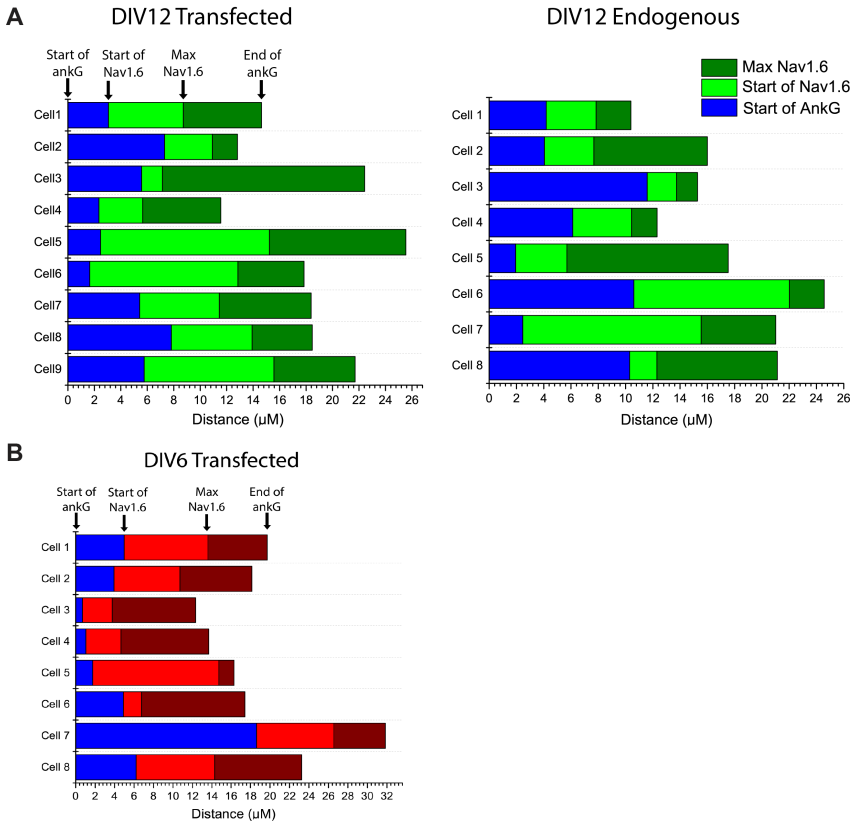

Figure 2.4. $Na_v1.6$ localizes to the distal AIS in both neurons transfected with $Na_v1.6$-BAD and non-transfected neurons.

Neurons were immunolabeled for $Na_v1.6$ and ankG. Neurons transfected with $Na_v1.6$-BAD were identified by SA-594 labeling. **A)** Expression profiles of $Na_v1.6$ in the AIS of DIV12 neurons. The start (blue) and end of the AIS were determined by the presence of ankG. $Na_v1.6$ localization was determined by the fluorescence intensity of immunofluorescence. The initial rise in fluorescence intensity (light green) and maximum intensities (dark green) are indicated for transfected neurons (left) and non-transfected neurons (right). **B)** Expression profiles of $Na_v1.6$ in the AIS of DIV6 neurons. Only neurons transfected with $Na_v1.6$-BAD were analyzed since endogenous $Na_v1.6$ is not expressed at this age in culture. The maximum intensity was not found in the distal portion of the AIS for all DIV6 neurons.

GFP- and biotinylation domain-tagged $Na_v1.6$ channels demonstrate functional properties very similar to the wild-type channel

$Na_v1.6$ has previously been tagged with GFP on the channel C-terminus with retention of wild-type activity (Gasser et al., 2012). To verify that the insertion of the BAD had minimal effects on function, we transfected the wild-type and $Na_v1.6$-BAD-GFP constructs into both the ND7/23 neuronal cell line and rHNs and analyzed channel properties via whole-cell voltage-clamp recording. The $Na_v1.6$ channel was previously rendered tetrodotoxin (TTX)-resistant (Y371S), which allows easy isolation of the transfected $Na_v1.6$ current by blocking the endogenous TTX-sensitive inward currents with 300nM TTX (Herzog et al., 2003). Fig 2.5A illustrates that similar current waveforms were obtained when comparing the wild-type and

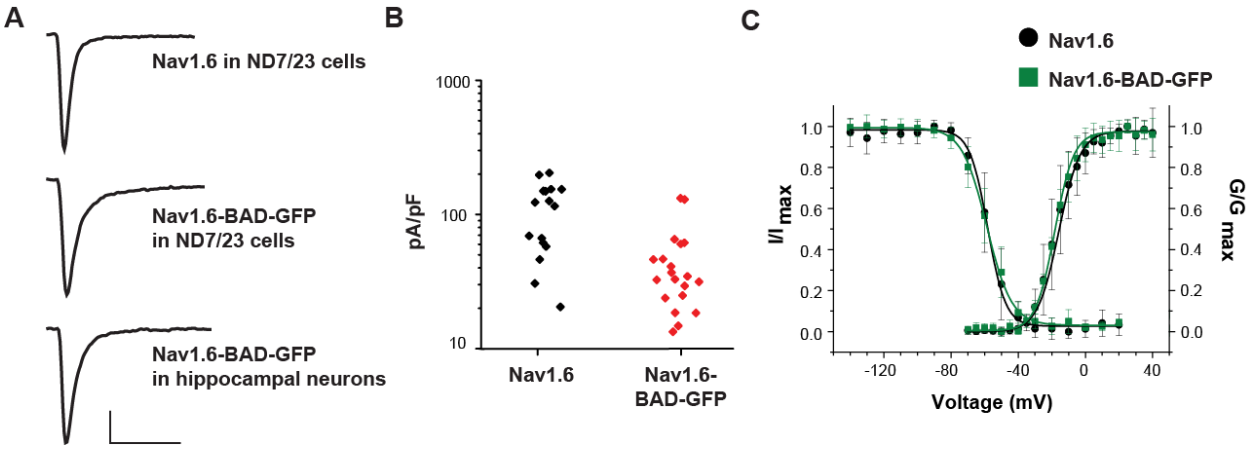

Fig 2.5. $Na_v1.6$-BAD-GFP displays wild-type currents.

ND7/23 neuroblastoma cells or DIV6 rat hippocampal neurons were transfected with either the wild-type channel or $Na_v1.6$-BAD-GFP and the resulting TTX-resistant currents analyzed by whole-cell voltage-clamp in the presence of 300 nM TTX. **A)** Representative current traces from the indicated cell type and construct. Scale bars represent 500 pA and 5 ms. B) Summary of current densities for WT and $Na_v1.6$-BAD-GFP expressed in hippocampal neurons. The difference in mean peak current density (116.8±63.06, n = 16 and 48.42±35.73 pA/pF, n = 20,) was significant ($p<0.001$) although many of the cells expressing the $Na_v1.6$-BAD-GFP channel had expression levels similar to cells expressing the wild-type channel. Currents were recorded 2 days post-transfection. **C)** Voltage-dependence of fast-inactivation and activation for wild-type $Na_v1.6$ (•) and $Na_v1.6$-BAD-GFP (■) as measured in ND cells 36–48 hours post-transfection. Error bars are mean ± s.d.

$Na_v1.6$-BAD-GFP constructs in ND7/23 cells and hippocampal neurons. Current densities for the transfected wild-type $Na_v1.6$ and the $Na_v1.6$-BAD-GFP in rHN averaged 116.8±63.06, n = 16

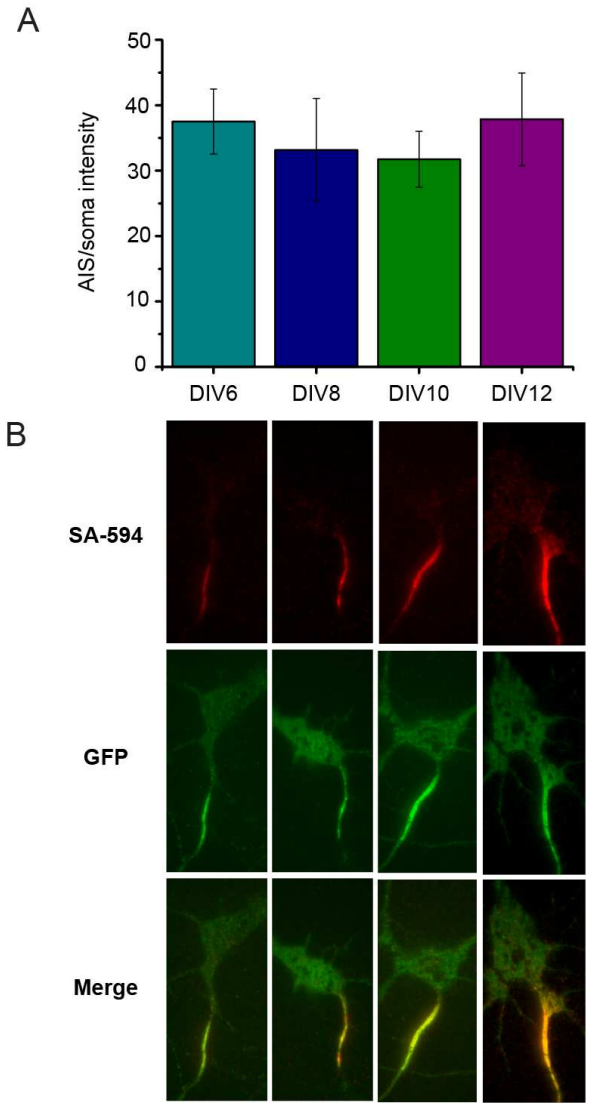

Figure 2.6. The AIS to soma ratio of $Na_v1.6$ in cultured hippocampal neurons remains constant through development.

Neurons were transfected with $Na_v1.6$-BAD-GFP on DIV4 and then imaged via TIRF microscopy on DIV 6, 8, 10, or 12. Neurons were incubated in SA-594 before imaging to label surface channels. **A)** The mean fluorescence intensity of SA-594 in the AIS and soma were determined for each neuron. The AIS to soma ratio was approximately 35 for all ages imaged. **B)** Representative images of neurons from each timepoint. The SA-594 signal (top) indicates channels with true surface expression while the GFP signal demonstrates any $Na_v1.6$-BAD-GFP channels within the TIRF field. Images are presented with identical contrast. Note the increase in SA-594 intensity in the AIS during neuronal development.

and 48.42±35.73 pA/pF, n = 20, respectively. While the differences in mean current densities are significant ($p<0.001$; Mann-Whitney), the distribution illustrated in Fig 2.5B illustrates that there is considerable overlap. The endogenous Na_v currents in DIV6 non-transfected neurons as measured in the absence of TTX, presumably carried by a mixture of $Na_v1.1$, $Na_v1.2$, and $Na_v1.6$ (Felts et al., 1997), had a current density of 214.3±64.9 pA/pF, n = 6. The current density of the recombinant $Na_v1.6$ channels (48–117 pA/pF) is in agreement with the endogenous $Na_v1.6$ channel contribution of 40% to the TTX-S current in hippocampal neurons. Fig 2.5C shows the voltage-dependence of activation and fast-inactivation for the wild-type and $Na_v1.6$-BAD-GFP constructs following expression in ND cells. The wild-type and tagged channels showed activation midpoints of -15.8±0.8, n = 6 and -18.3±0.4 mV, n = 8, and fast-inactivation midpoints of -58.2±1.3, n = 6, and -58.7±0.1 mV, n = 9, respectively, (values are mean ± s.e.m.) which are in agreement with published values (Gasser et al., 2012). The rate of fast inactivation was comparable between the wild type and $Na_v1.6$-BAD-GFP constructs, with time constants of (0.78±0.03, n = 6; 1.00±0.05, n = 7; mean ± s.e.m.), respectively. This difference does not achieve statistical significance ($p = 0.051$, Mann-Whitney).

AIS to soma ratio

Functional studies of the number of Na_v channels in the AIS relative to those in the soma have ranged from a ratio of 3 to over 100. With the cell surface specific BAD labeling combined with sensitivity of TIRF microscopy, we are able to visualize the distribution of $Na_v1.6$-BAD-GFP with single-molecule sensitivity. The ratio of surface density for channels in the AIS plasma membrane compared to the soma surface as visualized by fluorescence intensity of the surface label remained relatively constant with time in culture post-transfection (38±6, n = 11; 33±8, n = 11; 32±4, n = 16; 38±7, n = 13 for DIV6, 8, 10, and 12 respectively; ns;anova) (Figure 2.6). This

is in good agreement to the AIS to soma ratio of 39±9 found using freeze-fracture replica labeling (FRIL) electron microscopy to observe membrane-bound $Na_v1.6$ in hippocampal neurons (Lorincz and Nusser, 2010).

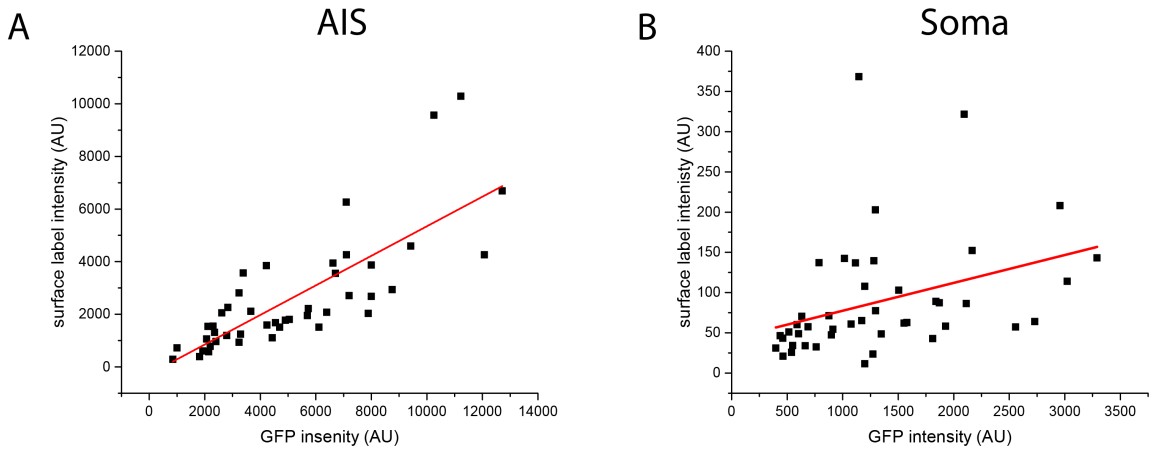

Figure 2.7. Fluorescence intensity of surface labeled $Na_v1.6$-BAD-GFP is a more reliable indication of surface expression than GFP.

Neurons were transfected with $Na_v1.6$-BAD-GFP on DIV4 and then imaged via TIRF microscopy on DIV 10. Neurons were incubated in SA-594 before imaging to label surface channels. The mean fluorescence intensity of SA-594 and GFP were determined for each neuron and plotted against each other for the AIS **(A)** and soma **(B)**. **A)** Fluorescence intensities for $Na_v1.6$-BAD-GFP in the AIS showed a positive trend for both labels such that increased GFP expression correlated to increased SA-594 labeling. **B)** Increased GFP intensity in the soma did not show any relationship to SA-594 intensity.

Several studies have estimated the ratio of somatic to axonal protein based on a fluorescent protein reporter (Garrido et al., 2003; Brachet et al., 2010). To determine how well the intensity of the GFP signal corresponds with that of the surface label for $Na_v1.6$, we used TIRF microcopy to image neurons expressing $Na_v1.6$-BAD-GFP. Channels were surface labeled streptavidin conjugated dye and the mean intensity of the GFP and the surface label were determined for both the soma and AIS for each cell. Figure 2.7 shows the mean fluorescence intensity of the surface label plotted against that of the GFP fluorescence. The signals in the AIS show a rough correlation such that increased GFP fluorescence showed increased surface

labeling, although there was a great deal of variability. There was almost no correlation in the soma. This demonstrates that the GFP signal itself is not a reliable indication of channel surface expression even using TIRF microscopy, especially in the soma where there is a large pool of intracellular channel.

Creation of Other $Na_v1.6$ constructs

Numerous other modifications were made to pcDNA3.1-m$Na_v1.6$R during the course of this dissertation to enable a variety of imaging studies as well as investigations in functional aspects of the channel. These included removal of the ankyrin-binding motif (discussed in chapter 3), substitution of the GFP for Dendra2 to enable techniques such as single-particle tracking photoactivation localization microscopy (spt-PALM) (discussed in chapter 4), and modification of the selectivity filter to render the channel calcium permeable. We have made a single ion selectivity mutation (K1411E) that modifies the Na_v selectivity filter (DEKA) away from Na+ to one that favors Ca^{2+} while also increasing pore conductance (Hinman et al., 2013). When expressed in hippocampal neurons, this modified $Na_v1.6$-GFP wild-type trafficking and is Ca^{2+} permeable as illustrated by Fig. 2.8. Using Ca^{2+} imaging dyes such as Fluo-4, this Ca^{2+} permeable-$Na_v1.6$ allows temporally and spatially enhanced high-resolution imaging of $Na_v1.6$ channel activity via TIRF microscopy. Chapter 4 discusses the presence of clustered immobile $Na_v1.6$ on the soma surface, which raises the question of whether these immobilized channels are functionally distinct from the freely diffusing channels, or even those located in the AIS. Studies with this Ca^{2+} permeable $Na_v1.6$ channel have been initiated, but are not included in this dissertation.

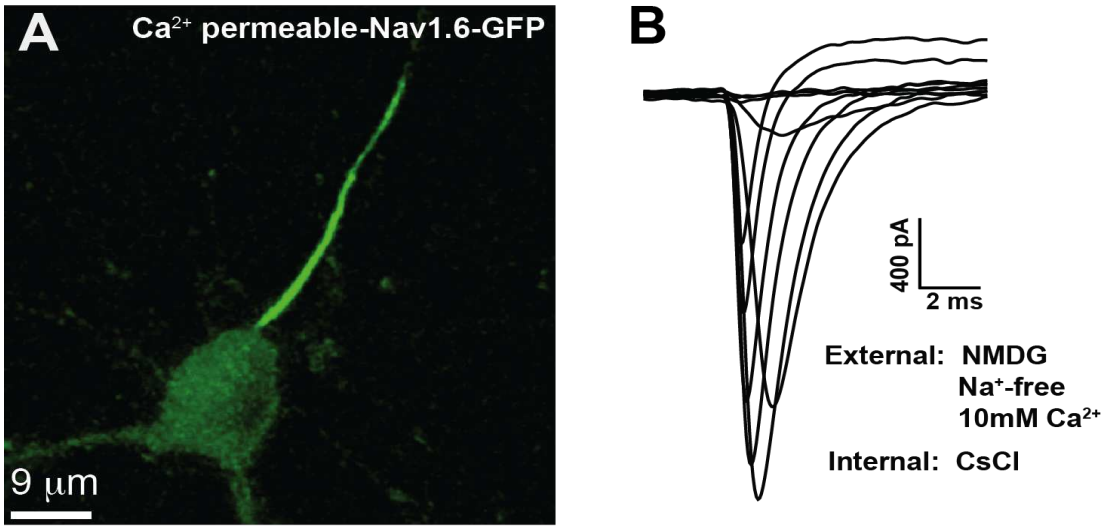

Fig. 2.8. A Ca^{2+} -permeable $Na_v1.6$ channel shows wild-type trafficking and function in hippocampal neurons.

A) Confocal GFP image of a 6 DIV rat hippocampal neuron expressing the Ca^{2+} -permeable $Na_v1.6$-GFP channel. **B)** Whole-cell current recorded in response to 100ms voltage steps from -60 mV to +30 mV in 10 mV increments. The prepulse potential was -100mV. The pipette solution contained 120 mM CsCl as the main ion and the bath solution contained 110 mM NMDG and 10mM Ca^{2+} . All solutions were Na+ free. Non-transfected neurons showed no inward currents under these conditions. The activation midpoint was near -20 mV.

2.4 Discussion

The successful incorporation of an extracellular and protein tagged $Na_v1.6$ clone that maintains near to wildtype characteristics and expresses well in neurons allows for investigations into the cell biology of $Na_v1.6$ not possible before. This advancement hinged on the creation of the stable, modifiable cDNA clone by the Waxman lab, punctuated by my failed attempt to express the modified zebrafish clone ($zNa_v1.6$). The successful incorporation of extracellular tags into other Na_v isoforms will enable investigations into isoform interactions, regulation, and activity. The success of the $Na_v1.6$-BAD-GFP construct was due to the stable vector background, the use of a highly efficient extracellular tag, and the careful placement of the extracellular tag. There are many potential extracellular tags enabling live-cell labeling and imaging of surface

proteins, such as a human influenza hemagglutinin (HA) tag which is recognized by an anti-HA antibody. The use of the BAD tag was chosen for several reasons. First, biotin-streptavidin interactions are some of the strongest known in biology. Second, streptavidin-conjugated flourophores are generally smaller than anti-HA antibodies which can improve labeling efficiency by avoiding issues of steric hindrance and improved spatial localization during super-resolution microscopy. Third, the BAD has been successfully used in the Tamkun Laboratory with $K_v2.1$ for most of a decade (Tamkun et al., 2007).

The modified channel expresses well in cultured hippocampal neurons with strong AIS localization, near endogenous expression levels within the AIS, and electrophysiological properties similar to untagged $Na_v1.6$. Importantly, the modified channel localizes to the distal end of the AIS in mature neurons, demonstrating that the localization mechanisms that produce this type of distribution have not been altered. Since the channel shows proper subcompartmental distribution, it is likely that proper trafficking of the channel has not been altered either, and thus make this construct suitable for localization and trafficking studies of $Na_v1.6$.

Due to the scarcity of $Na_v1.6$ on the somatic neuronal membrane, combined with a large intracellular pool of $Na_v1.6$, it has been nearly impossible to determine the somatic distribution of $Na_v1.6$ based on immunocytochemistry. The only successful method previously has been SDS-FRIL electron microscopy (Lorincz and Nusser, 2010). The AIS to soma ratio determined with that method, 39±9, is in close agreement with the ratio obtained with the surface label on $Na_v1.6$-BAD-GFP, which is another indication of proper localization of the modified protein. Surprisingly, the AIS to soma ratio did not increase with neuronal maturation in our assay, despite the fact that the AIS tends to grow in size and gain more channels as the neuron matures. This suggests that the mechanisms controlling both the high concentration of $Na_v1.6$ channels at

the AIS and the somatic distribution are both present even in immature neurons and develop nearly simultaneously.

Chapter 3

Preferential targeting of $Na_v1.6$ voltage-gated Na^+ channels to the axon initial segment during development[1]

Summary

During axonal maturation, voltage-gated sodium (Na_v) channels accumulate at the axon initial segment (AIS) at high concentrations. This localization is necessary for the efficient initiation of action potentials. The mechanisms underlying channel trafficking to the AIS during axonal development have remained elusive due to a lack of Na_v reagents suitable for high resolution imaging of channels located specifically on the cell surface. Using an optical pulse-chase approach in combination with a novel $Na_v1.6$ construct containing an extracellular biotinylation domain we demonstrate that $Na_v1.6$ channels are preferentially inserted into the AIS membrane during neuronal development via direct vesicular trafficking. Single-molecule tracking illustrates that axonal channels are immediately immobilized following delivery, while channels delivered to the soma are often mobile. Neither a $Na_v1.6$ channel lacking the ankyrin-binding motif nor a chimeric $K_v2.1$ channel containing the Na_v ankG-binding domain show preferential AIS insertion. Together these data support a model where ankG-binding is required for preferential $Na_v1.6$ insertion into the AIS plasma membrane. In contrast, ankG-binding alone does not confer the preferential delivery of proteins to the AIS.

---

[1] Modified from: Akin EJ, Solé L, Dib-Hajj S, Waxman SG, Tamkun MM (2015) Preferential Targeting of $Na_v1.6$ Voltage-Gated Na+ Channels to the Axon Initial Segment during Development. PLoS ONE 10(4): e0124397. doi:10.1371/journal.pone.0124397

3.1 Introduction

Voltage-gated sodium (Na_v) channels are responsible for the initiation and conduction of action potentials in neurons and are densely accumulated at the axon initial segment (AIS) (Kole and Stuart, 2008). Na_v channels are composed of a highly post-translationally modified pore-forming α-subunit and auxiliary β-subunits (Isom et al., 1992). Of the nine Na_v alpha subunits ($Na_v1.1$-1.9), $Na_v1.1$, $Na_v1.2$, $Na_v1.3$ and $Na_v1.6$ are the major isoforms within the central nervous system (Catterall et al., 2005) and the action potential waveform is determined to a large extent by the differential expression and distribution of these isoforms within the somatodendritic and axonal compartments (Boiko et al., 2003; Hu et al., 2009; Lorincz and Nusser, 2010). As such, the number, type, and location of channels must be precisely regulated to ensure proper neuronal function.

The AIS is a highly complex structure that can form without glial contact in cultured hippocampal neurons, in contrast to nodes of Ranvier that require interactions with glial cells (Ogawa and Rasband, 2008). The axon can be identified in cultured hippocampal neurons within one to two days in vitro (DIV) and its specialized cytoskeleton and unique protein content develops over the first week in culture(Dotti et al., 1988). AnkG (ankG), an intermediate anchoring protein that tethers many AIS proteins to the actin-spectrin cytoskeleton, is considered the master organizer of the AIS (Hedstrom et al., 2008). AnkG is detected in cultured hippocampal neurons as early as DIV3, increasing in expression levels and becoming highly localized to the AIS by DIV7 (Galiano et al., 2012). Over a similar timeframe, Na_v channels are recruited to the AIS via binding to ankG. This binding is mediated by a sequence of 9 amino acids, the ankG-binding motif (ABM), within the intracellular linker between Na_v domains II-III

(Garrido et al., 2003; Lemaillet et al., 2003), an interaction regulated by the protein kinase CK2 (Bréchet et al., 2008; Gasser et al., 2012).

While the ABM has been shown to be necessary to localize $Na_v1.6$ to the AIS (Gasser et al., 2012) the trafficking route taken by these channels as they become concentrated at the AIS during axonal development is still elusive. Initial studies of Na_v channel trafficking in neurons used chimeric proteins consisting of a fusion between the extracellular domain of CD4 and the C-terminal cytoplasmic domain of $Na_v1.2$ (Garrido et al., 2001). This construct showed axonal localization. Other CD4 chimeric constructs contained the $Na_v1.2$ ABM and accumulated at the AIS following ubiquitous delivery to the cell surface and selective endocytic elimination from the somatodendric regions (Fache et al., 2004). The AIS accumulation of this chimeric protein was presumably due to ankG binding. While studies with these chimeras have been indispensable for our understanding of Na_v localization and ankG binding, they do not fully recapitulate that of the native channel (Gasser et al., 2012). In addition to the studies with chimeras, experiments have been performed with GFP-tagged versions of the full length $Na_v1.2$ and 1.6 channels in order to address axonal localization (Lee and Goldin, 2009; Gasser et al., 2012). These studies indicated that the $Na_v1.2$ N-terminal domain is required for axonal targeting and that the $Na_v1.6$ ABM is essential for accumulation at the AIS. However, both the chimera-based studies and those utilizing the GFP-tagged full-length channel could not determine the location of protein delivery to the plasma membrane, rather just the site of steady-state protein accumulation.

In order to address these points, we used the full-length $Na_v1.6$ channel construct containing an extracellular biotin tag and intracellular GFP tag as described in chapter 2 of this dissertation. Here we use this construct for imaging studies using sensitive TIRF microscopy to

visualize both the site of protein insertion and subsequent membrane dynamics of individual $Na_v1.6$ molecules as they are delivered to, and anchored within, the AIS during axonal development. We find that $Na_v1.6$ is preferentially inserted into the axonal membrane, where we observe small numbers of channels simultaneously delivered directly to spatially discrete sites. Channels delivered to the axon are immediately immobilized, while channels delivered to the somatodendritic region are often mobile, although they are not observed to diffuse into the AIS. $Na_v1.6$ lacking the ABM and a $K_v2.1$-$Na_v1.2$ABM chimera are not preferentially trafficked to the AIS, demonstrating that ankG binding is necessary for preferential delivery to the AIS.

3.2 Materials and Methods

Plasmid constructs

The pcDNA3.1-$Na_v1.6$ channel was previously rendered TTX–resistant via a Y371S substitution (Herzog et al., 2003). Overlap PCR mutagenesis techniques were used to introduce KpnI and PacI restriction sites at the C-terminus of $Na_v1.6$ for insertion of GFP. Additional sites, NotI and SacII, were introduced between S1545 and K1546 within the extracellular domain between S1-S2 of domain IV, into which a biotin acceptor domain (BAD) was inserted (O'Connell et al., 2006). For the $Na_v1.6$-dABM constructs, PCR mutagenesis was used to remove the ankG-binding motif (Lemaillet et al., 2003), amino acids 1094-1102 (VPIAVGESD). The GFP-$K_v2.1$-BAD-$Na_v1.2$ABM construct was generated from the HA-$K_v2.1$-$Na_v1.2$ 1,080-1,203-GFP (Brachet et al., 2010) by replacing the ApaI-ApaI fragment from GFP-$K_v2.1$-BAD (O'Connell et al., 2006). This exchanged the extracellular HA epitope with the BAD tag. The GFP from ankG-GFP (gift from Vann Bennett, Duke University) was replaced with mCherry using SacII and NotI sites.

Cell culture and transfection

Neuronal cultures were used as previously described (O'Connell et al., 2006). Animal use was according to protocols approved by the Institutional Animal Care and Use Committee of Colorado State University (Animal Welfare Assurance Number: A3572-01). This Institutional Animal Care and Use Committee (IACUC) committee specifically approved this study. Embryonic hippocampal tissue was collected after anesthesia with isoflurane followed by decapitation. Neuronal transfections were performed after days in vitro (DIV) 4–6 in culture as indicated for each experiment. Transfections for both cell types were performed with Lipofectamine 2000 (Invitrogen, Life Technologies, Grand Island, NY, USA) and the indicated $Na_v1.6$ (1μg) or GFP-$K_v2.1$-BAD-Na_vABM (0.5μg) channel DNA. When indicated, human β1 in pcDNA3.1Mygro(+), rat β2 in pcDNA3.1VS-HisTopoTA, pSec-BirA (bacterial biotin ligase to biotinylate the $Na_v1.6$ or $K_v2.1$-$Na_v1.2$ proteins (Tamkun et al., 2007)), ankG-GFP/mCherry, or pEGFP-C1 (to mark transfected cells) were added. When neurons were used following transfection depended on the specific experiment (DIV of transfection/DIV of experiment): Immunolabeling- DIV4 or 6/DIV6,8, or 12 as indicated; surface labeling for AIS to soma ratio and FRAP- DIV4/DIV6,8,10, or 12 as indicated; electrophysiology- DIV4/DIV6; insertion site experiments- DIV4/DIV6 (imaged 36-44 hrs post-transfection for $Na_v1.6$ constructs or 12-16 hrs post-transfection for GFP-$K_v2.1$-BAD-$Na_v1.2$ABM). Endogenous $Na_v1.6$ did not appear consistently in our neuronal cultures until DIV10.

Immunofluorescence

Neurons were fixed in 4% formaldehyde in PBS for 15 min, incubated in PBS + 10% TX-100 + 10% goat serum for 30 min, and labeled with rabbit anti-$Na_v1.6$ antibody (Caldwell et

al., 2000, 1:100), mouse monoclonal anti-ankG (NeuroMab; 1:1000), or mouse monoclonal anti-MAP2 (Sigma, 1:1000) diluted in PBS containing 10% goat serum and 1% TX-100. Goat anti-rabbit or goat anti-mouse secondary antibodies conjugated to AlexaFluor-488, 594 or 647 (Molecular Probes, Life Technologies, Grand Island, NY, USA) were diluted 1:1000 in 10% goat serum and PBS.

Fluorescence recovery after photobleaching (FRAP)

Biotinylated $Na_v1.6$-BAD-GFP in transfected rat hippocampal neurons (rHNs) were labeled with SA-594 (1:1,000 dilution in imaging saline) at 37ºC for 10 min and then washed 3-4 times with imaging saline. Imaging and photobleaching were performed using an Olympus (Tokyo, Japan) FV1000 confocal microscope as previously described (O'Connell et al., 2006). Images were acquired every 1 min and the recovery of both GFP and SA-594 fluorescence within the bleach region quantitated The GFP signals were fit with a single exponential to determine percent recovery. Adjustments to brightness and contrast are identical for comparisons between time points, however, the brightness and contrast were enhanced to allow visualization of the vesicles.

Detection of intracellular channel insertion into the plasma membrane

Biotinylated $Na_v1.6$-BAD-GFP channels on the neuronal surface 36-44 hrs post-transfection (channels do not fully accumulate at AIS until ~48 hrs post-transfection) were blocked using 1 μM NeutrAvidin for 5 min, then washed 5-6 times with imaging saline. During TIRF imaging (2.5 Hz, 100 ms exposure), 1 nM SA-594 was added to the bath. Controls for the effectiveness of NeutrAvidin block, necessity of channel trafficking for binding, and kinetics of fluorophore binding were performed as previously reported (Deutsch et al., 2012b).

Image acquisition, presentation, and data analysis

Neurons expressing fluorescent protein–tagged constructs were imaged with either an Olympus FV1000 confocal or a Nikon TIRF microscope as previously described (Deutsch et al., 2012b). Volocity 6.1.1 (PerkinElmer, Waltham, MA, USA) software was used to determine fluorescent intensities, create the kymograph, adjust contrast, and quantitate fluorescence. For the surface density ratios, the AIS and soma ROIs were automatically detected using the object finder in Volocity. The ImageJ Manual Tracking plugin was used to track individual SA-594 molecules. OriginPro 8.5 (OriginLab, Northampton, MA, USA) was used to analyze and fit numerical data. All measurements of fluorescence intensities were background subtracted from an ROI of similar size to the region being measured. For the ratio of surface density of AIS to somatic $Na_V1.6$, signal in the soma was often only moderately above that of background. For these experiments, background was determined by taking the mean of two background ROI's. Images presented contain identical adjustments for brightness and contrast except where noted. Detection of insertion events, visualized as appearance of SA-594, was through manual inspection. Particles that appeared but remained for less than 1 s were considered non-specific and were excluded. Diffusion coefficients were calculated from the mean square displacements as previously described (Tamkun et al., 2007). For all imaging experiments, the stage and objective were heated to 37°C.

Statistics

Data are presented as mean ± s.d. unless otherwise stated. Statistical analysis was performed in Sigmaplot (Systat Software, Inc., San Jose, CA, USA) using an unpaired t-test,

paired t-test, or a Mann-Whitney Rank Sum Test for non-parametric data. $p<0.05$ was considered significant.

3.3 Results

GFP and biotinylation domain-tagged $Na_v1.6$ channels localize to the axon initial segment in cultured hippocampal neurons

To enable real-time imaging of $Na_v1.6$ dynamics in neurons, GFP was fused to the C-terminus of the mouse $Na_v1.6$ channel and a biotin acceptor domain (BAD) (Tamkun et al., 2007) was inserted into the S1-S2 extracellular loop of domain IV as described in Chapter 2 (Fig. 2.2A). The expression levels (Fig. 2.2B-C) and subcellular localization (Fig. 2.3, Fig. 2.4) were

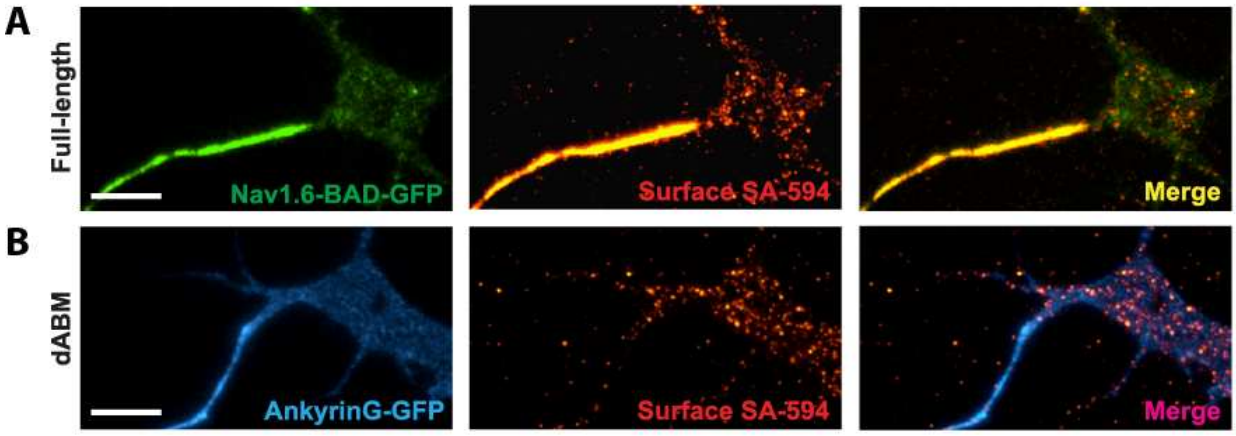

Figure 3.1 $Na_v1.6$-BAD-GFP localizes to the AIS in an ankyrin-dependent manner.

(A-B) Surface expression of full-length $Na_v1.6$ or $Na_v1.6$ lacking the ankG-binding motif (ABM) in live neurons visualized by TIRF microscopy. **A)** $Na_v1.6$-BAD-GFP is highly enriched at the AIS as indicated both by total expressed protein (green) and surface expression (red) visualized by live cell labeling with SA-594. **B)** $Na_v1.6$-dABM-BAD co-expressed with ankG-GFP (blue) as an axonal marker. Surface channels labeled with SA-594 (red) demonstrated a lack of axonal localization while maintaining a somatic expression pattern similar to the full-length channel. Panels B and C are taken from DIV12 cultures since the endogenous $Na_v1.6$ does not appear until this developmental time. Panels D and E are from DIV8 cultures. Scale bars represent 10 μm.

characterized to demonstrate that the modifications to $Na_v1.6$ did not alter any of these properties in relation to endogenous $Na_v1.6$. Furthermore, the functional properties of the channel (Fig. 2.5) were characterized via whole-cell electrophysiology to demonstrate that the tags did not alter channel function compared to untagged $Na_v1.6$.

$Na_v1.6$-BAD-GFP construct was expressed in cultured rat hippocampal neurons (rHN) and visualized via TIRF microscopy, using streptavidin-conjugated AlexaFluor-594 (SA-594) to label the extracellular BAD tag (Fig. 3.1A). The surface-specific fluorescence derived from the SA-594 (Fig. 3.1A, middle panel) indicates robust surface localization at the AIS. Interestingly, surface $Na_v1.6$ labeling showed a punctate localization pattern on the soma. The extracellular

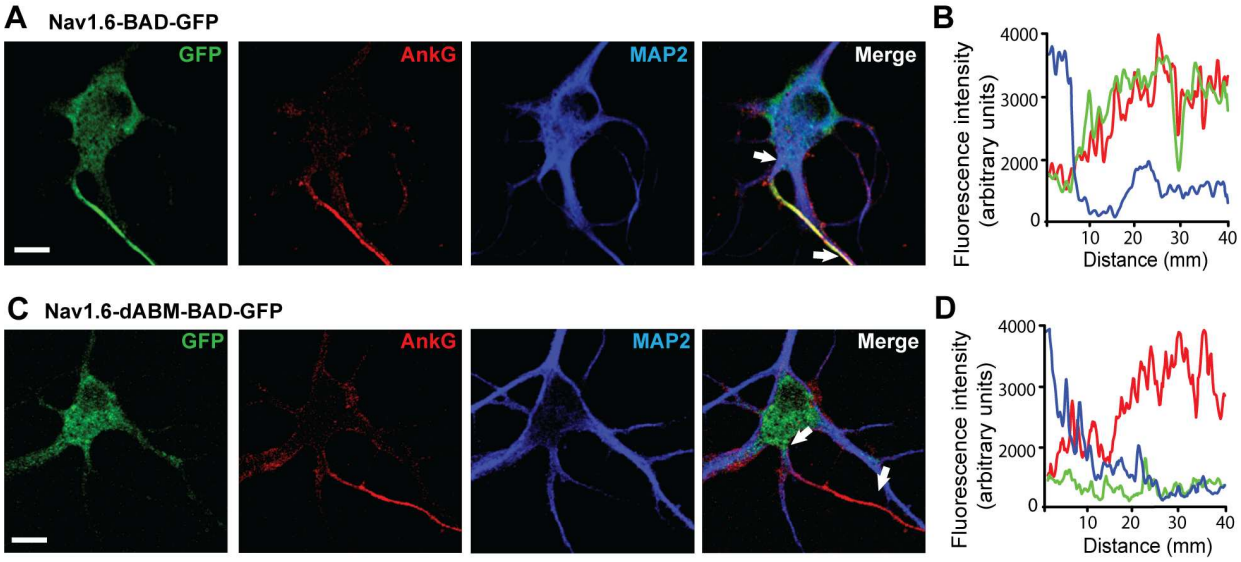

Fig 3.2. $Na_v1.6$-BAD-GFP but not $Na_v1.6$-dABM-BAD-GFP co-localizes with axonal markers

(A,C) Compression of confocal z-stacks of DIV8 rat hippocampal neurons co-transfected with ankG-mCherry and either wild-type $Na_v1.6$-BAD-GFP or $Na_v1.6$-dABM-BAD-GFP and immunolabeled for MAP2. **A)** $Na_v1.6$ is enriched within the ankG positive AIS. **B)** Line profile of the AIS showing the simultaneous increase of $Na_v1.6$ (green) and ankG (red) and the decrease of MAP2 (blue) with increasing distance from the soma. **C)** $Na_v1.6$-dABM-BAD-GPF is found throughout the somatodendritic region of the neuron, but is not enriched in the ankG positive AIS. **D)** Line profile of the AIS showing the increase in ankG (red) while the expression levels of the mutant $Na_v1.6$ (green) and MAP2 (blue) are low within the AIS. Scale bars represent 10 μm.

BAD tag was also inserted into a $Na_v1.6$ construct lacking the critical amino acids within the ankG-binding motif needed for ankG binding, amino acids 1094-1102 (Lemaillet et al., 2003) ($Na_v1.6$-dABM-BAD). Consistent with published data (Gasser et al., 2012), this channel showed no AIS accumulation with the SA-594 surface fluorescence evenly distributed throughout the soma and AIS, as marked by ankG-GFP (Fig. 3.1B). However, the puncta on the soma were still present indicating that an ankG-independent mechanism localizes $Na_v1.6$ channels on the soma surface (Fig. 3.1B, middle panel).

In order to establish the distribution of these $Na_v1.6$ constructs relative to the AIS we performed colocalization studies with ankG and MAP2 as illustrated in Fig. 3.2. AnkG concentrates at the AIS and is viewed as the AIS organizer (Jenkins and Bennett, 2001; Hedstrom et al., 2008), while MAP2 is found in dendritic processes and is dramatically reduced in the axon (Gasser et al., 2012). $Na_v1.6$-BAD-GFP channels clearly associate with the ankG positive and MAP2 negative AIS (Fig. 3.2A-B), while the $Na_v1.6$-dABM-BAD-GFP mutant does not (Fig. 3.2C-D).

$Na_v1.6$-BAD-GFP channels are localized to the AIS via direct insertion

As indicated in Fig. 3.3, once $Na_v1.6$-BAD-GFP channels have accumulated within the AIS of cultured hippocampal neurons channel turnover is slow. The illustrated FRAP studies of both cell surface and total $Na_v1.6$-BAD-GFP within the AIS indicates that there is only approximately 10% recovery of the GFP fluorescence over 25 min (7.5±0.2%, n=8 for DIV6; 9.7±1.8%, n=6 for DIV10; mean ± s.e.m.) while there is no detectable recovery of the surface-specific SA-594 fluorescence. Such limited recovery complicates study of AIS delivery in neurons where $Na_v1.6$ accumulation has reached steady state. For this reason we focused our

insertion site experiments on the delivery of nascent channels to the developing AIS in DIV6 neurons. Interestingly, we often observed mobile puncta, likely representing trafficking vesicles moving through the bleached region as illustrated in Fig. 3.3D.

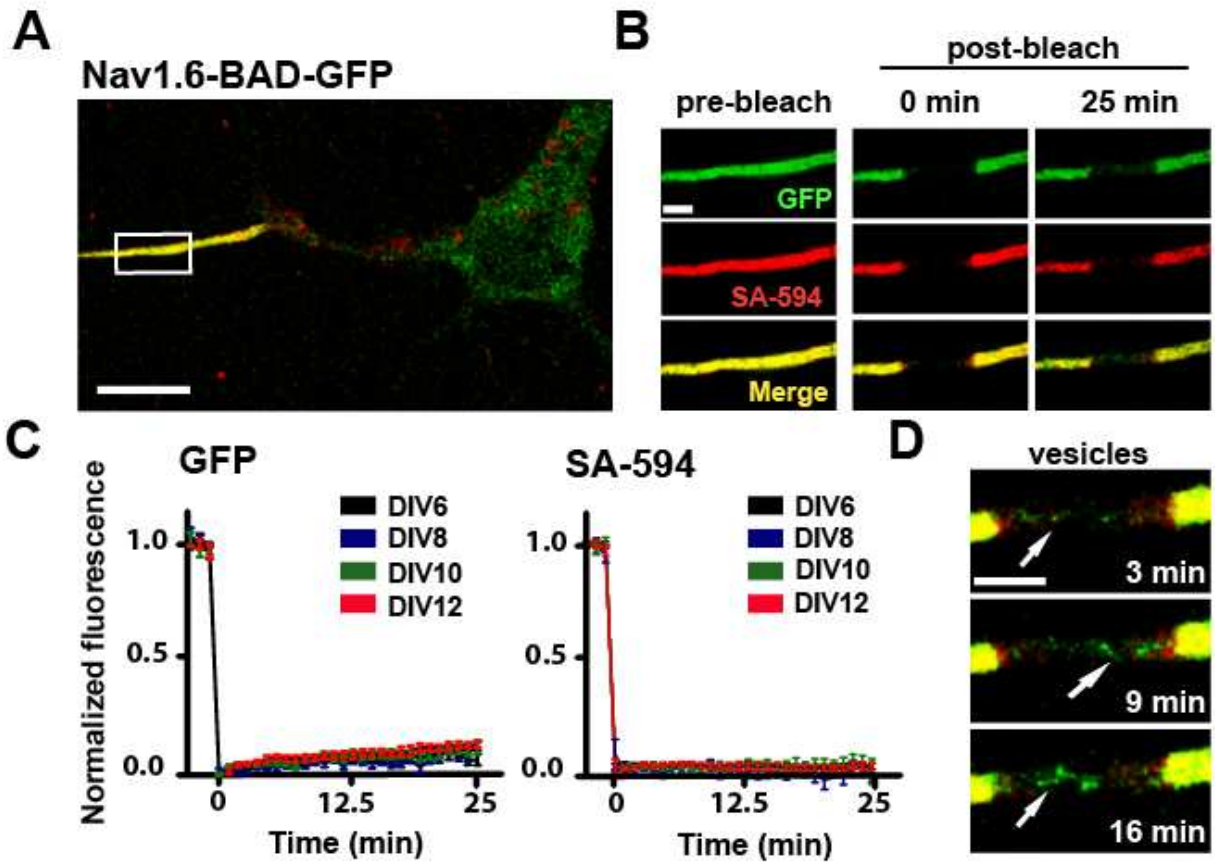

Fig 3.3. $Na_v1.6$ is stable in the AIS of mature neurons.
A) A representative compressed confocal z-stack of a DIV10 rHN expressing $Na_v1.6$-BAD-GFP. The high density of $Na_v1.6$ in the AIS is labeled both by the GFP fluorescence (green) and by surface labeling of the BAD tag via SA-594 (red). **B)** Enlargement of the white box in (**A**) showing fluorescence before photobleaching, immediately after photobleaching and 25 min postbleach. **C)** Average normalized FRAP curves over 25 min for the GFP fluorescence and surface-specific SA-594 fluorescence. Days post-transfection are indicated. On average, the GFP recovered 7.5±0.2%, n = 8, for DIV6 and 9.7±1.8%, n = 6, for DIV10 mean ± s.e.m.)Images were acquired every minute to minimize photobleaching during the recovery. D) Detection of mobile GFP-containing trafficking vesicles within the bleached AIS. The different time points illustrate the detection of dynamic puncta (arrows) at the indicated postbleach times. Scale bars represent 10 μm (A) or 2 μm (B,D).

Fig. 3.4A outlines the experimental approach for an optical pulse-chase experiment used to detect cell surface insertion sites. Briefly, NeutrAvidin (NA) was used to saturate available biotin binding sites on $Na_v1.6$-BAD-GFP channels already present on the neuronal surface. The unbound NeutrAvidin was then removed and SA-594 added to the bath during imaging. Thus, the spontaneous appearance of SA-594 fluorescence indicates a newly inserted channel. The advantage here is that the location of even a single newly inserted channel can be mapped since 1) our TIRF microscope readily detects single 594-SA molecules and 2) SA binding is rapid ($T_{1/2}$ < 75 sec) compared to the rate of membrane protein diffusion (Deutsch et al., 2012a).

Examples of delivery to both the soma and AIS are shown in Figs. 3.4C and 3.4D, respectively. The left panel of Fig. 3.4C shows a region of AIS membrane with two isolated puncta of SA-594 labeling (blue arrows) and the rest of the membrane devoid of SA-594 fluorescence. After 5 (yellow arrow) and then 35 (red arrow) seconds, new SA-594 puncta appear spontaneously. All puncta persist in the same location after their appearance. Both the spontaneous appearance of labeled channels and their immediate stability support the idea that $Na_v1.6$ channels are inserted directly into the AIS via direct trafficking. In contrast, SA-594 fluorescence that spontaneously appeared on the soma was often followed by rapid diffusion away from the site of channel insertion (Fig. 3.4D). The white trace (Fig. 3.4D, left panel) illustrates the single-molecule diffusion track over 13 sec after insertion at the red circle.

To visually represent the insertion events within the soma and AIS throughout the image sequence, a kymograph was created (Fig. 3.4E) corresponding to the line-scan indicated by the dashed line in Fig. 3.4B. The appearance of SA-594 molecules is seen along the length of the AIS, denoting insertion events. These particles persist over time as horizontal lines in the kymograph due to limited lateral movement, suggesting that they are immediately immobilized

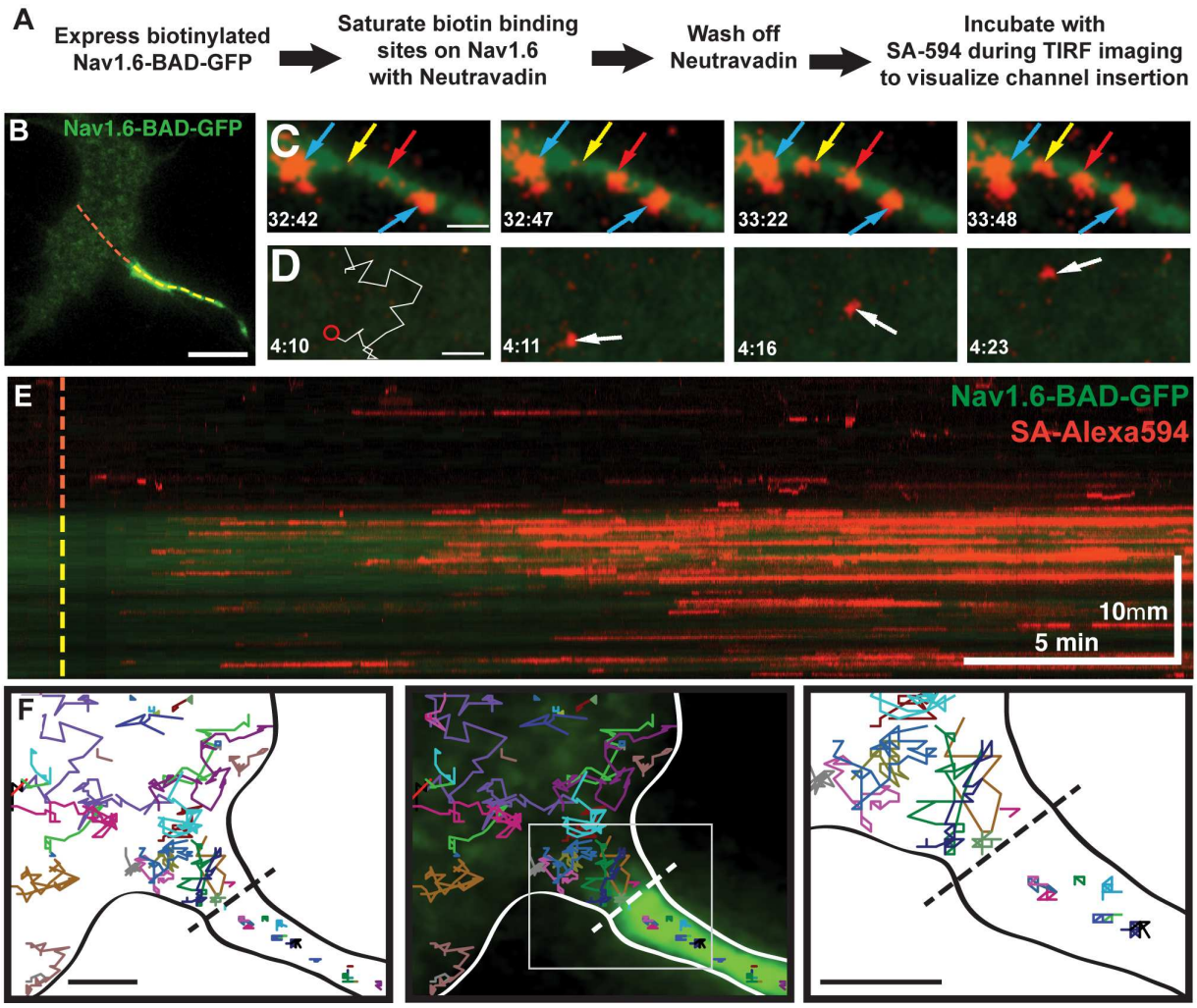

Fig 3.4. $Na_v1.6$-BAD-GFP is delivered along the length of the AIS where it is immediately immobilized.

A) Experimental outline. **B)** Representative TIRF image and reference for the Kymograph in (**E**). Dotted line indicates line scan starting in the soma (red) and continuing through the AIS (yellow). **C)** Representative images of SA-594 labeling of newly inserted channels in the AIS. Two SA-594 puncta appear in the axonal membrane previously devoid of surface labeling (yellow and red arrows), denoting insertion events. Two other puncta are present throughout this time course and show no lateral movement (blue arrows). **D)** Representative images of SA-594 labeling of newly inserted channels in the soma. The left panel shows the insertion site location (O) and subsequent single-molecule track overlaid on the region prior to the channel delivery at 4:11. **E)** Kymograph of the line scan shown in (**B**) indicating GFP (green) and SA-594 (red) fluorescence over time. **F)** Single-molecule tracking of inserted $Na_v1.6$-BAD-GFP. Each colored line represents an individual track. The black dotted line indicates the soma/AIS boundary. Neurons were transfected on DIV4 and imaged 36–44 hrs post-transfection. Scale bars represent 10 μm (B,E) or 2 μm (C,D,F).

after insertion. Had channels been localized to the AIS via diffusion from the soma, lines with a negative slope would have been obvious in the kymograph. Insertion events were seen in both the soma and AIS; however, there was a strong preference for the AIS. Out of 5 cells analyzed the number of insertion events in the AIS per μm^2 was 0.79±0.11, while the insertions in the soma were only 0.11±0.04 (mean±s.e.m.). Channels inserted into the somatic region were either mobile, as demonstrated by a brief appearance on the kymograph, or static and thus generating persistent horizontal lines. These behaviors are consistent with some somatic channels localizing to small puncta as observed in Fig. 3.1A.

While these data demonstrate that $Na_v1.6$ localizes to the AIS primarily through direct insertion, this does not exclude the possibility of diffusion trapping, i.e. mobile channels being trapped via ankG binding once entering the AIS, especially since we used DIV6 rHNs and the soma/AIS diffusion barrier is not well established until DIV10 (Nakada et al., 2003). To address this, we used single molecule tracking of newly inserted channels to inspect $Na_v1.6$ movement in the vicinity of the AIS/soma interface. Fig. 3.4F shows representative tracks from throughout the imaging sequence, demonstrating that while channels approached the AIS, none crossed the boundary. The diffusion coefficient for the mobile channels on the soma as calculated from mean square displacement analysis was 0.07 ±0.05 $\mu m^2/s$, n=20, in close agreement with previously determined values for mobile membrane proteins (Tamkun et al., 2007). The channels in the AIS membrane had diffusion coefficients of 0.0007±0.0006 $\mu m^2/s$, n=20, similar to previous reports of Na_v channels (Nakada et al., 2003) or $K_v2.1$-Na_v chimeras (Brachet et al., 2010) in the AIS. In summary, the data presented in Fig. 3.4 argue for preferential delivery to the AIS and immediate binding to ankG, with no direct evidence of diffusion trapping.

SA-594 binding requires temperatures permissive of trafficking

It is possible that the binding of SA-594 could be due to either dissociation of NA or incomplete block instead of delivery of proteins to the cell surface. To address this we performed an insertion site experiment at temperatures not permissive to intracellular trafficking. Fig. 3.5A-D shows neurons transfected with GFP-K_v2.1-BAD-Na_v1.2, a chimera with the Na_v1.2 ABM fused to K_v2.1 lacking its C-terminus (see Fig. 3.7). This protein is robustly expressed in neurons and has a relatively fast rate of channel recycling via endo- and exocytosis. Neurons incubated with SA-594 in the absence of NA block showed intense labeling, demonstrating the presence of

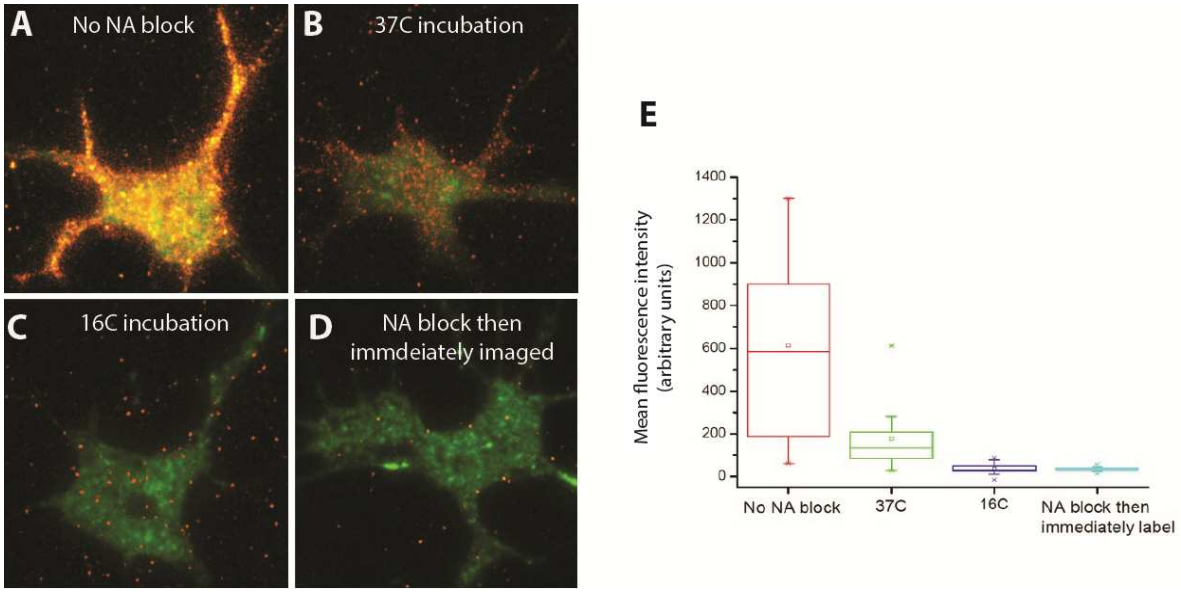

Figure 3.5 SA-594 binding after NA-block requires temperatures permissive of protein trafficking.

Neurons transfected with GFP-K_v2.1-BAD-Na_v1.2 were imaged in TIRF in the presence of SA-594 either without NeutrAvidin (NA) block **(A)** or after pre-incubation with NA **(B-D)** to block the biotin binding sites of channels present on the neuronal surface. **A)** Neurons imaged in the presence of SA-594 without NA block show robust SA-594 surface labeling of GFP-K_v2.1-BAD-Na_v1.2. **B-C)** GFP-K_v2.1-BAD-Na_v1.2 channels on the plasma membrane were blocked with NA, excess NA was removed, and neurons were incubated for 2 hrs at either **B)** 37ºC or **C)** 16ºC and then imaged in TIRF in the presence of SA-594. Neurons incubated at 37ºC, which is permissive of protein trafficking, showed SA-594 binding, while neurons incubated at 16ºC to preclude channel trafficking showed very little SA-594 labeling. **D)** Neurons incubated with NA and then immediately imaged in the presence of SA-594 showed binding levels not different than background. **E)** Box and whisker plots of average fluorescence intensity for each condition.

channels on the neuronal surface (Fig. 3.5A). To test for the effectiveness of NA block, surface channels were blocked with NA as in the $Na_v1.6$ insertion site experiment, the excess NA was removed, and the neurons were incubated for 2 hrs at either 37ºC (Fig. 3.5B) such that protein trafficking could occur as normal, or at 16ºC (Fig. 3.5C) which is a temperature not permissive of intracellular trafficking. The dishes were then bathed in SA-594 as during the insertion site experiment and imaged via TIRF microscopy. Neurons at the permissive temperature showed SA-594 binding, while neurons incubated at 16ºC showed almost no SA-594 over background. It was similar to the amount of labeling for neurons that were blocked with NA and then immediately incubated with SA-594 during imaging (Fig. 3.5D). Thus, the majority of SA-594 labeling during insertion site experiments is due to protein trafficking.

Insertion events simultaneously deliver multiple $Na_v1.6$ channels to the AIS

During the FRAP studies illustrated in Fig. 3.3D puncta of GFP fluorescence were often observed moving through the bleached AIS. These likely represent trafficking vesicles although we cannot conclude here that these represent cargo on the way to the cell surface. However, in the TIRF-based insertion site experiment the simultaneous appearance of multiple channels, which should be detected as multiple SA-594 molecules binding within the same delivery site, would be indicative of vesicular delivery to the plasma membrane. To investigate this, we first ascertained the average fluorescence intensity of single SA-594 labeled channels within the soma, identified by their distinctive, diffusive behavior in the plasma membrane (Fig. 3.4D). This produced a distribution with a mean of 863.3±295.7 a.u., n=110 (Fig. 3.6A). In contrast, puncta spontaneously appearing on the plasma membrane of the AIS and soma had fluorescence intensities as much as 6-fold greater than that of single molecules (Figs. 3.6B and 3.6C), with mean values of 1615.5±1030.7 a.u., n=53 and 1560.9±1134.3 a.u, n=50, respectively. These data

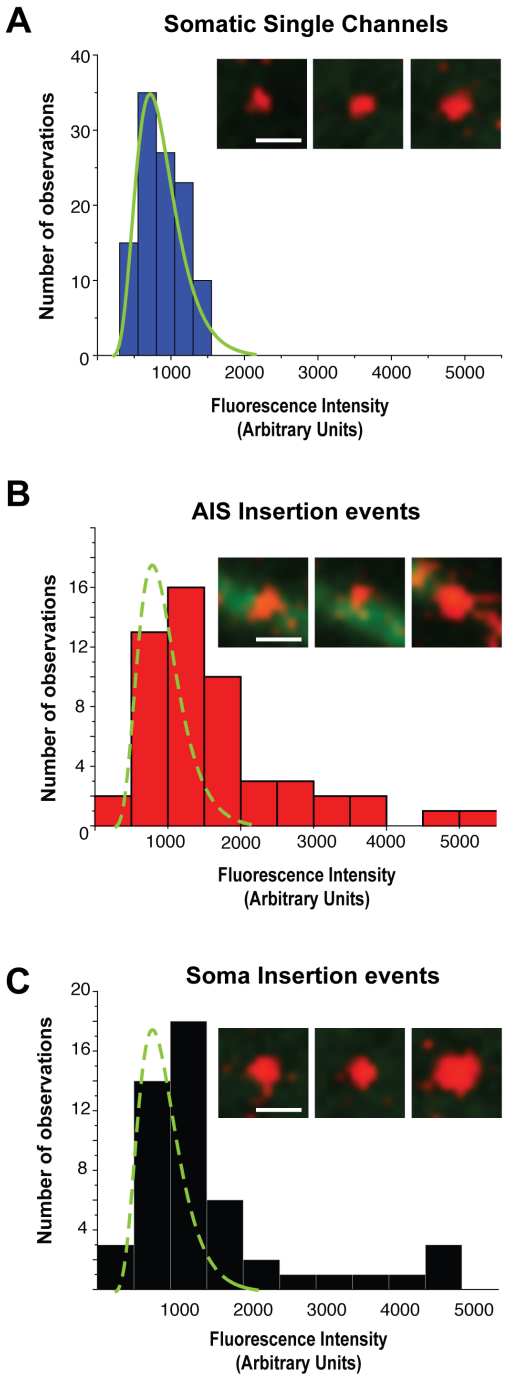

Fig 3.6. Simultaneous insertion of multiple channels into the plasma membrane.

A) Histogram of fluorescence intensity of SA-594 labeled $Na_v1.6$-BAD-GFP channels on the soma. Solid green line is a fit to the histogram distribution. (**B-C)** Fluorescence intensity of delivered channels in the AIS and soma, respectively. Dashed green line is the fit to the histogram distribution from panel A. Representative images are shown in the insets. Scale bars represent 1 μm.

are consistent with multiple SA-594 molecules binding rapidly following new channel insertion, with up to 6 channels per insertion event.

Preferential AIS delivery requires ankG binding

In order to address the role of ankG binding in the delivery of $Na_v1.6$ to the AIS, we repeated the insertion site assay (Fig. 3.4A) using the $Na_v1.6$ construct lacking the ankG-binding motif ($Na_v1.6$-dABM-BAD). To facilitate comparison, another insertion kymograph for the full-length $Na_v1.6$-BAD-GFP channel is presented in Fig. 3.7A-C. Similar to the kymograph in Fig. 3.4, $Na_v1.6$ insertion is most prominent in the AIS, with some SA-594 labeled channels present in the soma. Panel C shows an enlargement of the boxed region in the kymograph which highlights channel mobility on the soma as demonstrated by the vertical movement of the SA-594 signal (yellow arrow). This mobility is also apparent in the single molecule tracks of Panel D. Note that a short-lived SA-594 signal on the kymograph does not distinguish between channel movement, photobleaching, or internalization. In contrast to the full-length $Na_v1.6$, the kymograph illustrating surface delivery of the $Na_v1.6$-dABM-BAD mutant channel (Panel F) demonstrates that the preferential AIS insertion is lost upon deletion of ankG binding activity. Here the neurons were also transfected with ankG-GFP to mark the AIS. Overall, insertion events for the $Na_v1.6$-dABM-BAD channels were 0.18±0.01 per μm^2 in the AIS and 0.11±0.01 per μm^2 (mean±s.e.m.) in the soma. The corresponding single molecule tracks shown in Fig. 3.7H emphasize that the $Na_v1.6$-dABM-BAD mutant has increased mobility within the AIS as compared to the channel with ankG binding capability. The calculated diffusion coefficients from the mean square displacements were 0.09±0.06 $\mu m^2/s$ (n=10) for somatic channels and 0.03±0.03 $\mu m^2/s$ (n=10) for channels in the AIS. The reduced mobility within the AIS relative to

the soma for this ankG binding deficient channel is not surprising given the dense cortical cytoskeleton within the AIS (Xu et al., 2013).

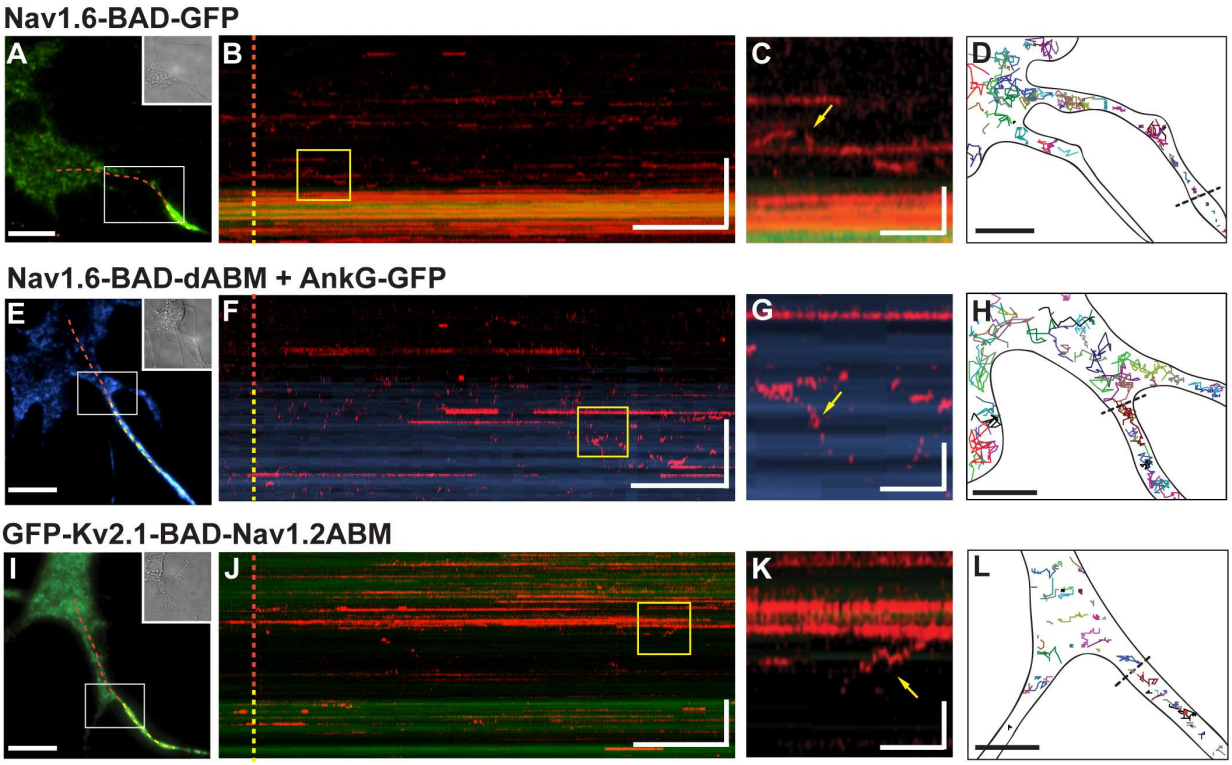

Fig 3.7. AnkG binding is necessary to confer directed delivery to the AIS.

Insertion site experiments were performed as outlined in Fig. 3.4A for hippocampal neurons transfected with either full-length $Na_v1.6$-BAD-GFP **(A-D)**, $Na_v1.6$-dABM-BAD and ankG-GFP **(E-H)**, or GFP-$K_v2.1$-BAD-$Na_v1.2$ABM **(I-L)**. **A,E,I)** Reference images for the kymographs with the dotted line indicating the line scan starting in the soma (red) and continuing through the AIS. **B,F,J)** Kymographs of line scans indicating location of newly inserted channels over time as indicated by SA-594. **C,G,K)** Enlargements of yellow boxes in kymographs. Immobile channels appear as persistent horizontal lines, while mobile channels are represented by the vertical movements (yellow arrows) in the kymograph or brief appearances as channels cross the line scan. **D,H,L)** Representative single molecule tracks illustrating channel mobility. The black dotted lines indicate the soma/AIS boundary. Neurons were transfected on DIV4 and imaged 36–44 hrs post-transfection for the $Na_v1.6$ constructs or 12–15 hrs post-transfection for the GFP-$K_v2.1$-BAD-$Na_v1.2$ABM construct. Scale bars for **A,E,I** represent 10 µm. Scale bars for **B,F,J** represent 2 min (horizontal) and 10 µm (vertical). Scale bars for **C,G,K** represent 15 sec (horizontal) and 3 µm (vertical). Scale bars for **D,H,L** represent 5 µm.

To assess whether the ankG binding domain alone is sufficient for preferential insertion in the AIS, we repeated the insertion site experiment with the K_v2.1-Na_vABM chimera used previously by the Dargent group (Bréchet et al., 2008; Brachet et al., 2010). These investigators demonstrated that this construct accumulates at the AIS due to its ankG binding activity. We inserted the BAD tag into the S1-S2 extracellular domain of K_v2.1 to create GFP-K_v2.1-BAD-Na_v1.2ABM (GFP-K_v2.1-BAD-Na_v1.2). As shown in Figs. 3.7I-K, the GFP-K_v2.1-BAD-Na_v1.2 chimera also lacks preferential insertion into the AIS and is robustly delivered to the cell surface, consistent with what was observed for the CD4-Na_vII-III chimera (Fache et al., 2004). Overall, insertion events per μm^2 were 0.31±0.06 in the AIS and 0.2±0.03 (mean±s.e.m.) in the soma. Both the single molecule tracks shown in Fig. 3.7L and the diffusion coefficients, 0.018±0.016 $\mu m^2/s$ (n=10) on the soma and 0.0025±0.0026 $\mu m^2/s$ (n=10) within the AIS, indicate that GFP-K_v2.1-BAD-Na_v1.2 has 10-fold lower mobility in the AIS as compared to the soma as previously described (Brachet et al., 2010). The data represented in Fig. 3.7 are summarized in Fig. 3.8.

3.4 Discussion

In this study we used a novel Na_v1.6 construct tagged with both GFP and an extracellular biotinylation domain to study the membrane delivery of the full-length Na_v1.6 protein during AIS development. The novelty of this construct lies in the ability to observe the total population of expressed channels via the GFP tag, while also being able to selectively label the subpopulation of surface channels via the biotinylated BAD tag. As summarized in Fig. 3.8 we found channel delivery to the plasma membrane directly within the AIS at a significantly higher density than in the somatodendritic region of the developing hippocampal neurons used in this study. Additionally, individually labeled channels showed almost no diffusion within the AIS after insertion, presumably due to immediate binding to ankG and the associated cytoskeletal

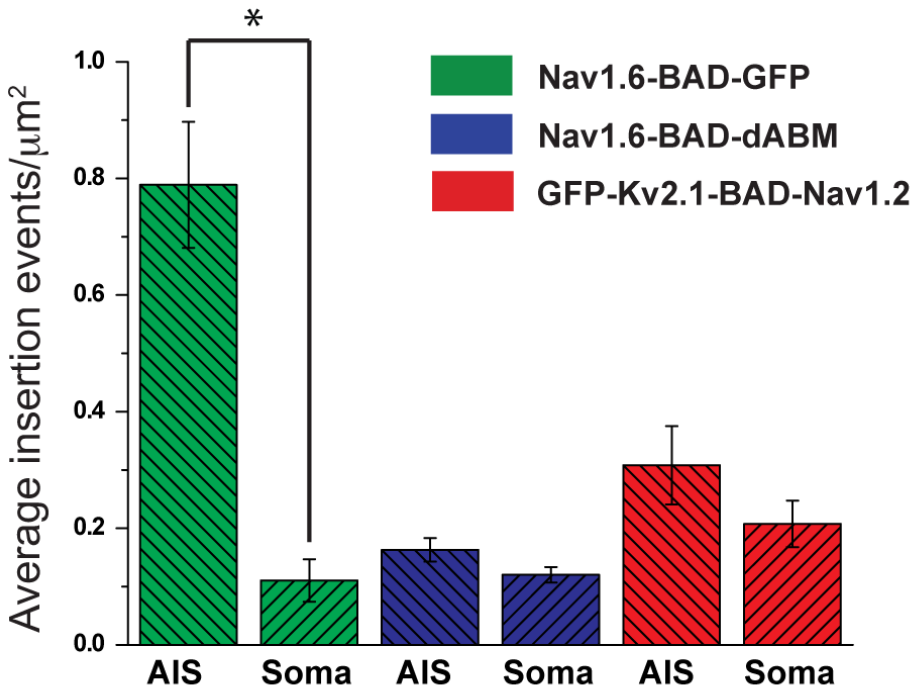

Fig 3.8. Summary of insertion events for the AIS versus soma.

Average insertion events for full-length $Na_v1.6$ (694 insertion events from 5 cells), $Na_v1.6$-dABM (265 insertion events from 5 cells), or the $K_v2.1$-$Na_v1.2$ chimera (618 insertion events from 5 cells). Numbers of insertion events were determined over a 5 min period for each region of the cell, then normalized to the surface area. Data shown as mean values ± s.e.m. Significance was determined using paired t-tests. * indicates $p = 0.00194$ for $Na_v1.6$-BAD-GFP. The differences for GFP-$K_v2.1$-BAD-$Na_v1.2$ were not significant, $p = 0.2$.

elements. Consistent with the idea of vesicular delivery of channels, we observed trafficking vesicles in the FRAP experiments and, in the insertion site experiments, the appearance of newly delivered puncta on the AIS with fluorescence intensities as much as 6-fold greater than that of a single channel. Our data are best explained by delivery of small quanta of channels to spatially discrete sites within the cell membrane at the AIS.

This preferential delivery is dependent on the ability of $Na_v1.6$ to bind ankG, as supported by our results from the $Na_v1.6$-dABM-BAD mutant. This finding agrees with the recent published results (Barry et al., 2014) demonstrating that ankG links Na_v channels to kinesin-1 and is essential for axonal targeting both in culture and *in vivo*. It appears that ankG

binding is only required for preferential delivery and not general trafficking, since non-selective delivery of the $Na_v1.6$-dABM-BAD channels to the cell surface was still observed.

As evidenced by the GFP-$K_v2.1$-BAD-$Na_v1.2$ chimera, ankG binding alone, while required for directed delivery of $Na_v1.6$ to the AIS, is not sufficient for preferential delivery to the AIS. Despite the lack of preferential delivery, this chimera is ultimately concentrated at the AIS (Brachet et al., 2010) and thus must use a different mechanism, such as selective endocytosis or diffusion trapping. Previous studies addressing Na_v localization mechanisms used a similar chimeric protein, CD4-Na_vII-III chimera (Fache et al., 2004). This construct also appeared on the soma surface only to be internalized within 20 min. These results led to a model in which Na_v channels are selectively internalized from the surface if they are not retained via ankG binding at the AIS (for a recent review see (Leterrier and Dargent, 2014). This model is consistent with our GFP-$K_v2.1$-BAD-$Na_v1.2$ chimera insertion data where this protein is inserted ubiquitously and then presumably endocytosed from the soma but retained in the AIS.

While our data suggest that the majority of the full-length $Na_v1.6$ channels arrive at the AIS via direct delivery, we were not able to address the possible contribution of selective endocytosis in enhancing their polarized distribution. Additionally, while it is likely that we were detecting the appearance of nascent channels on the plasma membrane, we were not able to directly address transcytosis in which channels are first inserted into the somatodendritic region, then endocytosed and subsequently delivered to the AIS. Future studies will investigate these mechanisms, as well as further examining the motors and exocytic machinery responsible for vesicular delivery.

Our study focuses on the establishment of the AIS, rather than its maintenance for several reasons. First, it is important to understand how $Na_v1.6$ channels are incorporated into the unique cytoskeletal and membrane network created in this region during its development. Additionally, once $Na_v1.6$ accumulates at the AIS turnover is very slow (10% over 25 min) as illustrated in Fig. 3.3. Consistent with the immediate immobilization of individual channels delivered to the AIS as illustrated in Fig. 3.4, the lack of surface channel (SA-594 fluorescence) recovery suggests that once $Na_v1.6$ is added to the surface it is anchored in place, showing little exchange with adjacent membrane. Thus, while our insertion site assay is useful for detecting the large bolus of $Na_v1.6$ channel delivered to the AIS during neuronal development, i.e. how the first wave of $Na_v1.6$ populates the AIS, new assays must be developed to be able to detect the much more subtle process of $Na_v1.6$ turnover during AIS maintenance. It is interesting to note, however, that even in the absence of a fully established diffusion barrier $Na_v1.6$ was not observed to localize to the AIS via diffusion trapping. This strongly suggests that the same trafficking method is used for mature neurons. Whether these results apply *in vivo* will require new technologies as present approaches for the mapping of cell surface delivery sites require a cell system suitable for high-resolution microscopy.

Our present study does not address the role of Na^+ channel beta subunits in $Na_v1.6$ delivery to the AIS, for the beta1 and beta2 subunits were transfected with the $Na_v1.6$ to ensure that they were always available. The role of beta subunits in the preferential delivery to the AIS clearly merits study since beta1 binds ankG (Malhotra et al., 2002) and beta1 null mice show no $Na_v1.6$ at the AIS even though $Na_v1.1$ is up-regulated here (Brackenbury et al., 2010). It is possible that a role for beta subunits might explain the lack of $K_v2.1$ABM construct delivery to the AIS.

Another unresolved question is related to the nanoscopic organization of the cytoskeleton at the AIS plasma membrane. A recent study elegantly examined actin and spectrin structure at the AIS with super-resolution techniques (Xu et al., 2013). Actin rings approximately 100 nm apart (seen in DIV5-7 neurons) are linked by a dense spectrin mesh that at first glance should block even 50 nm vesicles from reaching the cell surface. The most parsimonious explanation to reconcile the presence of a rigid structure and directed AIS delivery is to suggest that the AIS cytoskeleton is dynamic, with transient and localized breakdown in this cytoskeletal collar allowing exocytosis. However, it is noteworthy that platinum replica electron microscopy (Jones et al., 2014) has not detected dense actin meshworks in the AIS, underscoring the need for further study.

Direct vesicular delivery at the AIS provides a mechanism that can effectively establish sodium channel localization within this critical neuronal compartment. This mechanism of localized exocytosis avoids the soma/AIS plasma membrane diffusion barrier. In addition, a diffusion-trap mechanism is unreliable given the dense membrane and cytoskeletal architecture within the AIS itself (Xu et al., 2013), especially when considering the cytoplasmic mass of Na_v channels and potential association with cytosolic proteins. Direct delivery of Na_v channels to the AIS is a means of precisely controlling number, isoform, and location, and thus, the establishment of the proper environment for action potential initiation.

Chapter 4

Single-molecule imaging of $Na_v1.6$ on the soma of cultured hippocampal neurons reveals unique somatic nanoclusters

4.1 Introduction

Proper neuronal communication is reliant on both the proper complement of ion channels and their precise subcellular localization within the neuronal membrane. In particular, a high density of voltage-gated sodium (Na_v) channels at the axon initial segment (AIS) is essential for action potential initiation (Zhou et al., 1998; Boiko et al., 2003; Meeks and Mennerick, 2007; Kole et al., 2008). As such, neurons are polarized cells with vastly different machinery and molecular organizations between the AIS and somatodendritic regions including unique protein, cytoskeletal, and lipid components (Ohura and Kamiya, 2015). Due to the functional importance of the AIS and high density of proteins, the structural and functional aspects of this neuronal subcompartment have been highly studied in relation to its somatic counterpart.

The presence of somatodendritic Na_v channels has been demonstrated by functional methods including electrophysiology and fluorescent Na+ indicators (Hu et al., 2009; Fleidervish et al., 2010; Gorelova and Seamans, 2015). Cell attached patch clamp suggests a heterogeneous distribution of Na_v channels throughout the somatic membrane (Williams and Stuart, 2000). Localized application of the sodium channel blocker tetrodotoxin (TTX) diminishes action potential backpropagation, suggesting that these channels are important for relaying information about AIS output to the rest of the neuron. These signals are postulated to enhance associative synaptic plasticity. In nigral dopamine neurons, the somatodendritic Na_v channels, compared to AIS Na_v channels, are specifically involved in regulating repetitive firing frequency in this cell

type (Tucker et al., 2012). There is also precedence that Na_v channels in the AIS and somatodendritic compartments are differentially regulated. Activation of D1/D5 dopamine receptors in prefrontal cortex pyramidal neurons preferentially modulates Na_v channels in the soma and proximal dendrites, increasing the amount of persistent current (Gorelova and Seamans, 2015).

Despite the functional importance of Na_v channels in this neuronal compartment, the distribution and live-cell dynamics of somatodendritic Na_v channels have been elusive. Traditional immunofluorescence-based assays are not sensitive enough to detect the sparse protein distribution of Na_v channels in the soma (Kole et al., 2008; Hu et al., 2009; Tian et al., 2013). The highly sensitive method of quantitative electron microscopy (EM) using immunogold labeled SDS-digested freeze-fracture replica-labeling (SDS-FRL) has provided the best demonstration that $Na_v1.6$ is present in the soma and dendrites of hippocampal CA1 pyramidal cells (PC), although at a density approximately 40 times lower than that in the AIS (Lorincz and Nusser, 2010).

The localization and dynamics of proteins provides important information on protein and neuronal function. Basic biology is driven by molecular interactions and thus the specific localization as well as mobility of proteins, such as Na_v channels, can provide immense insight into protein function and regulation. The early fluid mosaic model suggested that membrane proteins in the lipid bilayer are generally freely mobile and lack specific organization (Singer and Nicolson, 1972). Further studies into membrane dynamics quickly demonstrated that the plasma membrane is actually highly ordered and protein diffusion in membranes is quite complex. Our current understanding is that the plasma membrane is structured such that molecular movement is influenced in a manner to increase the likelihood of relevant protein-protein interactions. This

is achieved through several different mechanisms including macromolecular crowding, compartmentalization by the actin cytoskeleton, and local lipid environments. The presence of a dense number of proteins restricts the ability of any one protein to diffuse freely, establishing localized domains within the membrane (Banks and Fradin, 2005; Mika and Poolman, 2011). Additionally, actin filaments present adjacent to the inner leaflet of the plasma membrane form compartments by creating physical barriers to integral membrane proteins, termed the picket and fence model (Ritchie et al., 2003; Kusumi et al., 2005). The larger the cytoplasmic domain of membrane proteins, the more the diffusion is hindered by such compartmentalization. Other mechanisms of protein localization are through protein-protein interactions such as self-organization (Sieber et al., 2007), interactions with anchoring proteins (Brachet et al., 2010), or protein-protein or protein-lipid interactions between the plasma membrane and the endoplasmic reticulum (Hogan et al., 2010; Wu et al., 2014; Fox et al., 2015). Further membrane complexity arises through unique lipid domains in the plasma membrane that some proteins may prefer over other regions (Kraft, 2013).

Protein movement has been studied through a variety of techniques. At the most crude level, fluorescence recovery after photobleaching (FRAP) shows the mobility of a protein population as a whole. This method often cannot accurately distinguish between mobile and immobile fractions and thus averages out the heterogeneity of behavior within and between individual proteins. Single-particle tracking, or visualization of a fluorescent tag bound to an individual molecule, provides much more precise information about molecule behavior, and thus insight into the complex factors and interactions that are influencing its behavior. However, single-particle tracking has its own limitations including the fact that generally a small fraction of the population can be imaged due to the need of spatial separation of fluorescent probes for

accurate tracking. Additionally, most single-particle tracking data is analyzed using mean squared displacement (MSD) as a function of time. These types of data are then used to determine diffusion coefficients and domain sizes based on individual tracks such that molecular movements can be described in terms of free, or Brownian, motion, directed transport, confined movement, or anomalous diffusion.

New techniques for both data acquisition and analysis have provided a multitude of additional information about the forces influencing protein distribution and mobility. One such approach, single-particle tracking photoactivation localization microscopy (spt-PALM), combines the sensitivity of traditional single-particle tracking with information from the entire population, as with FRAP (Manley et al., 2008). In essence, it preserves information about the heterogeneous motion of individual molecules with high spatiotemporal resolution, while acquiring information from a large subset of the population. This is achieved through the use of photoconvertible fluorescent proteins such as Dendra2. A low intensity activation laser is used to photoconvert this fluorescent protein from green to red emission, and a high intensity imaging laser is used for visualization and tracking the photoactivated red proteins until they photobleach. By balancing the levels of photoconversion to photobleaching, a renewable subset of activated molecules are maintained in the plasma membrane where they can be imaged and tracked, resulting in high-density tracks. Analyzing this type of data using a Bayesian inference scheme to spatially map cellular forces also provides much more information than a typical MSD analysis (Masson et al., 2014; El Beheiry et al., 2015). Instead of averaging over the entire trajectory of each molecule, and thus averaging out different motions, this type of analysis both considers each part of an individual molecule track such as transitions between free diffusion and confinement. This can help elucidate the concerted effect of factors such as friction and protein-

protein interactions on protein movement. This powerful technique can be used to map the factors influencing protein distribution and dynamics in a living cell.

Technical limitations have hindered the visualization of both the distribution and live-cell dynamics Na_v channels in the soma of neurons. Here we use a $Na_v1.6$ construct containing extracellular and fluorescent-protein tags to visualize these proteins in cultured hippocampal neurons. To the best of our knowledge, this is the first analysis of an individual Na_v channel isoform within the neuronal soma. Using the extracellular tag, we visualized the distribution of $Na_v1.6$ in live cells and found that the channels are distributed heterogeneously, often localizing to small membrane domains, or nanoclusters. Channels within these domains appear to be stably bound on the order of minutes to hours. $Na_v1.6$ channels localized outside of nanoclusters tend to be mobile. spt-PALM based analysis of $Na_v1.6$-Dendra2 demonstrated that channel mobility decreases as the neurons mature. The nanoclusters can be modeled as energy wells, or regions of the membrane where the energy barrier is low, and the depth of these interactions increase with neuronal age. The nanoclusters appear to be both actin and ankG independent, suggesting a novel Na_v localization mechanism within this neuronal sub-compartment. We postulate that these nanoclusters represent sites of channel regulation, potentially contributing to the functional differences seen between somatic and axonal Na_v channels.

4.2 Methods

Cell culture

Neuronal cultures were used as previously described (Akin et al., 2015). Animal use was according to protocols approved by the Institutional Animal Care and Use Committee of Colorado State University (Animal Welfare Assurance Number: A3572-01). This Institutional

Animal Care and Use Committee (IACUC) committee specifically approved this study. Embryonic hippocampal tissue was collected after anesthesia with isoflurane followed by decapitation. E18 rat hippocampal neurons were plated on glass-bottom 35mm dishes (MatTek, Ashland, MA, USA) that had been previously coated with Poly-L-lysine (Sigma-Aldrich, St. Louis, MO, USA). Neurons were grown in Neurobasal Medium (Gibco/Thermo Fisher Scientific, Waltham, MA, USA) with penicillin/streptomycin antibiotics (Cellgro/Mediatech, Inc., Manassas, VA, USA) and NeuroCult SM1 Neuronal Supplement (STEMCELL Technologies, Vancouver, BC, Canada).

Transfection

The $Na_v1.6$ constructs $Na_v1.6$-BAD-GFP and $Na_v1.6$-BAD-dABM were used as described in chapters II and III and (Akin et al., 2015). For $Na_v1.6$-Dendra2, the GFP from $Na_v1.6$-GFP was replaced with Dendra2 using KpnI and PacI restriction sites. Neuronal transfections were performed after days in vitro (DIV)4–6 in culture as indicated for each experiment using Lipofectamine 2000 (Invitrogen, Life Technologies, Grand Island, NY, USA) and either $Na_v1.6$-BAD, $Na_v1.6$-Dendra2, or $Na_v1.6$-BAD-GFP (1μg), human β1 in pcDNA3.1Mygro(+), and rat β2 in pcDNA3.1VS-HisTopoTA as indicated. For the $Na_v1.6$-BAD-GFP or $Na_v1.6$-BAD constructs, pSec-BirA (bacterial biotin ligase) was co-transfected to biotinylate the channel. For co-localization studies, clathrin-light chain-GFP (100ng) or GFP-$K_v2.1$ (500ng) was co-transfected with $Na_v1.6$-BAD.

Live-cell surface labeling

For experiments using a $Na_v1.6$ construct containing a BAD-tag, surface labeling was performed before imaging. Neurons were rinsed with neuronal imaging saline (NIS) to remove the Neurobasal media, as it could contain enough free biotins to prevent labeling of the channel with streptavidin-conjugated fluorophores, and then incubated for 10 min at 37°C with the indicated streptavidin-conjugated fluorophore, either streptravidin-conjugated Alexa594 (SA-594) (Molecular Probes, Life Technologies, Grand Island, NY, USA) or CF640R-streptavidin (Biotium, Hayward, CA, USA), diluted 1:1000 in (NIS). Excess dye was removed by rinsing with imaging saline. CF640R was used for far-red imaging instead of streptavidin-conjugated Alexa647 since the latter does not label $Na_v1.6$-BAD well. Alexa647 has a higher molecular weight than either SA-594 or CF640R, suggesting that the biotin within the BAD domain is accessible to dyes only under a certain size. For spt-PALM and actin super-resolution experiments, neurons were incubated with TetraSpeck beads (Molecular Probes, Life Technologies, Grand Island, NY, USA) diluted 1:1000 in imaging saline for 10 min such that several beads were visible within the field of view around most neurons. TetraSpeck beads are bright, photostable, and fluoresce at multiple wavelengths and thus are used as fiduciary markers to correct for drift during long image sequences.

Microscope

TIRF images were acquired using a Nikon Eclipse Ti Perfect-Focus equipped TIRF/wide-field fluorescence microscope as described previously (Fox et al., 2013). The TIRF microscope is equipped with AOTF-controlled 405, 488, 561, 647 nm diode lasers, 100 mW each, and an Intensilight wide-field light source. A 100x PlanApo TIRF, 1.49 NA, objective was

used for image acquisition. Emission was collected through a Sutter Lambda 10–3 filter wheel containing the appropriate bandpass filters. This microscope is equipped with the Andor iXon EMCCD DU-897 camera, 512x512. Neurons were imaged at 37°C using a stage and objective heater.

Fluorescence recovery after photobleaching (FRAP)

Neurons transfected with ankG-GFP and $Na_v1.6$-BAD were imaged in TIRF. $Na_v1.6$-BAD channels present on the neuronal surface were labeled with CF640R prior to imaging. Neurons were imaged every 5 sec for 2 minutes to establish a baseline. Then the microscope photoactivation unit (PAU) was used to apply high intensity laser to a small region on the neuronal membrane for ~10sec, or until the region was photobleached. Images were taken every 5 sec for an additional 30 min to observe recovery of the bleached region. The low imaging rate minimized photobleach during the recovery period.

spt-PALM imaging

The experimental details for the spt-PALM data are outlined in Fig. 4.1. DIV7, 10, or 15 rHNs expressing $Na_v1.6$-Dendra2, $Na_v1.6$-Dendra2-dABM, or CD4-Dendra2 were imaged using TIRF microscopy. Images of the unconverted Dendra2 and DIC images of the neuron were acquired both pre- and post- imaging. The TIRF angle was adjusted slightly for each cell to maximize the signal-to noise. Dendra2 was photoconverted with low-level 405nm laser (0.1%-1%) and photoconverted molecules were excited and imaged using high-intensity (100%) 561 nm laser. The 405 laser intensity was adjusted such that a steady-state level of photoconverted Dendra2 molecules were present, i.e. when photoactivation and photobleaching were balanced. Image sequences of 10,000 frames were acquired at 20 Hz for each cell.

1. Transfection

- Transfect neurons with $Na_v1.6$-Dendra2, $Na_v1.6$-Dendra2-dABM, or CD4-Dendra2

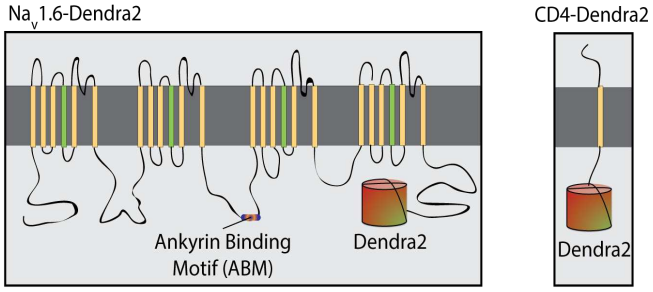

2. Imaging

- TIRF microscopy
- 10,000 frame aquisitions at 20Hz

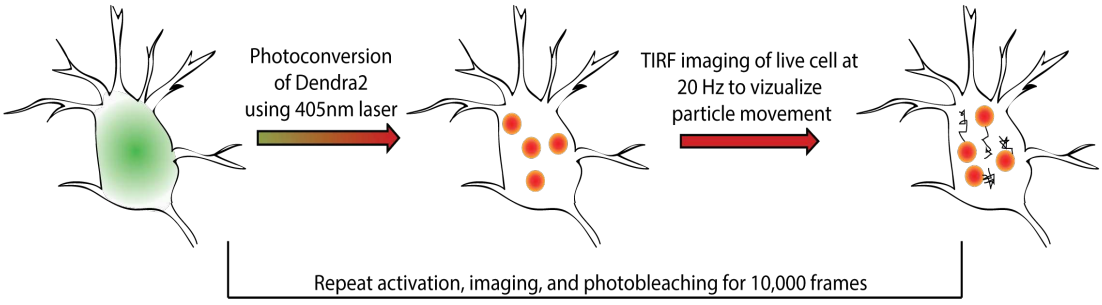

3. Image processing
ImageJ

- Subtract background
- Gaussian blur

4. uTrack detection and tracking
MATLAB

- Determination of partical location per frame
- Particle linking frame-to-frame to create track segments
- Gap closing, merging, and splitting to create complete tracks

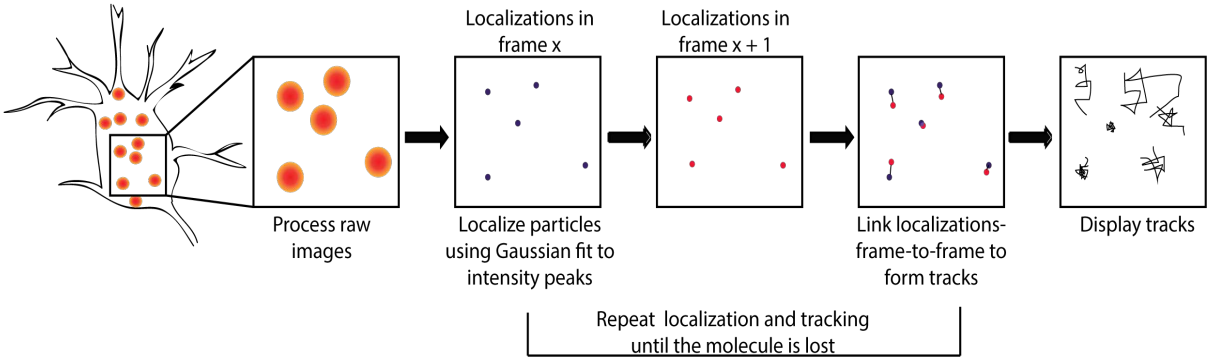

5. Data conversion
LabVIEW

- uTrack output is in XYI (x and y coordinents and intensity)
- Data is converted into TrXYT (track number, x and y cooridients, and time)

6. Drift correction
LabVIEW

- Tetraspec beads used as fudiciary markers are tracked
- Average movement over the imaging time are corrected for each track

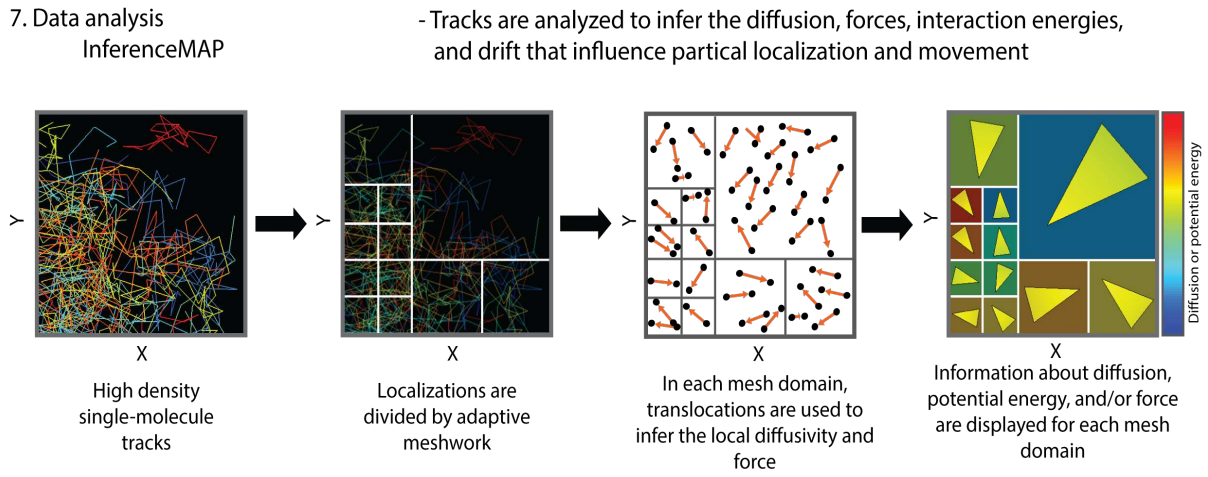

Figure 4.1. Experimental details for spt-PALM data acquisition and analysis.

1) Cultured hippocampal neurons are transfected with Dendra2 tagged proteins on DIV4-6 and imaged on DIV7, 10, or 15. Diagrams show how $Na_v1.6$ and CD4 are both tagged on their intracellular c-terminus. Note that $Na_v1.6$ is a large, 24-pass transmembrane protein while CD4 is a single-pass. **2)** Transfected neurons are found in TIRF. The green represents Dendra2 in its unconverted state as imaged with the 488nm-laser. Image sequences are then taken in the presence of low 405nm laser to photoconvert a small subset of the Dendra2 molecules (red dots) while 561nm laser is used to excite and detect the molecules. 10,000 frames are acquired at 20Hz to capture molecule movement (black lines). **3)** Image sequences are imported into ImageJ where the raw data is processed to enhance molecule detection. **4)** Processed images are then analyzed using the automatic tracking program uTrack in MATLAB. For details see (Jaqaman et al., 2008). The fluorescence of individual molecules is fit with a two-dimensional Gaussian. The center of the fit yields the position of single molecules. Molecule locations are determined for each frame, and then linked frame-to-frame. Smaller track segments are then combined through gap closing, merging, and splitting. **5)** The tracking data is ultimately analyzed using InferenceMAP, which requires data in the format of TrXYT (track number, x and y coordinate, and time). The output from uTrack is converted to this format using a custom LabVIEW code. **6)** Thermal drift during the time course of imaging is corrected by measuring the displacement of TetraSpeck beads present in the field of view during image acquisition. The beads are tracked and the average drift applied to the TrXYT data using custom LabVIEW codes. **7)** spt-PALM data is analyzed using InferenceMAP. For details see (El Beheiry et al., 2015). The high-density single-molecule localizations are plotted in x and y. Localizations of each molecule are connected by lines, each color representing a different single-molecule track. The tracks are then divided by a meshwork. Information about the diffusion and forces of molecules are assumed to remain constant within each mesh domain. Particularly in instances when particle localization is heterogeneous through the membrane region sampled, it is important to try to equalize the localization density throughout the mesh. The example shown here uses an adaptive meshwork, Quad-tree Meshing, in which subzones (leaves) are generated. If a grid contains more localizations than the defined capacity, it is subdivided into 4 identical zones. The translocations (orange arrows) within each zone are then analyzed. Each translocation contains information about particle diffusion (distance the particle moves between images) and the force (direction of movement) for each particle. Averaging the information from each mesh domain gives a measure of diffusivity and force (gradient of the potential). This is then used to make maps of the membrane regions studied.

spt-PALM image processing and tracking

Images were background subtracted and a Gaussian filter was applied to image sequences using ImageJ. Tracking analysis of the movies was carried out using the uTrack algorithm (Jaqaman et al., 2008). Fluorescence spots corresponding to single emitting fluorophores were fit with a two-dimensional Gaussian. The center of the fit yielded the position of single molecules and trajectories were then computed by linking detections frame-to-frame using the uTrack algorithm (Danuser Lab) in MatLab. These tracks were drift corrected by using the TretraSpeck beads present during imaging as fiduciary markers. Custom-made LabView codes written by Diego Krapf were used for this correction.

spt-PALM data analysis

Analysis of diffusion and potential energy landscapes used the program InferenceMAP program which employs a Bayesian inference scheme (for details see El Beheiry et al., 2015). This method is able to map the physical interactions that influence molecule movement, as well as being able to distinguish the type of physical interaction encountered. This includes diffusion, forces (directional biases), interaction (potential) energies, and drift. This method of analysis is also able to determine the strength of molecule interactions.

Super-resolution localization microscopy

Neurons were transfected with $Na_v1.6$-BAD and photoactivatable-GFP-actin (paGFP-actin). Before imaging, $Na_v1.6$-BAD was labeled with CF640R as described above. Transfected neurons were imaged in TIRF. First, $Na_v1.6$-BAD channels were imaged to determine their surface distribution. Then photoactivation localization microscopy was used to localize the actin

filaments in close proximity to the plasma membrane. paGFP is converted from a non-fluorescent state to a fluorescent state in the presence of 405 nm laser. The cells were exposed to low levels of 405nm-laser to photoconvert a subset of paGFP-actin, while molecules were visualized and subsequently photobleached using high intensity 488nm laser light. Molecule localizations were determined and super-resolution images of actin localization were reconstructed using the ImageJ plugin ThunderSTORM (Ovesný et al., 2014). TIRF images of $Na_v1.6$-BAD (non-super-resolution) were overlaid on the super-resolution image of actin. TetraSpeck beads were used as fiduciary markers to correct for drift.

Actin depolymerization

Neurons were transfected with $Na_v1.6$-BAD and ruby-Lifeact (gift from Dr. James Bamburg, CSU). The surface distribution of $Na_v1.6$-BAD was visualized using surface labeling of CF640R. Transfected neurons were localized in TIRF, and imaged every 1 min for ~10min to establish a baseline. 200nM swinholideA, an actin depolymerizing drug, was added to the bath. Successful depolymerization of actin was monitored using ruby-Lifeact. Lifeact is a 17-amino-acid peptide that preferentially bind filamentous actin (F-actin) structures (Riedl et al., 2008). Neurons were imaged every 1 min for an additional hour to determine the effect of actin depolymerization on $Na_v1.6$-BAD distribution.

4.3 Results

Somatic $Na_v1.6$ has a heterogeneous distribution

In order to investigate the distribution and dynamics of $Na_v1.6$ in living cells, we transfected cultured rat hippocampal neurons (rHNs) with a modified $Na_v1.6$ construct, $Na_v1.6$-

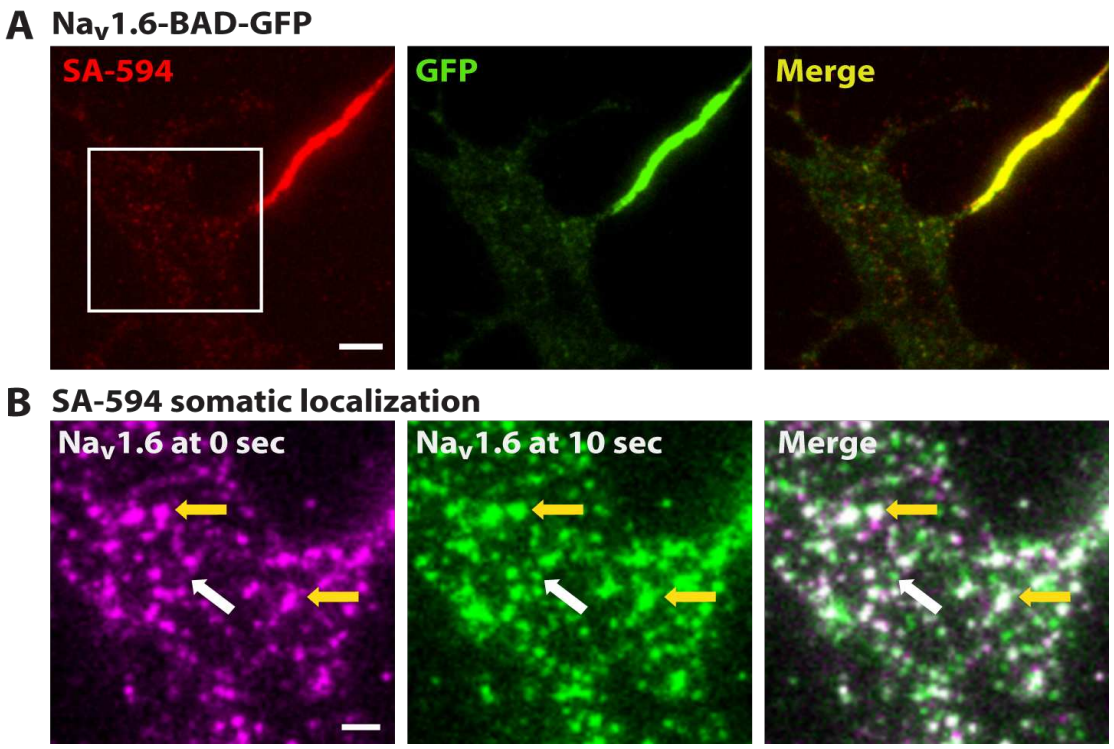

Figure 4.2. Na$_v$1.6 is distributed heterogeneously in the somatic membrane.

A**)** Na$_v$1.6-BAD-GFP is highly enriched at the AIS as indicated both by total expressed protein (green) and surface expression (red) visualized by live cell labeling with SA-594. Channels within the somatic region (white box) are barely visible at this contrast. **B)** Enlargement of white box in **(A)**. Contrast has been enhanced to visualize the somatic channels. Panels represent two frames of an images sequence spaced 10 sec apart. Overlay of the first frame (magenta) and the subsequent frame (green) is shown in the far right panel. Co-localization appears white. Large, bright puncta appear in the same location in both image sequences (yellow arrows), while smaller puncta demonstrate mobility (white arrow). Scale bars are 5 µm **(A)** and 2 µm **(B)**.

BAD-GFP as described in chapters 2 and 3 and in Akin et al, 2015. This construct encodes a modified Na$_v$1.6 tagged with a GFP and an extracellular biotin acceptor domain (BAD) that allows live-cell labeling of surface channels using streptavidin-conjugated fluorophores. Fig. 4.2A shows a cultured hippocampal neuron transfected with Na$_v$1.6-BAD-GFP, labeled with streptavidin-conjugated Alexa594 (SA-594), and imaged in TIRF. Both the extracellular label (left panel) and the GFP (middle panel) show that Na$_v$1.6 is localized to the AIS at a high density.

Previous reports have shown an AIS to soma ratio of approximately 35 (Lorincz and Nusser, 2010; Akin et al., 2015). Due to this difference in channel density, the fluorescence intensity of channels within the AIS overpowers the relatively sparse distribution of channels within the somatic region such that they are hardly visible when the image is contrasted for the AIS. Fig. 4.2B corresponds to an enlargement of the white box in Fig. 4.2A. The contrast has been optimized for visualization of the somatic channels. Here we see that the somatic channels are distributed non-uniformly. The channels display both mobile and non-mobile behavior on the neuronal surface. This behavior is illustrated by overlaying different frames of the movie that have been pseudo-colored either magenta or green and then overlaid such that immobile proteins that persists in the same location are co-localized between frames and appear white, while mobile channels appear either magenta or green. Fig 4.2B shows somatic channel distribution at two different timepoints separated by 10 sec (left panel, pseudo colored in magenta, first frame; middle panel, pseudo colored in green, later frame). The merge of these frames (right panel) demonstrates the presence of bright, white puncta (yellow arrow) and smaller colored puncta (white arrow), representing the immobile and mobile populations, respectively. The immobile puncta are much brighter and larger than the mobile ones, suggesting that these represent multiple channels localized to distinct, stable regions, or nanoclusters, within the somatic membrane with individual channels diffusing throughout the membrane.

$Na_v1.6$ localizes to stable somatic nanoclusters

Fig. 4.2B demonstrates the presence of nanoclusters as imaged over a relatively short timescale (10 sec). To demine the timescale over which $Na_v1.6$ channels remain stably localized within these membrane domains, we imaged the surface distribution of $Na_v1.6$ as visualized by a surface label for 30 min. Additionally, we were interested in the turnover of proteins within the

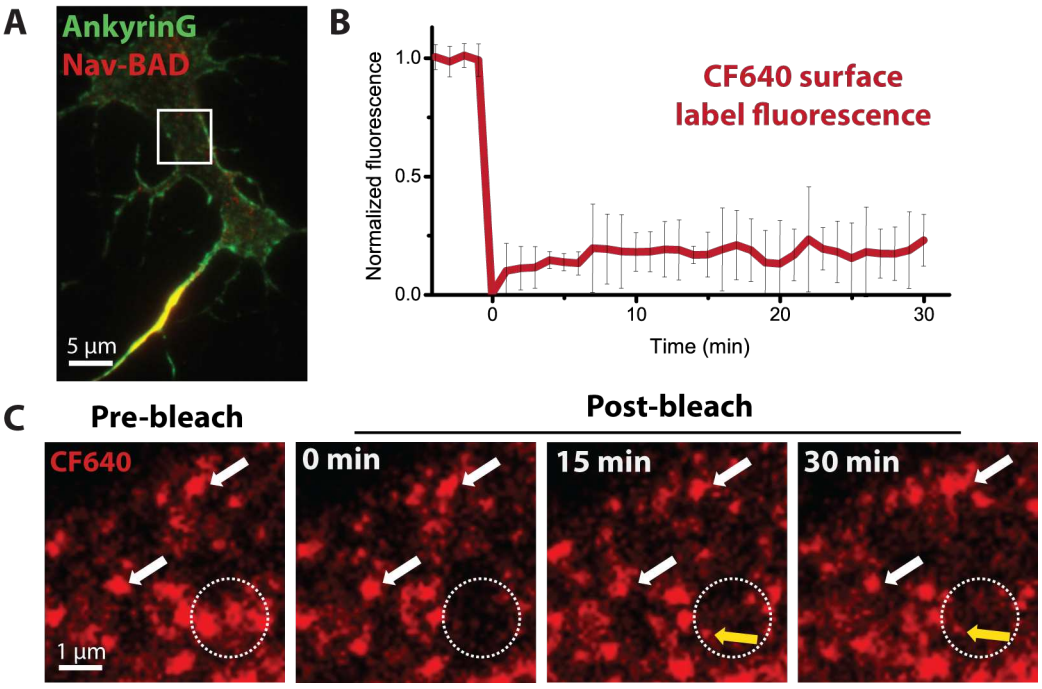

Fig 4.3 $Na_v1.6$ is stable in the AIS of mature neurons.

A) A representative TIRF image of a DIV10 rHN expressing $Na_v1.6$-BAD and ankyrinG-GFP to mark the AIS. Surface channels of $Na_v1.6$-BAD were labeled with CF640. **B)** Average normalized FRAP curve over 30 min for CF640 labeled $Na_v1.6$ nanoclusters. On average, there was a 23% ± 9% (n= 5; mean ± SD) recovery. **C)** Enlargement of the white box in (**A**) showing fluorescence before photobleaching, immediately after photobleaching, and 15 and 30 min postbleach. The dotted circle denotes the ROI bleached. Somatic nanoclusters localized outside of the bleached region show stable localization throughout the image sequence (yellow arrows).

$Na_v1.6$ nanoclusters. They could be composed of stably bound channels that persist in the same location, or of a pool of channels that are continually binding and unbinding. To investigate both the stability and protein turnover of the $Na_v1.6$ channels localized to nanoclusters, we used time-lapse imaging and fluorescence recovery after photobleaching (FRAP). By photobleaching a small number of nanoclusters, we could both observe the recovery of the bleached nanoclusters to obtain a measure of protein turnover, as well as follow the location and fluorescence intensity of nanoclusters located outside of the photobleach region. Fig. 4.3A shows a neuron transfected with $Na_v1.6$-BAD and ankyrinG-GFP (ankG-GFP), which is used to mark the axon. Surface

channels were labeled with the streptavidin-conjugated fluorophore CF640. This dye was used instead of the SA594 used in Fig. 4.1 since the longer wavelength laser (640nm) is less damaging to living cells than shorter wavelengths and thus is better suited to experiments with long acquisition times.

Fig. 4.3B shows the average fluorescence recovery of $Na_v1.6$ nanoclusters after photobleaching (5 nanoclusters from 3 cells). On average, the clusters recover 23% ± 9% (mean ± SD). Fig. 4.3C is an enlargement of the white box in Fig. 4.3A, and shows a representative FRAP experiment. Again, the contrast has been enhanced, revealing the presence of several large puncta, or somatic nanoclusters (arrows). High intensity 640 nm-laser was applied to a region of interest (white dashed circle) until the area was photobleached. In the example shown, three nanoclusters within the ROI were photobleached (Fig. 4.3C, second panel). The cell was then imaged for 30 min, with images acquired at a low frequency (every 5 sec) to minimize photobleaching during recovery. As quantitated in Fig. 4.3B, very little recovery was seen for the bleached nanoclusters over this time frame. At 15 min (Fig. 4.3C, third panel), two small spots are seen within the photobleached region. Due to the low intensity of these puncta in relation to the nanoclusters, they most likely represent individual $Na_v1.6$ channels that have diffused into this region. One molecule is still present 30 min after photobleach (Fig. 4.3C, last panel, yellow arrow), suggesting it has become stably bound within the region occupied by the nanocluster. The lack of fluorescence recovery for these domains suggest that the majority of channels localized to nanoclusters are stably bound and there is minimal exchange between bound and unbound channels during the times studied. In support of this idea, several of the bright puncta localized outside of the photobleach region persisted throughout the image sequence (Fig. 4.3C, yellow arrows). Thus, the lack of recovery of fluorescence within the bleached area demonstrates

that $Na_v1.6$ somatic nanoclusters are stable and have low channel turnover within the time frame of 30 min. This assay does not account for the possibility of new channel delivery to the plasma membrane.

High-density single-molecule tracking of $Na_v1.6$

The plasma membrane is a fluid structure with high levels of lipid and protein diffusion. Many forces influence protein diffusion including macromolecular crowding, cytoskeletal compartmentalization, and protein-protein interactions. The presence of stable domains within the plasma membrane that persist for minutes to hours is quite striking since membrane proteins generally display more transient immobilizations. Protein immobilization on this time scale is most likely due to stable interactions with binding partners. Analysis of $Na_v1.6$ diffusion can provide insights into protein interactions and thus insight into channel function and regulation. In the case of somatic $Na_v1.6$, we have a population of channels that appear to be stably anchored within nanoclusters and another population of mobile channels (Fig. 4.2B). Interestingly, visual inspection of the single-molecule behavior shows that mobile channels occasionally move in and around the large somatic clusters in a manner suggesting that there may be a property of these membrane regions containing $Na_v1.6$ nanoclusters that favor $Na_v1.6$ localization within these domains (data not shown). As such, we wanted to investigate the forces influencing the distribution of channels, as well as determining the strength of single-molecule interactions involved in $Na_v1.6$ localization to these nanoclusters. A particularly powerful technique combining spt-PALM with Bayesian statistical analysis was recently developed that uses high-density, single-molecule tracks to determine information about diffusion and potential energy landscape of the cell surface (Masson et al., 2014).

spt-PALM allows for sampling of a continually changing subset of molecules within a larger population such that the location and diffusion of thousands to tens of thousands of molecules can be obtained within a small region. Here we imaged rHNs transfected with a $Na_v1.6$ construct tagged with Dendra2 on the c-terminus ($Na_v1.6$-Dendra2). The experimental details are outline in Fig. 4.1. The use of a photoconvertible fluorophore and sparse activation allowed visualization of spatially separated molecules that could then be fit to a point spread function, providing information about $Na_v1.6$ membrane dynamics at a resolution below that of the diffraction limit.

Fig. 4.4A shows a DIV10 rHN expressing $Na_v1.6$-Dendra2 in the pre-photoconverted state. Fig. 4.4B shows the tracks obtained from spt-PALM where each colored line represents a track from an individual photoconverted Dendra2 molecule. Together, these tracks demonstrate the localization and diffusion of the $Na_v1.6$ population on the neuronal surface over the time sampled (~8 min for each image sequence). The data were then analyzed using the program InferenceMAP. The channel translocations were first divided into regions using an adaptive meshwork such that each region contained approximately the same number of tracks with a minimum side length larger than the average step size of the molecules (Fig. 4.4C, white lines). In this case, mesh sizes were generally ~130 x 130 nm^2. The large number of translocations within each grid of the mesh was used to obtain information on diffusion and potential energy (see Fig. 4.1.7). Fig. 4.4C shows the diffusion coefficient calculated for each section of the grid based off of the step sizes contained within each region, represented as different colors. Warmer colors represent regions of higher diffusion and cooler colors represent lower diffusion. The arrows for each grid section show the direction of the force for each region.

The potential energy of each mesh domain was also calculated using InferenceMAP. Fig. 4.4D shows this visualized as a 3D diffusion landscape such that regions with high energy are represented as warm-colored peaks and regions with low energy are visualized as cool-colored troughs. Here we see potential energies ranging around 0-6 K_BT. Fig. 4.4E shows an enlargement of the white box in Fig. 4.4B and the black box in Fig. 4.4D. As seen in Fig. 4.4B, this region contains a large number of highly localized tracks and most likely represents the location of a $Na_v1.6$ nanocluster as visualized through spt-PALM. The energy landscape shows low energy in this same location (represented by the blue region within the black box in Fig. 4.4D). Fig. 4.4E shows this region of low energy from the side. It is visualized as an energy well such that proteins tend to move into and remain within this membrane region. The depth of the energy well is around ~5.4 K_BT, which is indicative of stable anchoring of proteins (Masson et al., 2014). Thus, analysis of the potential energy landscape is consistent with the localization of $Na_v1.6$ to somatic nanoclusters through interactions with an anchoring protein.

Diffusion of $Na_v1.6$-Dendra2 decreases over neuronal maturation

While imaging $Na_v1.6$ in neurons of different ages with surface labels as in Fig. 4.2, it was noted that the proportion of channels in the mobile versus non-mobile populations tends to shift during neuronal maturation. Immature neurons (DIV7) appeared to have a greater percentage of channels present in the mobile population for younger neurons, while more mature neurons (DIV15) seemed to have more stable somatic nanoclusters. In order to investigate this quantitatively, we repeated the spt-PALM experiment for DIV7, DIV10, and DIV15. As a control, we also performed spt-PALM on CD4-Dendra2. CD4 is a small, single-pass transmembrane protein normally expressed in T-cells. Since it is not endogenously expressed in

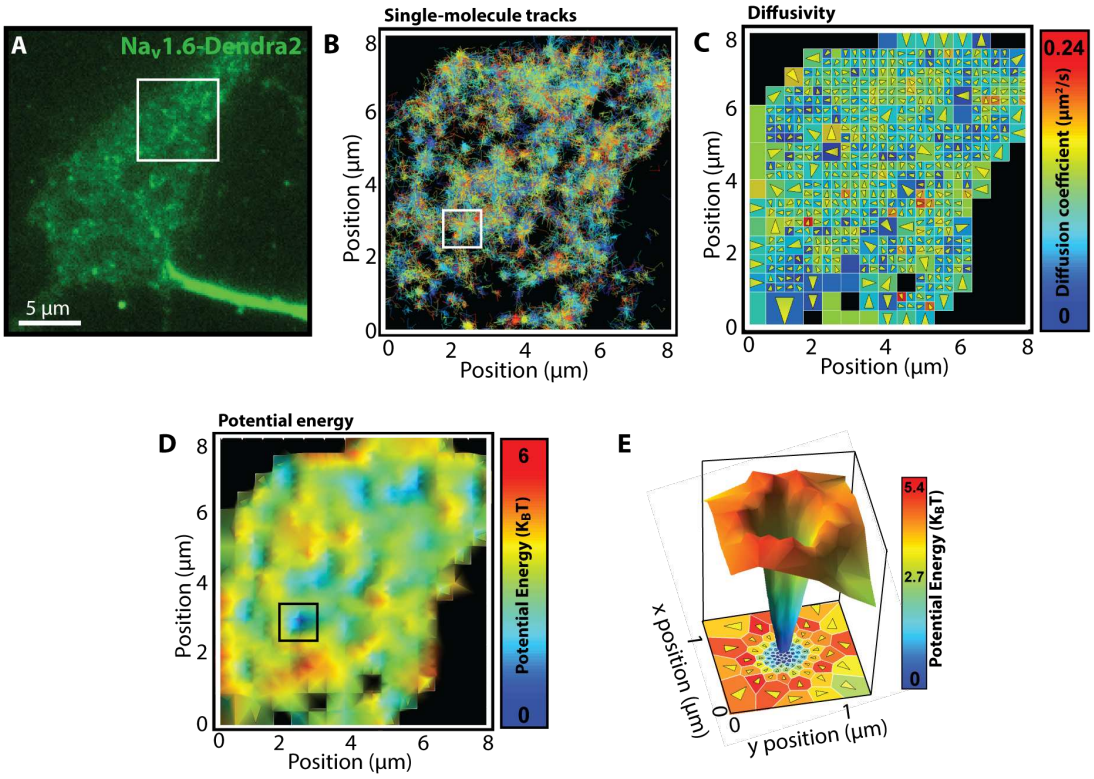

Figure 4.4. Single particle tracking-PALM of Na$_v$1.6-Dendra2 shows heterogeneity in the diffusion and energy landscapes.

DIV 10 hippocampal neurons expressing Na$_v$1.6-Dendra2 were imaged in TIRF. Dendra2 particles were stochastically activated to allow visualization of individual particles. Image sequences of 10,000 frames were acquired at 20Hz. **A)** Image of neuron expressing Na$_v$1.6-Dendra2 showing unconverted Dendra2. **B)** Ensemble of tracks from individual Na$_v$1.6-Dendra2 particles from an ROI located in the somatic region (white box in **A**). Molecules were detected and connected into tracks using uTrack. Each line represents a track from an individual particle. The axes represent the X and Y positions of the particles in µm. **C)** The tracks from **(B)** were divided into regions based on adaptive meshing such that each section contains similar numbers of localizations. The step sizes of particle tracks within these regions were used to determine the diffusion coefficient within each grid. Warmer colors represent regions with high diffusion coefficients. The arrows within each grid represent the average direction of movement, or force, within each region. **D)** A 3D representation of the potential energy landscape. Information about both the mobility of channels and the direction of movement are used to determine the potential energy. The potential energy for each region is represented by a color such that warm colored peaks represent membrane regions with high energy. **E)** Enlargement of a single energy well. The white box in **(B)** shows a high density of tracks which corresponds with the energy well within the black box in **(D)**. The depth of the energy well is approximately 5.4 K_BT.

neurons and has very little intracellular mass, it should have few binding or interacting partners. Due to its small size it should move relatively freely throughout the neuronal surface.

The tracks from each of these conditions were analyzed using InferenceMAP. The diffusion landscapes representing the diffusion coefficients (as shown in Fig. 4.4C) are shown here as 3D landscapes. $Na_v1.6$-Dendra2 channels expressed in DIV7 neurons show fairly high diffusion coefficients, as indicated by the warm colors (Fig. 4.5A) and $Na_v1.6$-Dendra2 channels in DIV10 have lower diffusion coefficients as indicated by the cooler colors in the landscape (Fig. 4.5B). This is also true for $Na_v1.6$-Dendra2 in DIV15 neurons (Fig. 4.5C). CD4 (Fig. 4.5D), which should represent a nearly freely diffusion protein, shows high diffusion coefficients represented by a large portion of the diffusion landscape covered with warm colors. Unexpectedly, there were also regions of the landscape that showed slow diffusion. Since we do not expect CD4 to stably bind to any proteins and should have fairly minimal protein-protein interactions in a neuron, these regions most likely represent areas of either high molecular crowding or containing a complex cortical cytoskeleton.

In order to quantitate these maps, the diffusion coefficients from the landscapes were plotted as histograms. The diffusion coefficient from each mesh domain (as shown in Fig. 4.4C) was multiplied by the number of localizations in that domain used to calculate the average diffusion coefficient in that region. Fig. 4.5E shows the distribution of diffusion coefficients. The diffusion coefficients of $Na_v1.6$ expressed in DIV7 rHNs are higher and more broadly distributed that that seen for the DIV10 or DIV 15 neurons. This is consistent with fewer immobilized channels in younger neurons. Relative to DIV10 neurons, $Na_v1.6$-Dendra2 shows even less mobility, consistent with the development of $Na_v1.6$ somatic nanoclusters during neuronal maturation.

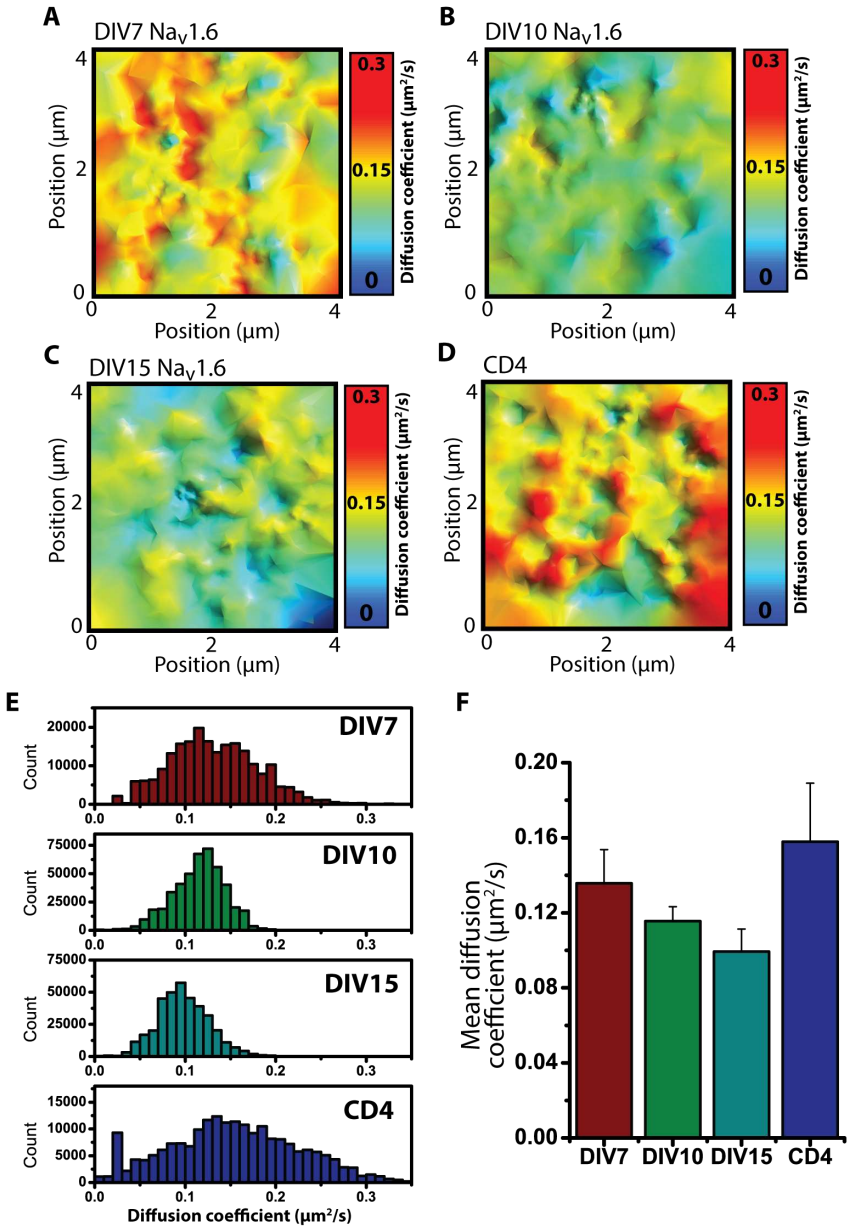

Figure 4.5. $Na_v1.6$-Dendra2 in mature neurons shows decreased diffusion.

Neurons expressing either $Na_v1.6$-Dendra2 or CD4-Dendra2 were imaged using spt-PALM and analysis performed using InferenceMAP as described in Fig. 4.1. **A-D)** 3-dimentional diffusion landscapes were created using InferenceMAP for $Na_v1.6$-Dendra2 in DIV 7 **(A)**, DIV10 **(B)**, and DIV15 **(C)** neurons or CD4-Dendra2 in DIV7 neurons **(D)** as a control. **E)** Diffusion coefficients taken from each grid of the meshwork used to make the 3D landscapes were plotted as a histogram. The distribution of diffusion coefficients of $Na_v1.6$-Dendra2 is the broadest for immature neurons (DIV7) and the distribution becomes narrower with a lower diffusion coefficients as neurons mature (DIV10 and 15). CD4-Dendra2 (bottom panel) is a small protein that should represent nearly free diffusion and shows a broad distribution of diffusion coefficients. **(F)** Mean ± SD of the distributions shown in **(E)**. Data is pooled from analysis of multiple cells: 6 cells for DIV7, 3 cells for DIV10, 3 cells for DIV15, or 4 cells for CD4.

When we then compared these to the CD4 control representing a nearly freely moving protein. The distribution of diffusion coefficients for CD4 is broad, demonstrating protein diffusion ranging from nearly immobile to highly mobile. The distribution between cells was highly heterogeneous, suggesting that the lipid and protein environment is variable between neurons. The distribution is even broader than that of $Na_v1.6$-Dendra2 in DIV7 rHNs. The mean of each distribution is plotted in Fig. 4.5F. This shows that that average diffusion coefficient of $Na_v1.6$-Dendra2 decreases during neuronal maturation. The diffusion coefficient is the greatest for CD4, consistent with its small size. Overall, we see that $Na_v1.6$-Dendra2 channels have a lower mobility in more mature neurons, consistent with the development of $Na_v1.6$ nanoclusters during this timeframe.

$Na_v1.6$ somatic nanoclusters are ankyrinG independent

The energy wells that represent $Na_v1.6$ nanoclusters (as in Fig. 4.4E) are most likely indicative of stable $Na_v1.6$ channel interactions with a binding partner present intracellularly. The only known mechanism of Na_v localization in neurons is its interactions with ankG. Loss of ankG-binding prevents localization of Na_v channels to the AIS. To investigate the role of ankG-binding in the somatic localization of $Na_v1.6$, we examined the somatic distribution of a $Na_v1.6$ mutant channel in which the ankyrin-binding motif (ABM) was removed ($Na_v1.6$-BAD-dABM). Fig. 4.6A shows a DIV10 rHN expressing $Na_v1.6$-BAD-dABM and ankG-GFP to mark the axon. In contrast to the full-length channel that co-localizes with ankG at the AIS (see Fig. 4.3A), the mutant channel does not show a strong accumulation within this region. Surprisingly, $Na_v1.6$-BAD-dABM still localized to the somatic nanoclusters (Fig. 4.6A). To look at the mobility of these nanoclusters, and the individual channels, we again overlaid two frames from an image sequence of channels labeled with SA-594 on the somatic membrane (Fig. 4.6B). When the first

frame (top panel, pseudocolored magenta) and a frame 10 sec later (middle panel, pseudocolored green) were overlaid we again saw large puncta that are stable over this time, while some of the smaller puncta no longer co-localize. This represents the presence of both a mobile and immobile population of channels, similar to that seen for the full-length $Na_v1.6$ protein (Fig. 4.2B).

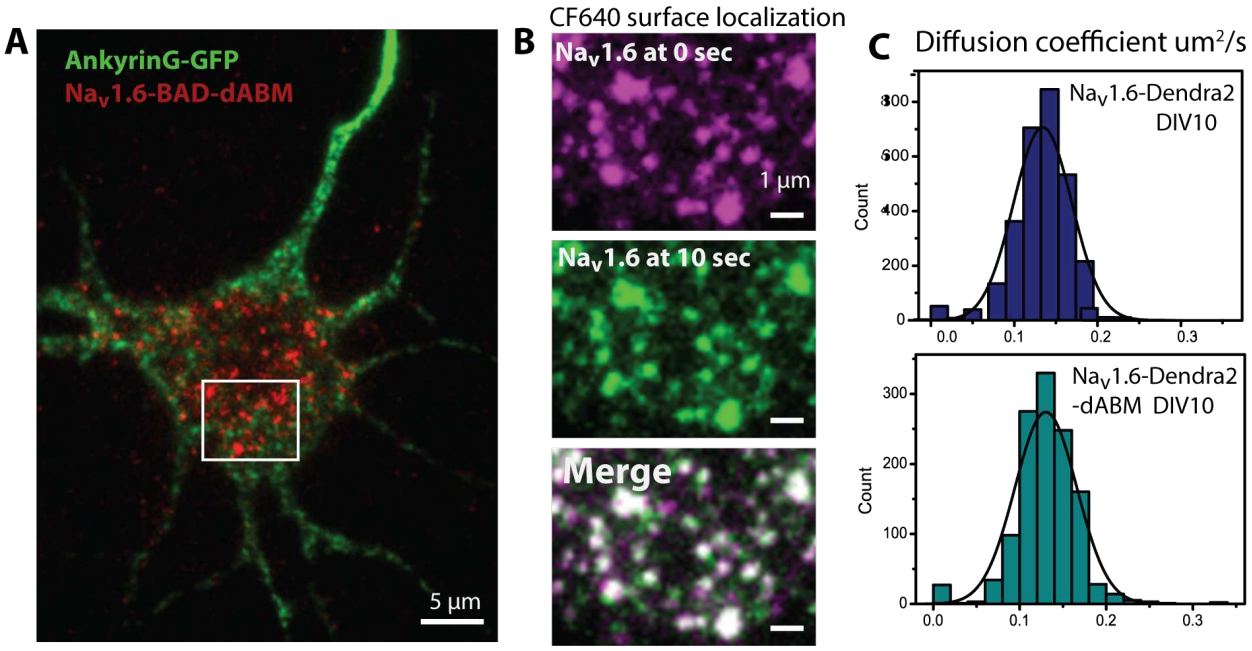

Fig 4.6 $Na_v1.6$ somatic distribution is ankyrinG independent.

A) DIV10 rHN expressing the mutant $Na_v1.6$ channel lacking the ankyrin-binding motif. ($Na_v1.6$-BAD-dABM). This channel localizes to the somatic region of the channel, but does not show a high density of channels within the AIS, which is marked by ankG-GFP. **B)** Enlargement of white box in **(A)**. Panels represent two frames of an image sequence spaced 10 sec apart. The first frame (magenta) and a frame 10 sec later (green) are overlaid (merge, bottom panel). Co-localization appears white. Large, bright puncta appear in the same location in both image sequences while smaller puncta demonstrate mobility. **C)** Histograms of the diffusion coefficients from spt-PALM data (See Fig. 4.5) for the full-length $Na_v1.6$ channel and the mutant dABM channel. The distribution of these channels is similar, suggesting similar mobility of these channels within the somatic region.

To determine if the overall diffusion of the somatic channels was influenced by the ability to bind ankG, we performed spt-PALM on $Na_v1.6$-Dendra2-dABM in DIV10 rHNs. As described above, low levels of photoconverted Dendra2 were imaged for 10,000 frames through

repeated activation and photobleaching of individual Dendra2 molecules. These were tracked using uTrack and the resulting translocations were analyzed using InferenceMAP to create diffusion and potential energy landscapes. The distribution of the diffusion coefficients for the mutant channel was again plotted in a histogram (Fig. 4.6C). The distribution of the full-length $Na_v1.6$-Dendra2 channel from Fig. 4.5E is plotted here for comparison. The range and distribution of the diffusion coefficients for the full-length and dABM mutant were nearly identical, demonstrating that ankyrin binding does not influence the diffusion of $Na_v1.6$ in the soma of rHNs. Together these data suggest an ankG-independent localization mechanism for $Na_v1.6$ distribution in the soma.

$Na_v1.6$ nanoclusters are actin independent

Since the localization mechanism of somatic $Na_v1.6$ l is not due to ankyrin-binding, we hypothesized that other cytoskeletal components may be involved. Indeed, actin is involved in the localization of $K_v2.1$ to large, micron size clusters on the soma of some neurons (O'Connell et al., 2006) as well as influencing the diffusion of a number of membrane proteins. Thus we wanted to determine whether $Na_v1.6$ nanoclusters are also stabilized by cortical actin. Actin is present throughout nearly the entire neuron, while $Na_v1.6$ nanoclusters represent very small regions of the neuronal membrane. Thus, in order to see whether there is any distinct actin organization present around the $Na_v1.6$ nanoclusters we needed to use super-resolution microscopy such that actin structures could be resolved below the diffraction limit. For this, we used photoactivation localization microscopy (PALM) of photoactivatable-GPF actin (paGFP-actin). Neurons were co-transfected with $Na_v1.6$-BAD and paGFP-actin and the $Na_v1.6$ surface distribution was visualized with CF640. 405-nm laser was used to activate low numbers of the paGFP-actin molecules, and 488-nm laser was used to visualize and photobleach activated

particles. The sparse number of activated fluorophores were fit with a Gaussian distribution to localize particles below the diffraction limit. The localizations from each frame were reconstructed into a super-resolution image of actin for a DIV11 rHN (Fig. 4.7A).

The image acquired using light microscopy is displayed on the left side of the image,

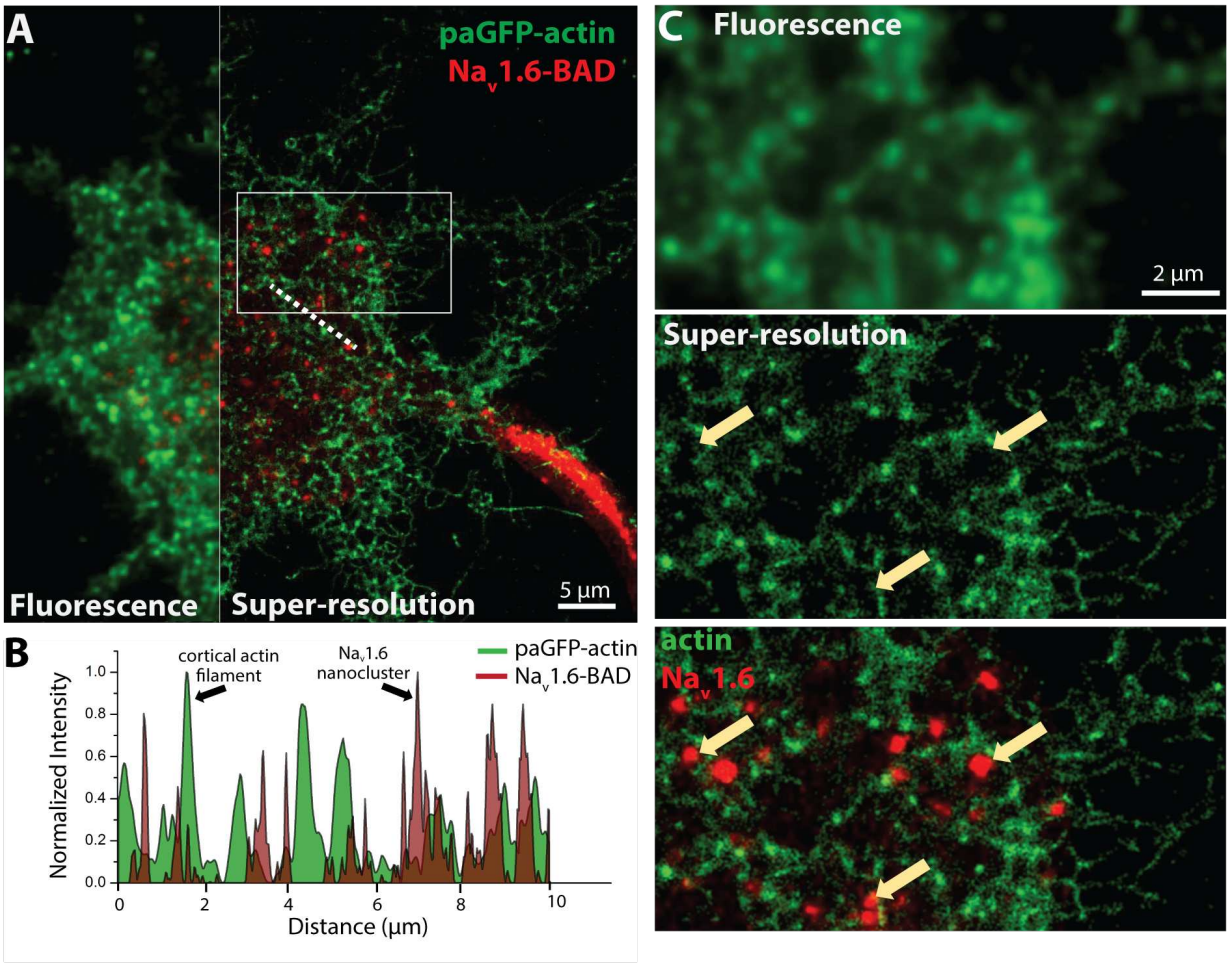

Figure 4.7 Na$_v$1.6 nanoclusters are not associated with cortical actin.

A) DIV10 rHN transfected with photoactivatable-GFP-actin (paGFP-actin) and Na$_v$1.6-BAD. Surface distribution of Na$_v$1.6 visualized with CF640R. PALM-based super-resolution image of paGFP-actin (right side) was reconstructed from cycles of activation and photobleaching of individual paGFP-tagged actin molecules. The super-resolution image reveals fine actin structures not visible with light microscopy (left side). The single process with dense CF640 surface labeling is the AIS. **B)** Line scan showing the normalized fluorescence intensity of actin (green) or Na$_v$1.6 (dark red) of the dotted white line in **(A)**. Na$_v$1.6 nanoclusters are generally adjacent to, but not co-localized with cortical actin filaments. **C)** Enlargement of box in **(A)** showing the diffraction limited image (top panel) of the PALM reconstruction (middle panel). Na$_v$1.6-BAD visualized with CF640 is present near, but not co-localized with actin structures present in the TIRF field (bottom panel).

with the super-resolution image on the right. Fig. 4.7C shows an enlargement of the white box in Fig 4.7A to demonstrate the relative distribution of $Na_v1.6$ and actin. Again, the image obtained by light microscopy shows little fine structure (top panel), while PALM-based super-resolution clarifies the location of the actin (middle panel). Somatic $Na_v1.6$ channels appear to localize to membrane regions distinct, but often adjacent to cortical actin structures present in the TIRF field (bottom panel, yellow arrows). This is demonstrated by the line scan in Fig. 4.7B. The fluorescence intensity of actin and surface-labeled $Na_v1.6$-BAD along the dotted line in Fig. 4.7A were normalized and plotted as a function of distance. The actin peaks corresponding to cortical actin filaments and the $Na_v1.6$ peaks corresponding to somatic nanoclusters do no co-localize, but are often in close proximity.

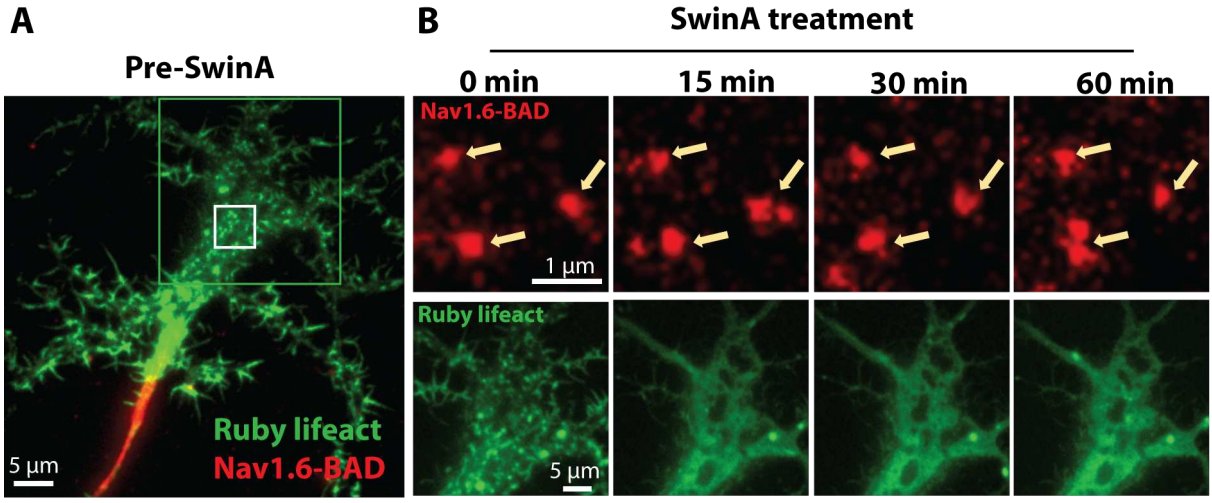

Figure 4.8 Actin depolymerization does not dissolve $Na_v1.6$ nanoclusters.

A) A neuron expressing $Na_v1.6$-BAD and ruby-lifeact was imaged in TIRF. $Na_v1.6$-BAD was labeled with CF640 to visualize the surface distribution. **B)** (Top) Enlargement of white box in **(A)** containing three $Na_v1.6$ nanoclusters. Neurons were imaged for 10 min to establish a baseline, then 200nM swinholideA (swinA) was added to the bath to depolymerize actin. Images were acquired once every 1 min. The fluorescence intensity and location of the nanoclusters remained constant up to 1 hour after actin depolymerization (top panels, yellow arrows). (Bottom) Enlargement of the green box in **(A)**. Ruby-lifeact labeled actin filaments were used to demonstrate the effectiveness of swinA treatment. Before swinA treatment, distinct filamentous actin structures were visible. After addition of the drug, ruby-lifeact showed a more homogeneous distribution (right bottom panels), demonstrating the depolymerization of actin.

To better understand whether actin is involved in $Na_v1.6$ localization to nanoclusters, we imaged the distribution of $Na_v1.6$-BAD in the presence of 200nM swinholideA (swinA), a drug that induces f-actin depolymerization. Fig. 4.8A shows a neuron expressing $Na_v1.6$-BAD and ruby-lifeact. The neuron was imaged in TIRF with a slow frame rate (every 1 min) to minimize photobleaching, and swinA was added after 10 min of imaging to establish a baseline. Fig. 4.8B, top panels, is an enlargement of the white box in Fig. 4.8A, showing 3 nanoclusters that were present before the addition of swinA. The intensity and location of the clusters remains remarkably consistent even 60 min after the addition of swinA (Fig. 4.8B, top panels, yellow arrows), suggesting that disruption of actin does not affect the stability of the nanoclusters. Ruby-lifeact, a fluorescent actin-binding protein, was used to confirm swinA-induced f-actin depolymerization. The ruby-lifeact showed distinct actin filaments before the addition of swinA (Fig. 4.8A), which dissolved within a few minutes of swinA treatment (Fig 4.8B, bottom right panels). The distribution of $Na_v1.6$ within the AIS was also stable during the course of the experiment (data not shown).

Co-localization studies

Since neither ankyrinG nor actin seem to play an important role in the maintenance of the structure or formation of the somatic nanoclusters, we decided to investigate colocalization of these nanodomains with several different proteins, hoping that some of them might indicate the purpose of these structures. We first imaged clathrin-light-chain tagged with GFP (CLC-GFP) to determine whether the $Na_v1.6$ nanoclusters were formed via channel localization to endocytic sites (Fig. 4.9A). However, few of the $Na_v1.6$-BAD channels labeled with CF640 co-localized with CLC-GFP. This result suggests that the nanoclusters are not endocytic platforms. This is consistent with the long lifetime seen for the nanoclusters since clathrin-coated pits tend to be

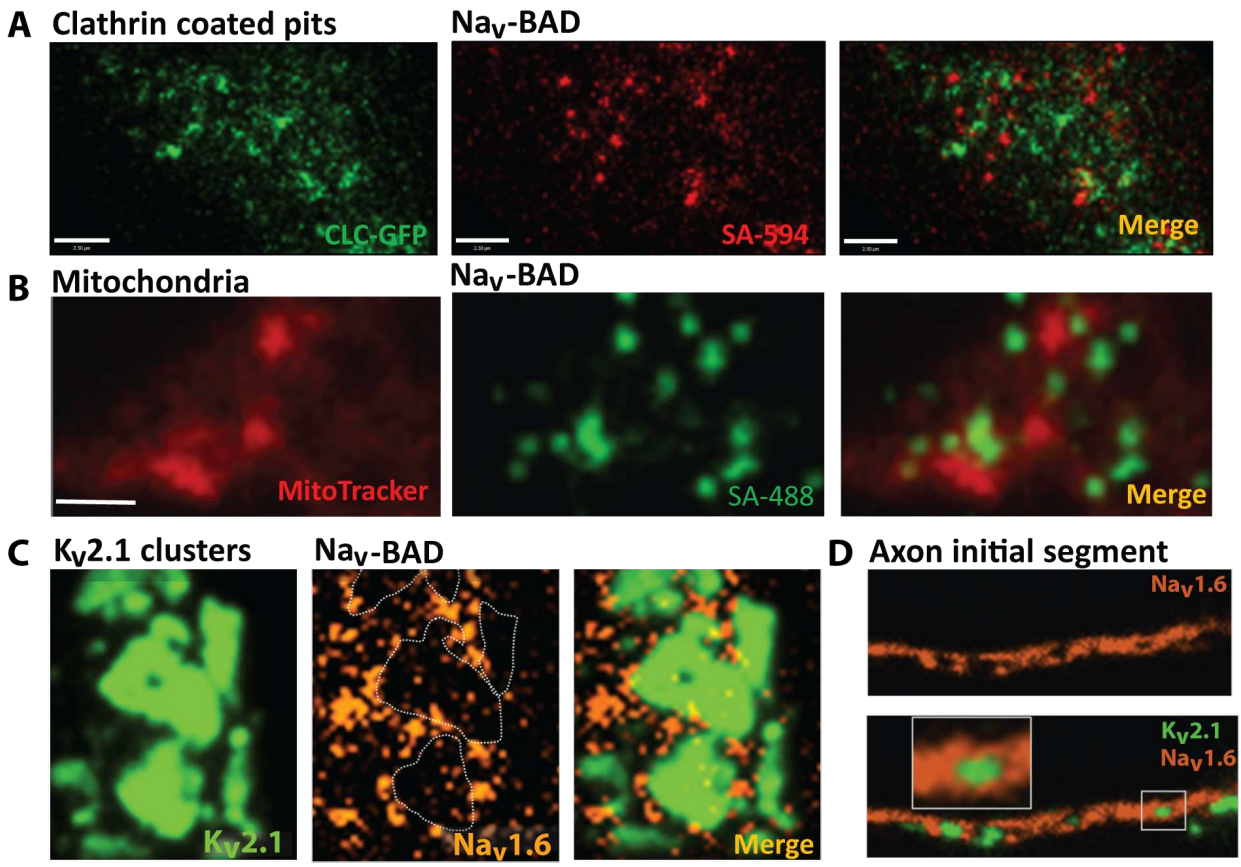

Figure 4.9. $Na_v1.6$ clusters do not co-localize with endocytic sites, mitochondria or ER-PM junctions.

(A-C) Correspond to TIRF images of hippocampal neurons. **A)** Neurons transfected with GFP-clathrin-light-chain (left green panel) and $Na_v1.6$-BAD labeled with SA-594 (red middle panel) show no significant co-localization (yellow) as observed on the merge panel (right). **B)** Mitochondria were labeled with MitoTracker (left panel, red), live neurons transfected with $Na_v1.6$-BAD surface labeled in this case with SA-488 (middle panel, green). No apparent co-localization was observed. **C)** Neurons co-transfected with GFP-$K_v2.1$, a marker of ER-PM junctions, (green) and $Na_v1.6$-BAD surface labeled with SA-594 (orange). The first three panels correspond to a somatic region of a neuron. The merged image of the two channels (left panel) shows how GFP-$K_v2.1$ (green) and $Na_v1.6$-BAD-SA594 (orange) localize to mutually exclusive regions, with $Na_v1.6$ clusters located outside of the $K_v2.1$ clusters, and only few single channels located inside. **D)** Panels corresponding to the axon initial segment of the same neuron from **(C)** where the same pattern can be observed. Upper panel corresponds to surface labeled SA-594 $Na_v1.6$ channel (orange). Bottom panel corresponds to a merged image of the previous channel with GFP-$K_v2.1$ (green). An enlargement of one of the axonal $K_v2.1$ clusters surrounded by $Na_v1.6$ channels is shown (white box).

more transient (seconds to minutes) (Loerke et al., 2009; Weigel et al., 2013). This does not exclude, however, that small numbers of $Na_v1.6$ channels could interact with clathrin since all proteins have a basal rate of protein turnover.

Mitochondria have been observed to localize near membrane-bound proteins and regulate them through calcium and oxidative signaling (Chaplin et al., 2015). We investigated whether mitochondria are consistently found under or near the somatic nanoclusters. MitoTracker was used to mark mitochondria in live neurons and SA-488 was used to label $Na_v1.6$-BAD. Mitochondria close to the plasma membrane were imaged in TIRF and compared to the distribution of $Na_v1.6$. No apparent relationship between mitochondria and the somatic nanoclusters was observed (Fig. 4.9B).

We next looked at the distribution of $Na_v1.6$ in relation to the delayed rectifier K_v channel, $K_v2.1$, which forms large micron-sized clusters on the soma and AIS of some neurons (Tamkun et al., 2007; Sarmiere et al., 2008). These channels were recently found to mediate the formation of junctions between the endoplasmic reticulum and plasma membrane (ER-PM junctions) (Fox et al., 2015), thus creating membrane regions of specific, functional importance. We co-expressed $Na_v1.6$-BAD and GFP-$K_v2.1$, labeling surface $Na_v1.6$ with SA-594. $Na_v1.6$ nanoclusters were found around, but not within, large $K_v2.1$ clusters, as seen in Fig.4.9C. This is similar to the distribution seen in the AIS where these ion channels also clearly localize to mutually exclusive regions of the membrane (Fig. 4.9D), consistent with a recent study (King et al., 2014). In contrast to the differential $Na_v1.6$ expression patterns and localization mechanisms seen in the AIS and soma, the exclusion from $K_v2.1$-induced ER-PM junctions appears to be consistent in both neuronal subcompartments.

4.4 Discussion

Due to the low numbers of somatic $Na_v1.6$ channels and lack of tools to visualize them, the distribution of these proteins has not been previously visualized in living cells. Here, with the use of $Na_v1.6$ constructs allowing the specific labeling of $Na_v1.6$ surface channels, combined with the sensitivity of TIRF microscopy, we were able to visualize the subcomparmental distribution of somatic $Na_v1.6$ channels in live cells for the first time. Functional studies suggested a non-uniform distribution of somatic channels based on cell-attached patch clamp (Williams and Stuart, 2000), which is consistent with the heterogeneous distribution of channels seen within this region. Specifically, we demonstrated a novel localization pattern of $Na_v1.6$ in cultured hippocampal neurons to stable nanoclusters. Importantly, Na_v channel localization to these membrane domains is ankyrin independent, which is a striking discovery since this is the only known ankyrin-independent mechanism for Na_v channel localization.

The detection of $Na_v1.6$ channel localization with single-molecule sensitivity in living cells enabled analysis of channel mobility. This is important since both protein location and diffusion provide insight into protein regulation. Protein immobilization within the plasma membrane often indicates protein-protein interactions. Here, we see that $Na_v1.6$ localizes to membrane regions for extended periods of time (minutes to hours), suggesting a very stable interaction. Using spt-PALM data we were able to describe the diffusion and potential energy landscapes surrounding these static structures. The power in this approach lies in its ability to investigate the entire population of $Na_v1.6$ surface protein within a short (<10 min) time frame and with single-molecule resolution. Thus, we were able to see both global distribution, and obtain information on individual channel behavior. This allows analysis of the heterogeneity of protein behavior that is lost in techniques like FRAP that provide only an average of protein

behavior. These experiments showed that regions of the membrane where $Na_v1.6$ nanoclusters are found can be modeled as energy wells for $Na_v1.6$ channels.

Although it is very clear that ankyrin-binding is necessary and sufficient for AIS targeting of Na_v channels (Gasser et al., 2012), the finer details are perplexing. Although ankG is present throughout the AIS and all the $Na_v1.x$ isoforms contain nearly identical ankyrin-binding motifs, $Na_v1.2$ and $Na_v1.6$ localize to the proximal and distal regions, respectively (Kaplan et al., 2001). Thus, additional localization mechanisms must exist. Furthermore, the Rasband lab recently demonstrated that in the absence of ankG another member of the same family, ankyrinR, can also target Na_v channels to node of Ranvier (Ho et al., 2014). Together, these demonstrate complex interactions between ankyrin and Na_v channel molecules. It is possible that the localization mechanism in the soma is not truly ankyrin independent, but is interacting through a region other than the identified ankyrin-binding motif that was investigated in this study.

Information regarding channel trafficking and specifics of channel localization has remained elusive. We demonstrated that $Na_v1.6$ channels localize to the AIS via direct trafficking in chapter 3 and (Akin et al., 2014), in contrast to the previously accepted theory of diffusion trapping where channels passively diffuse into the AIS and are subsequently bound to ankyrin. Further experiments need to be performed in order to decipher the specific traffic pathway that somatic $Na_v1.6$ channels follow versus that taken by axonal $Na_v1.6$ channels. The signal for these different trafficking pathways could be post-translational modifications of the channels, or specific protein interactions. In a recent paper it was shown that $Na_v1.2$ must bind ankyrin for kinesin-dependent transport to the AIS (Barry et al., 2014). This suggests that Na_v channel-ankG structures are inserted into the AIS membrane as a preformed complex. The stability we see with the somatic $Na_v1.6$ nanoclusters is most likely due to interactions with a not yet identified

scaffolding protein, and thus compartment specific trafficking could be regulated by which scaffolding protein $Na_v1.6$ is bound to. Recently a new multidomain scaffolding protein (Kidins220/ARMS) that interacts and modulates $Na_v1.2$ activity has been described (Cesca et al., 2015) and could be a candidate with respect to somatic nanocluster formation.

We propose that the stable $Na_v1.6$ nanoclusters described in this study are most likely sites of localized regulation of $Na_v1.6$. Studies have demonstrated that somatic and AIS Na_v channels have differing functional properties. However, the specifics of such regulation remain unknown. The nanoclusters are not sites of endocytosis since they are both very stable and do not co-localize with clathrin. It is most likely that these sites also localize other ion channels such as calcium channels or sodium-activated potassium channels. Thus the activity of these channels would modulate each other. These domains could also concentrate signaling molecules proteins such as protein kinases and phosphatases that modify channel behavior.

Despite the fact that Na_v channels were discovered decades ago and their central importance to neuronal function has been long accepted, knowledge of $Na_v1.6$ cell biology is surprisingly lacking. This study provides insight into the cell biology of $Na_v1.6$ and opens up new areas of research such as how localized regulation of these channels may influence overall neuronal function in additional to furthering our understanding of basic neuronal cell biology.

Chapter 5

Summary and Future Directions

5.1 $Na_v1.6$ trafficking and localization

This dissertation describes some of the first experiments investigating $Na_v1.6$ cell biology in living cells with high spatial and temporal resolution. While the polarized distribution of Na_v channels in neurons has been known since the 1980s (Catterall, 1981), the trafficking mechanisms underlying this essential localization and the subsequent cell surface dynamics have remained inaccessible. The ability to perform such studies hinged on the successful creation of a construct containing an extracellular tag, which, due to difficulties in working with Na_v cDNA's and the propensity for channel modifications to alter channel trafficking or function, had been lacking in the field. The successful creation modified $Na_v1.6$ constructs as described in chapter 2 represents a powerful tool for investigating Na_v cell biology.

5.2 Direct trafficking to the AIS

The experiments outlined in chapter 3 provide evidence for direct trafficking of $Na_v1.6$ to the AIS. These studies represent the first live-cell trafficking studies of a full-length Na_v channel with single molecule sensitivity. Using fluorescent probes to visualize the delivery of proteins to the neuronal surface, I demonstrated that $Na_v1.6$ is directly delivered to the AIS, presumably through vesicular trafficking. Removal of the ankyrin-binding motif disrupts axonal delivery without disrupting unpolarized transport to the plasma membrane, while addition of ankyrin-binding properties to a chimeric protein such as $K_v2.1$ does not confer directed axonal delivery. Trafficking of $Na_v1.6$ to the cell surface is enhanced by interactions with the microtubule

associated protein Map1b, which interacts with the N-terminus of the channel (O'Brien et al., 2012). This is consistent with the idea of a microtubule-based transport mechanism for $Na_v1.6$. In collaboration with the Meisler lab, we are performing trafficking studies to determine whether the enhanced Map1b surface expression in neurons is specific for axonal localization, or whether it affects overall trafficking.

The conclusion of directed vesicular trafficking contradicts the current dogma in the field. A recent review article stated that "there is no direct targeting [of Na_v channels] to the axon, but rather unpolarized export to the plasma membrane followed by selective endocytosis from the somatodendritic compartment" (Leterrier and Dargent, 2014). This statement was based on trafficking studies of chimeric proteins containing the $Na_v1.2$ domain II-III intracellular loop such that it transferred ankyrin-binding properties to the reporter proteins (Garrido et al., 2003; Fache et al., 2004). These resourceful studies were vital in our understanding of Na_v localization in terms of ankyrin-based localization mechanisms (Garrido et al., 2003; Fache et al., 2004), restricted diffusion due to anyrinG binding (Brachet et al., 2010), and modulation of the channels by protein kinase CK2 (Bréchet et al., 2008). However, the interpretation of studies using chimeric proteins must be taken under consideration since they do not always fully recapitulate the behavior of the full-length protein. Indeed, some ankG-binding behavior of the full-length channel was shown to differ from that of chimeric proteins (Gasser et al., 2012).

Due to technical limitations, the trafficking experiments in this dissertation were performed in young, developing neurons (DIV6). As a result, the data from chapter 3 must be interpreted in the context of neuronal development and of $Na_v1.6$ channels immediately after biosynthesis. It is likely, however, that this conclusion will be consistent in more mature neurons. Direct trafficking and not diffusion trapping was observed before the establishment of the

diffusion barrier, which develops in DIV7-10 neurons (Nakada et al., 2003). Therefore, this mechanism is likely to be maintained in more mature neurons that have developed such a barrier. Future experiments will need to investigate channel trafficking in such mature neurons and, ultimately, in intact tissue. Additionally, it will have to be determined whether the other major AIS isoforms $Na_v1.1$ and $Na_v1.2$ also demonstrate direct trafficking. One study showed that $Na_v1.2$ localization to the AIS is kinesin-based, suggesting that the localization of this isoform might also depend on vesicular trafficking (Barry et al., 2014). If so, it will be interesting to determine whether different Na_v isoforms are packaged within the same vesicles or are delivered separately to the AIS. During development $Na_v1.2$ is the major isoform at the AIS and nodes of Ranvier and is later replaced by $Na_v1.6$ (Boiko et al., 2003). The signals and mechanisms responsible for this transition have still not been elucidated. The direct trafficking mechanism that I demonstrated for $Na_v1.6$ is logical in the context of this transition since diffusion trapping would not have precise spatial and temporal control.

The study by Barry et al. (2014) also raises an interesting idea about the formation of the intricate AIS membrane. The experiments demonstrated that $Na_v1.2$ forms a complex with ankG within vesicles before delivery to the AIS. This suggests that perhaps multiple components of the AIS are assembled within the somatic cytoplasm and are delivered as a pre-established unit. My studies demonstrate that very few (1-6) $Na_v1.6$ channels are simultaneously delivered to the AIS in what we assume to be vesicular delivery. This would be consistent with the delivery of a larger membrane complex rather than $Na_v1.6$ channels specifically. Vesicles containing $K_v2.1$ channels have been shown to contain around 30 channels per vesicle (Deutsch et al., 2012a). Trafficking studies with fluorescent protein tags on both $Na_v1.6$ and ankG should be performed to determine whether these proteins are delivered to the AIS simultaneously.

The motif identified as responsible for AIS localization, the ankyrin-binding motif, is conserved throughout all the $Na_v1.x$ isoforms. However, only a subset of Na_v isoforms are localized by interactions with ankG and, furthermore, isoforms distribute unevenly within the ankG occupied region of the AIS. For example, $Na_v1.2$ localizes to the proximal part of the axonal membrane while $Na_v1.6$ has a more distal distribution (Lorincz and Nusser, 2008; Boiko et al., 2003). Since ankG is distributed homogeneously throughout the AIS, there are most likely additional signals responsible for this complementary localization of the various Na_v isoforms. It could be dependent solely on delivery of the isoforms to the compartments, or there could be additional regulatory or accessory proteins that influence isoform localization. CK2 has been shown to strengthen Na_v-ankG binding and is a potential candidate (Brechet et al., 2008). This sort of differential distribution is on the order of microns. It is becoming more apparent that the AIS is even further subdivided into membrane domains at the submicron level. Clusters of $K_v2.1$ in the AIS (Sarmiere et al., 2008) are found in regions distinct from that of ankG or Na_v containing regions (King et al., 2014).

5.3 Somatic distribution of $Na_v1.6$

The majority of studies on Na_v channels have focused on the AIS population of channels. The experiments in chapter 4 demonstrate the first study of the live-cell somatic distribution and dynamics of a distinct Na_v isoform. I found that somatic $Na_v1.6$ channels have both a mobile and non-mobile distribution on the somatic surface, with the non-mobile channels localizing to discrete regions of the membrane, or nanoclusters. This localization is ankG independent since removal of the ankyrin-binding motif, while disrupting AIS localization, does not affect the localization pattern or diffusion of the somatic channels. To the best of our knowledge, this is the first ankyrin-independent localization of any Na_v isoform. We have, however, been unable to

determine the mechanisms that form and regulate these nanoclusters. Future studies will investigate potential candidates regulated this type of localization. The stability of $Na_v1.6$ channels within nanoclusters resembles that of channels in the AIS. For both populations of channels, FRAP experiments yield a recovery of less than 20% within 30 min. In comparison, ion channels with high mobility in the plasma membrane can show large (>60%) recovery in less than 2 min (O'Connell and Tamkun, 2005; Solé et al., 2009).

Functional studies have demonstrated that somatic and axonal channels have different biophysical properties. The $Na_v1.6$ somatic nanoclusters could represent regions of localized protein modulation. There is an ever-growing list of $Na_v1.6$ interacting proteins including FGFs and calmodulin (Dib-Hajj and Waxman, 2010). Future studies will investigate the potential protein interactors in regards to differential regulation of channels in the AIS versus the soma. Previous studies have used sodium indicator dyes to probe Na_v channel activity in the AIS versus the soma (Fleidervish et al., 2010). However, sodium dyes have poor spatial and temporal resolution such that activity through a limited number of channels would be undetectable using this method.

As discussed in chapter 2, I have created a $Na_v1.6$ channel construct with a K1411E substitution, rendering the channel Ca^{2+} permeable (Heinemann et al., 1992). The methods to study Ca^{2+} dynamics are much more sophisticated than those for Na^+, and thus can provide much better temporal and spatial resolution. We propose to use the Ca^{2+} indicator Fluo-4 in conjunction with the Ca^{2+} chelator EGTA, which enhances the signal to noise ratio of the Fluo-4, to investigate $Na_v1.6$ activity within the somatic nanoclusters. Initial trials with this technique have proved difficult, particularly with the multitude of endogenous Ca^{2+} signals present in neurons and the fact that the mutant channel is also blocked by a broad range of calcium blockers.

Another related strategy is the use of GCAMP as a reporter for Ca^{2+} flux. The GFP from the Ca^{2+} permeable mutant $Na_v1.6$ channel has been replaced with GCAMP (by Laura Solé) and preliminary experiments have recorded Ca^{2+} flux in both the AIS and soma during spontaneous neuronal activity. Ultimately, we propose to determine the location specific contribution of $Na_v1.6$ somatic nanoclusters to neuronal signaling, determine the protein regulators of such activity, and determine how these are altered in states of disease and neuronal pathophysiology.

5.4 Heterogeneous distribution of $Na_v1.6$ in the AIS

$Na_v1.6$ is important for fast-spiking in some types of neurons because of its persistent and resurgent current, as well as the fact that it is activated at more negative membrane potentials than other isoforms (Rush et al., 2005). It has been proposed, based on electrophysiology studies, that the action potential is initiated in the distal portion of the AIS where the density of $Na_v1.6$ is the greatest (Hu et al., 2009). Another study using Na^+ indicator dyes argued that action potentials initiate beyond the peak density of $Na_v1.6$, perhaps because it is farther away from the large capacitive drain of the somatic membrane. High-resolution studies of Na_v localization and activity are needed to address this question further. The submicron distribution of Na_v channels in the AIS is still unknown. I have used the $Na_v1.6$-Dendra2 construct to investigate precise channel localization and diffusion of axonal $Na_v1.6$ channels. Preliminary data suggests that channels are localized to distinct regions of the AIS with low mobility. I have supported these data using STORM to create super-resolution images of $Na_v1.6$ distribution in the AIS, confirming the non-uniform distribution of $Na_v1.6$ in the AIS.

Future investigations will probe how this submicron distribution of channels influences channel function by combining high-resolution localization techniques with optical measures of

channel activity. Cell-attached patch clamp or excised patches of the AIS membrane have both been criticized since the unique protein packing and cytoskeletal network most likely make it impossible to retain true channel function with the added pressures of a gigaohm seal or cleanly excise a membrane patch (Kole and Stuart, 2008). These factors make optical measures of neuronal function the best strategy. We propose to use the Ca^{2+} permeable $Na_v1.6$ channel in conjunction with Ca^{2+} indicators or GCAMP to investigate channel activity in the AIS with high spatial resolution. Combined with super-resolution images of $Na_v1.6$ localization in the same axon, it would be possible to determine how the subcompartmental distribution of $Na_v1.6$ influences AP initiation and propagation. This would provide insight into the reason for the differential distribution of Na_v isoforms in the AIS.

5.6 Final Remarks

Na_v channels are central to basic physiology and mutations, altered localization, or misregulation of these channels lead to disease. They are important targets of drug therapy, such as anti-arithmetic and anti-epileptic treatments. The research in this dissertation represents the first study of a Na_v isoform at the single-molecule level. By improving our understanding of $Na_v1.6$ channel trafficking, localization, and cell-surface dynamics, these studies have greatly enhanced our knowledge of Na_v neuronal cell biology. We propose that this will provide a basis for understanding altered Na_v localization and misregulation in diseases such as epilepsy and after traumatic brain injury and ischemia. Ultimately, the creation of tagged $Na_v1.6$ channel constructs suitable for high-resolution microscopy studies will enable novel areas of Na_v channel research.

References

Abbe E (1873) Beiträge zur Theorie des Mikroskops und der mikroskopischen Wahrnehmung. Archiv für mikroskopische Anatomie 9:413-418.

Agnew WS, Moore AC, Levinson SR, Raftery MA (1980) Identification of a large molecular weight peptide associated with a tetrodotoxin binding protein from the electroplax of Electrophoruselectricus. Biochemical and biophysical research communications 92:860-866.

Akin EJ, Solé L, Dib-Hajj SD, Waxman SG, Tamkun MM (2015) Preferential Targeting of Nav1. 6 Voltage-Gated Na+ Channels to the Axon Initial Segment during Development. PloS one 10.

Akin EJ, Brown K, Sadegh S, Weigel AV, Masson J-B, Krapf D, Tamkun MM (2014) Single-Particle Tracking Palm of Nav1. 6 in Hippocampal Neurons Demonstrates Unique Subcellular Diffusion Landscapes. Biophysical Journal 106:36a.

Aldrich R, Corey D, Stevens C (1983) A reinterpretation of mammalian sodium channel gating based on single channel recording. Nature 306:436-441.

Amir R, Argoff CE, Bennett GJ, Cummins TR, Durieux ME, Gerner P, Gold MS, Porreca F, Strichartz GR (2006) The role of sodium channels in chronic inflammatory and neuropathic pain. The Journal of Pain 7:S1-S29.

Andrews NL, Lidke KA, Pfeiffer JR, Burns AR, Wilson BS, Oliver JM, Lidke DS (2008) Actin restricts FcεRI diffusion and facilitates antigen-induced receptor immobilization. Nature Cell Biology 10.

Ango F, di Cristo G, Higashiyama H, Bennett V, Wu P, Huang ZJ (2004) Ankyrin-based subcellular gradient of neurofascin, an immunoglobulin family protein, directs GABAergic innervation at purkinje axon initial segment. Cell 119:257-272.

Armstrong CM, Bezanilla F (1973) Currents related to movement of the gating particles of the sodium channels.

Armstrong CM, Bezanilla F (1974) Charge movement associated with the opening and closing of the activation gates of the Na channels. The Journal of General Physiology 63:533-552.

Arnold DB, Gallo G (2014) Structure meets function: actin filaments and myosin motors in the axon. Journal of neurochemistry 129:213-220.

Banks DS, Fradin C (2005) Anomalous diffusion of proteins due to molecular crowding. Biophysical journal 89:2960-2971.

Barchi RL (1983) Protein components of the purified sodium channel from rat skeletal muscle sarcolemma. Journal of neurochemistry 40:1377-1385.

Baroudi G, Acharfi S, Larouche C, Chahine M (2002) Expression and intracellular localization of an SCN5A double mutant R1232W/T1620M implicated in Brugada syndrome. Circulation research 90:e11-e16.

Baroudi G, Pouliot V, Denjoy I, Guicheney P, Shrier A, Chahine M (2001) Novel mechanism for Brugada syndrome defective surface localization of an SCN5A mutant (R1432G). Circulation Research 88:e78-e83.

Barry J, Gu Y, Jukkola P, O'Neill B, Gu H, Mohler PJ, Rajamani KT, Gu C (2014) Ankyrin-G directly binds to kinesin-1 to transport voltage-gated Na+ channels into axons. Developmental cell 28:117-131.

Behrends JC (2012) Evolution of the ion channel concept: The historical perspective. Chemical reviews 112:6218-6226.

Beneski DA, Catterall WA (1980) Covalent labeling of protein components of the sodium channel with a photoactivable derivative of scorpion toxin. Proceedings of the National Academy of Sciences 77:639-643.

Bernstein J (1902) Untersuchungen zur Thermodynamik der bioelektrischen Ströme. Pflügers Archiv European Journal of Physiology 92:521-562.

Bernstein J (1912) Elektrobiologie: Die Lehre von den Elektrischen Vorgangen im Organismus auf Moderner Grundlage Dargestellt.

Biskup C, Zimmer T, Benndorf K (2004) FRET between cardiac Na+ channel subunits measured with a confocal microscope and a streak camera. Nature biotechnology 22:220-224.

Boiko T, Van Wart A, Caldwell JH, Levinson SR, Trimmer JS, Matthews G (2003) Functional specialization of the axon initial segment by isoform-specific sodium channel targeting. The Journal of neuroscience 23:2306-2313.

Brachet A, Leterrier C, Irondelle M, Fache M-P, Racine V, Sibarita J-B, Choquet D, Dargent B (2010) Ankyrin G restricts ion channel diffusion at the axonal initial segment before the establishment of the diffusion barrier. The Journal of cell biology 191:383-395.

Brackenbury WJ, Isom LL (2011) Na+ channel β subunits: overachievers of the ion channel family. Frontiers in pharmacology 2.

Brackenbury WJ, Calhoun JD, Chen C, Miyazaki H, Nukina N, Oyama F, Ranscht B, Isom LL (2010) Functional reciprocity between Na+ channel Nav1.6 and beta1 subunits in the coordinated regulation of excitability and neurite outgrowth. Proc Natl Acad Sci U S A 107:2283-2288.

Brechet A, Fache MP, Brachet A, Ferracci G, Baude A, Irondelle M, Pereira S, Leterrier C, Dargent B (2008) Protein kinase CK2 contributes to the organization of sodium channels in axonal membranes by regulating their interactions with ankyrin G. J Cell Biol 183:1101-1114.

Bréchet A, Fache M-P, Brachet A, Ferracci G, Baude A, Irondelle M, Pereira S, Leterrier C, Dargent B (2008) Protein kinase CK2 contributes to the organization of sodium channels in axonal membranes by regulating their interactions with ankyrin G. The Journal of cell biology 183:1101-1114.

Burgess DL, Kohrman DC, Galt J, Plummer NW, Jones JM, Spear B, Meisler MH (1995) Mutation of a new sodium channel gene, Scn8a, in the mouse mutant 'motor endplate disease'. Nature genetics 10:461-465.

Caldwell JH, Schaller KL, Lasher RS, Peles E, Levinson SR (2000) Sodium channel Nav1. 6 is localized at nodes of Ranvier, dendrites, and synapses. Proceedings of the National Academy of Sciences 97:5616-5620.

Catterall WA (1981) Localization of sodium channels in cultured neural cells. The Journal of Neuroscience 1:777-783.

Catterall WA (1987) Common modes of drug action on Na+ channels: local anesthetics, antiarrhythmics and anticonvulsants. Trends in Pharmacological Sciences 8:57-65.

Catterall WA (2010) Ion channel voltage sensors: structure, function, and pathophysiology. Neuron 67:915-928.

Catterall WA, Kalume F, Oakley JC (2010) NaV1. 1 channels and epilepsy. The Journal of physiology 588:1849-1859.

Catterall WA, Perez-Reyes E, Snutch TP, Striessnig J (2005) International Union of Pharmacology. XLVIII. Nomenclature and structure-function relationships of voltage-gated calcium channels. Pharmacological reviews 57:411-425.

Cesca F, Satapathy A, Ferrea E, Nieus T, Benfenati F, Scholz-Starke J (2015) Functional Interaction between the Scaffold Protein Kidins220/ARMS and Neuronal Voltage-Gated Na+ Channels. Journal of Biological Chemistry 290:18045-18055.

Chahine M, O'Leary ME (2014) Regulation/modulation of sensory neuron sodium channels. In: Voltage Gated Sodium Channels, pp 111-135: Springer.

Chaplin NL, Nieves-Cintrón M, Fresquez AM, Navedo MF, Amberg GC (2015) Arterial Smooth Muscle Mitochondria Amplify Hydrogen Peroxide Microdomains Functionally Coupled to L-Type Calcium Channels. Circulation research:CIRCRESAHA. 115.306996.

Chen I, Howarth M, Lin W, Ting AY (2005) Site-specific labeling of cell surface proteins with biophysical probes using biotin ligase. Nature methods 2:99-104.

Cole KS, Curtis HJ (1939) Electric impedance of the squid giant axon during activity. The Journal of general physiology 22:649-670.

Craner MJ, Newcombe J, Black JA, Hartle C, Cuzner ML, Waxman SG (2004) Molecular changes in neurons in multiple sclerosis: altered axonal expression of Nav1. 2 and Nav1. 6 sodium channels and Na+/Ca2+ exchanger. Proceedings of the National Academy of Sciences of the United States of America 101:8168-8173.

Crill WE (1996) Persistent sodium current in mammalian central neurons. Annual Review of Physiology 58:349-362.

Cummins TR, Sheets PL, Waxman SG (2007) The roles of sodium channels in nociception: implications for mechanisms of pain. Pain 131:243-257.

Cutler PJ, Malik MD, Liu S, Byars JM, Lidke DS, Lidke KA (2013) Multi-color quantum dot tracking using a high-speed hyperspectral line-scanning microscope.

DeCaen PG, Yarov-Yarovoy V, Scheuer T, Catterall WA (2011) Gating charge interactions with the S1 segment during activation of a Na+ channel voltage sensor. Proceedings of the National Academy of Sciences 108:18825-18830.

DeCaen PG, Yarov-Yarovoy V, Zhao Y, Scheuer T, Catterall WA (2008) Disulfide locking a sodium channel voltage sensor reveals ion pair formation during activation. Proceedings of the National Academy of Sciences 105:15142-15147.

Deutsch E, Weigel AV, Akin EJ, Fox P, Hansen G, Haberkorn CJ, Loftus R, Krapf D, Tamkun MM (2012a) Kv2. 1 cell surface clusters are insertion platforms for ion channel delivery to the plasma membrane. Molecular biology of the cell 23:2917-2929.

Deutsch E, Weigel AV, Akin EJ, Fox P, Hansen G, Haberkorn CJ, Loftus R, Krapf D, Tamkun MM (2012b) Kv2.1 cell surface clusters are insertion platforms for ion channel delivery to the plasma membrane. Molecular biology of the cell 23:2917-2929.

Dib-Hajj SD, Waxman SG (2010) Isoform-specific and pan-channel partners regulate trafficking and plasma membrane stability; and alter sodium channel gating properties. Neuroscience letters 486:84-91.

Dib-Hajj SD, Cummins TR, Black JA, Waxman SG (2010) Sodium channels in normal and pathological pain. Annual review of neuroscience 33:325-347.

Dib-Hajj SD, Fjell J, Cummins TR, Zheng Z, Fried K, LaMotte R, Black JA, Waxman SG (1999) Plasticity of sodium channel expression in DRG neurons in the chronic constriction injury model of neuropathic pain. Pain 83:591-600.

Dib-Hajj SD, Black JA, Waxman SG (2009) Voltage-Gated Sodium Channels: Therapeutic Targets for Pain. Pain Medicine 10:1260-1269.

Dotti CG, Sullivan CA, Banker GA (1988) The establishment of polarity by hippocampal neurons in culture. The Journal of neuroscience 8:1454-1468.

Du Y, Huang X, Wang T, Han K, Zhang J, Xi Y, Wu G, Ma A (2007) Downregulation of neuronal sodium channel subunits Nav1. 1 and Nav1. 6 in the sinoatrial node from volume-overloaded heart failure rat. Pflügers Archiv-European Journal of Physiology 454:451-459.

Eaholtz G, Scheuer T, Catterall WA (1994) Restoration of inactivation and block of open sodium channels by an inactivation gate peptide. Neuron 12:1041-1048.

El Beheiry M, Dahan M, Masson J-B (2015) Inferencemap: Mapping of Single-Molecule Dynamics using Bayesian Inference. Biophysical Journal 108:472a.

Fache M-P, Moussif A, Fernandes F, Giraud P, Garrido JJ, Dargent B (2004) Endocytotic elimination and domain-selective tethering constitute a potential mechanism of protein segregation at the axonal initial segment. The Journal of cell biology 166:571-578.

Felts PA, Yokoyama S, Dib-Hajj S, Black JA, Waxman SG (1997) Sodium channel alpha-subunit mRNAs I, II, III, NaG, Na6 and hNE (PN1): different expression patterns in developing rat nervous system. Brain research Molecular brain research 45:71-82.

Fleidervish IA, Lasser-Ross N, Gutnick MJ, Ross WN (2010) Na+ imaging reveals little difference in action potential-evoked Na+ influx between axon and soma. Nature neuroscience 13:852-860.

Fox PD, Haberkorn CJ, Akin EJ, Seel PJ, Krapf D, Tamkun MM (2015) Induction of stable endoplasmic reticulum/plasma membrane junctions by Kv2. 1 potassium channels. Journal of cell science:jcs. 166009.

Fox PD, Haberkorn CJ, Weigel AV, Higgins JL, Akin EJ, Kennedy MJ, Krapf D, Tamkun MM (2013) Plasma membrane domains enriched in cortical endoplasmic reticulum function as membrane protein trafficking hubs. Molecular biology of the cell 24:2703-2713.

Galiano MR, Jha S, Ho TS-Y, Zhang C, Ogawa Y, Chang K-J, Stankewich MC, Mohler PJ, Rasband MN (2012) A distal axonal cytoskeleton forms an intra-axonal boundary that controls axon initial segment assembly. Cell 149:1125-1139.

Garrido JJ, Fernandes F, Giraud P, Mouret I, Pasqualini E, Fache MP, Jullien F, Dargent B (2001) Identification of an axonal determinant in the C-terminus of the sodium channel Nav1. 2. The EMBO journal 20:5950-5961.

Garrido JJ, Giraud P, Carlier E, Fernandes F, Moussif A, Fache M-P, Debanne D, Dargent B (2003) A targeting motif involved in sodium channel clustering at the axonal initial segment. Science 300:2091-2094.

Gasser A, Cheng X, Gilmore ES, Tyrrell L, Waxman SG, Dib-Hajj SD (2010) Two Nedd4-binding motifs underlie modulation of sodium channel Nav1. 6 by p38 MAPK. Journal of Biological Chemistry 285:26149-26161.

Gasser A, Ho TS-Y, Cheng X, Chang K-J, Waxman SG, Rasband MN, Dib-Hajj SD (2012) An ankyrinG-binding motif is necessary and sufficient for targeting Nav1. 6 sodium channels to axon initial segments and nodes of Ranvier. The Journal of Neuroscience 32:7232-7243.

Giannone G, Hosy E, Levet F, Constals A, Schulze K, Sobolevsky AI, Rosconi MP, Gouaux E, Tampé R, Choquet D (2010) Dynamic superresolution imaging of endogenous proteins on living cells at ultra-high density. Biophysical journal 99:1303-1310.

Goldin AL (2001) Resurgence of sodium channel research. Annual review of physiology 63:871-894.

Gorelova N, Seamans JK (2015) Cell-attached single-channel recordings in intact prefrontal cortex pyramidal neurons reveal compartmentalized D1/D5 receptor modulation of the persistent sodium current. Frontiers in neural circuits 9.

Hains BC, Klein JP, Saab CY, Craner MJ, Black JA, Waxman SG (2003) Upregulation of sodium channel Nav1. 3 and functional involvement in neuronal hyperexcitability associated with central neuropathic pain after spinal cord injury. The Journal of Neuroscience 23:8881-8892.

Hallaq H, Yang Z, Viswanathan PC, Fukuda K, Shen W, Wang DW, Wells KS, Zhou J, Yi J, Murray KT (2006) Quantitation of protein kinase A-mediated trafficking of cardiac sodium channels in living cells. Cardiovascular research 72:250-261.

Hamann M, Meisler MH, Richter A (2003) Motor disturbances in mice with deficiency of the sodium channel gene Scn8a show features of human dystonia. Experimental neurology 184:830-838.

Hartshorne R, Catterall W (1984) The sodium channel from rat brain. Purification and subunit composition. Journal of Biological Chemistry 259:1667-1675.

Hartshorne R, Messner D, Coppersmith J, Catterall W (1982) The saxitoxin receptor of the sodium channel from rat brain. Evidence for two nonidentical beta subunits. Journal of Biological Chemistry 257:13888-13891.

Hartshorne RP, Catterall WA (1981) Purification of the saxitoxin receptor of the sodium channel from rat brain. Proceedings of the National Academy of Sciences 78:4620-4624.

Hartshorne RP, Keller BU, Talvenheimo JA, Catterall WA, Montal M (1985) Functional reconstitution of the purified brain sodium channel in planar lipid bilayers. Proceedings of the National Academy of Sciences 82:240-244.

Hedstrom KL, Ogawa Y, Rasband MN (2008) AnkyrinG is required for maintenance of the axon initial segment and neuronal polarity. The Journal of cell biology 183:635-640.

Hedstrom KL, Xu X, Ogawa Y, Frischknecht R, Seidenbecher CI, Shrager P, Rasband MN (2007) Neurofascin assembles a specialized extracellular matrix at the axon initial segment. The Journal of cell biology 178:875-886.

Heinemann SH, Terlau H, Stühmer W, Imoto K, Numa S (1992) Calcium channel characteristics conferred on the sodium channel by single mutations. Nature 356:441-443.

Hell SW, Wichmann J (1994) Breaking the diffraction resolution limit by stimulated emission: stimulated-emission-depletion fluorescence microscopy. Optics letters 19:780-782.

Herzog RI, Cummins TR, Ghassemi F, Dib-Hajj SD, Waxman SG (2003) Distinct repriming and closed-state inactivation kinetics of Nav1. 6 and Nav1. 7 sodium channels in mouse spinal sensory neurons. The Journal of physiology 551:741-750.

Hien Y, Montersino A, Castets F, Leterrier C, Filhol O, Vacher H, Dargent B (2014) CK2 accumulation at the axon initial segment depends on sodium channel Nav1. FEBS letters 588:3403-3408.

Hille B (1967) The selective inhibition of delayed potassium currents in nerve by tetraethylammonium ion. The Journal of general physiology 50:1287-1302.

Hille B (1968) Pharmacological modifications of the sodium channels of frog nerve. The Journal of general physiology 51:199-219.

Hille B (1971) The permeability of the sodium channel to organic cations in myelinated nerve. The Journal of general physiology 58:599-619.

Hille B (1972) The permeability of the sodium channel to metal cations in myelinated nerve. The Journal of general physiology 59:637-658.

Hille B (1975) Ionic selectivity, saturation, and block in sodium channels. A four-barrier model. The Journal of general physiology 66:535-560.

Hille B (2001) Ion channels of excitable membranes: Sinauer Sunderland, MA.

Hinman JD, Rasband MN, Carmichael ST (2013) Remodeling of the axon initial segment after focal cortical and white matter stroke. Stroke 44:182-189.

Hiyama TY, Watanabe E, Ono K, Inenaga K, Tamkun MM, Yoshida S, Noda M (2002) Nax channel involved in CNS sodium-level sensing. Nature neuroscience 5:511-512.

Ho TS-Y, Zollinger DR, Chang K-J, Xu M, Cooper EC, Stankewich MC, Bennett V, Rasband MN (2014) A hierarchy of ankyrin-spectrin complexes clusters sodium channels at nodes of Ranvier. Nature neuroscience.

Hodgkin A, Huxley A (1952a) The components of membrane conductance in the giant axon of Loligo. The Journal of physiology 116:473.

Hodgkin AL, Katz B (1949) The effect of sodium ions on the electrical activity of the giant axon of the squid. The Journal of physiology 108:37-77.

Hodgkin AL, Huxley AF (1952b) Currents carried by sodium and potassium ions through the membrane of the giant axon of Loligo. The Journal of physiology 116:449-472.

Hodgkin AL, Huxley AF (1952c) The dual effect of membrane potential on sodium conductance in the giant axon of Loligo. The Journal of physiology 116:497-506.

Hodgkin AL, Huxley A, Katz B (1952) Measurement of current-voltage relations in the membrane of the giant axon of Loligo. The Journal of physiology 116:424.

Hogan PG, Lewis RS, Rao A (2010) Molecular basis of calcium signaling in lymphocytes: STIM and ORAI. Annual review of immunology 28:491.

Howarth M, Takao K, Hayashi Y, Ting AY (2005) Targeting quantum dots to surface proteins in living cells with biotin ligase. Proceedings of the National Academy of Sciences of the United States of America 102:7583-7588.

Hoze N, Nair D, Hosy E, Sieben C, Manley S, Herrmann A, Sibarita J-B, Choquet D, Holcman D (2012) Heterogeneity of AMPA receptor trafficking and molecular interactions revealed by superresolution analysis of live cell imaging. Proceedings of the National Academy of Sciences 109:17052-17057.

Hu W, Tian C, Li T, Yang M, Hou H, Shu Y (2009) Distinct contributions of Nav1. 6 and Nav1. 2 in action potential initiation and backpropagation. Nature neuroscience 12:996-1002.

Huang B, Babcock H, Zhuang X (2010) Breaking the diffraction barrier: super-resolution imaging of cells. Cell 143:1047-1058.

Hunanyan AS, Alessi V, Patel S, Pearse DD, Matthews G, Arvanian VL (2011) Alterations of action potentials and the localization of Nav1. 6 sodium channels in spared axons after hemisection injury of the spinal cord in adult rats. Journal of neurophysiology 105:1033-1044.

Isom LL, De Jongh KS, Patton DE, Reber BF, Offord J, Charbonneau H, Walsh K, Goldin AL, Catterall WA (1992) Primary structure and functional expression of the beta 1 subunit of the rat brain sodium channel. Science 256:839-842.

Jaqaman K, Loerke D, Mettlen M, Kuwata H, Grinstein S, Schmid SL, Danuser G (2008) Robust single-particle tracking in live-cell time-lapse sequences. Nature methods 5:695-702.

Jenkins SM, Bennett V (2001) Ankyrin-G coordinates assembly of the spectrin-based membrane skeleton, voltage-gated sodium channels, and L1 CAMs at Purkinje neuron initial segments. The Journal of cell biology 155:739-746.

Jones SL, Korobova F, Svitkina T (2014) Axon initial segment cytoskeleton comprises a multiprotein submembranous coat containing sparse actin filaments. The Journal of cell biology 205:67-81.

Kanchanawong P, Shtengel G, Pasapera AM, Ramko EB, Davidson MW, Hess HF, Waterman CM (2010) Nanoscale architecture of integrin-based cell adhesions. Nature 468:580-584.

Kaplan MR, Cho M-H, Ullian EM, Isom LL, Levinson SR, Barres BA (2001) Differential control of clustering of the sodium channels Na v 1.2 and Na v 1.6 at developing CNS nodes of Ranvier. Neuron 30:105-119.

Kellenberger S, Scheuer T, Catterall WA (1996) Movement of the Na+ channel inactivation gate during inactivation. Journal of Biological Chemistry 271:30971-30979.

Kellenberger S, West JW, Catterall WA, Scheuer T (1997a) Molecular analysis of potential hinge residues in the inactivation gate of brain type IIA Na+ channels. The Journal of general physiology 109:607-617.

Kellenberger S, West JW, Scheuer T, Catterall WA (1997b) Molecular analysis of the putative inactivation particle in the inactivation gate of brain type IIA Na+ channels. The Journal of general physiology 109:589-605.

King AN, Manning CF, Trimmer JS (2014) A unique ion channel clustering domain on the axon initial segment of mammalian neurons. Journal of Comparative Neurology 522:2594-2608.

Kohrman DC, Smith MR, Goldin AL, Harris J, Meisler MH (1996) A missense mutation in the sodium channel Scn8a is responsible for cerebellar ataxia in the mouse mutant jolting. The Journal of neuroscience 16:5993-5999.

Kole MH, Stuart GJ (2008) Is action potential threshold lowest in the axon? Nature neuroscience 11:1253-1255.

Kole MH, Letzkus JJ, Stuart GJ (2007) Axon initial segment Kv1 channels control axonal action potential waveform and synaptic efficacy. Neuron 55:633-647.

Kole MH, Ilschner SU, Kampa BM, Williams SR, Ruben PC, Stuart GJ (2008) Action potential generation requires a high sodium channel density in the axon initial segment. Nature neuroscience 11:178-186.

Kraft ML (2013) Plasma membrane organization and function: moving past lipid rafts. Molecular biology of the cell 24:2765-2768.

Kraner SD, Filatov GN, Sun W, Bannerman P, Lindstrom J, Barchi RL (1998) Analysis of Local Structure in the D2/S1–S2 Region of the Rat Skeletal Muscle Type 1 Sodium Channel Using Insertional Mutagenesis. Journal of neurochemistry 70:1628-1635.

Krapf D (2015) Mechanisms Underlying Anomalous Diffusion in the Plasma Membrane. Current topics in membranes.

Kusumi A, Sako Y (1996) Cell surface organization by the membrane skeleton. Current opinion in cell biology 8:566-574.

Kusumi A, Nakada C, Ritchie K, Murase K, Suzuki K, Murakoshi H, Kasai RS, Kondo J, Fujiwara T (2005) Paradigm shift of the plasma membrane concept from the two-dimensional continuum fluid to the partitioned fluid: high-speed single-molecule tracking of membrane molecules. Annu Rev Biophys Biomol Struct 34:351-378.

Lasne D, Blab GA, Berciaud S, Heine M, Groc L, Choquet D, Cognet L, Lounis B (2006) Single nanoparticle photothermal tracking (SNaPT) of 5-nm gold beads in live cells. Biophysical journal 91:4598-4604.

Laude AJ, Prior IA (2004) Plasma membrane microdomains: organization, function and trafficking (Review). Molecular membrane biology 21:193-205.

Lee A, Goldin AL (2009) Role of the terminal domains in sodium channel localization. Channels 3:171-180.

Lemaillet G, Walker B, Lambert S (2003) Identification of a conserved ankyrin-binding motif in the family of sodium channel α subunits. Journal of Biological Chemistry 278:27333-27339.

Leterrier C, Dargent B (2014) No Pasaran! Role of the axon initial segment in the regulation of protein transport and the maintenance of axonal identity. In: Seminars in cell & developmental biology, pp 44-51: Elsevier.

Lippincott-Schwartz J, Patterson GH (2003) Development and use of fluorescent protein markers in living cells. Science 300:87-91.

Liu Z, Lavis LD, Betzig E (2015) Imaging Live-Cell Dynamics and Structure at the Single-Molecule Level. Molecular cell 58:644-659.

Loerke D, Mettlen M, Yarar D, Jaqaman K, Jaqaman H, Danuser G, Schmid SL (2009) Cargo and dynamin regulate clathrin-coated pit maturation.

Lorincz A, Nusser Z (2008) Cell-type-dependent molecular composition of the axon initial segment. The Journal of neuroscience : the official journal of the Society for Neuroscience 28:14329-14340.

Lorincz A, Nusser Z (2010) Molecular identity of dendritic voltage-gated sodium channels. Science 328:906-909.

Malhotra JD, Koopmann MC, Kazen-Gillespie KA, Fettman N, Hortsch M, Isom LL (2002) Structural requirements for interaction of sodium channel beta 1 subunits with ankyrin. The Journal of biological chemistry 277:26681-26688.

Manley S, Gillette JM, Patterson GH, Shroff H, Hess HF, Betzig E, Lippincott-Schwartz J (2008) High-density mapping of single-molecule trajectories with photoactivated localization microscopy. Nature methods 5:155-157.

Mao Q, Jia F, Zhang X-h, Qiu Y-m, Ge J-w, Bao W-j, Luo Q-z, Jiang J-y (2010) The Up-Regulation of Voltage-Gated Sodium Channel NaV1. 6 Expression Following Fluid Percussion Traumatic Brain Injury in Rats. Neurosurgery 66:1134-1139.

Masel BE, Bell RS, Brossart S, Grill RJ, Hayes RL, Levin HS, Rasband MN, Ritzel DV, Wade CE, DeWitt DS (2012) Galveston Brain Injury Conference 2010: clinical and experimental aspects of blast injury. Journal of neurotrauma 29:2143-2171.

Masson J-B, Dionne P, Salvatico C, Renner M, Specht CG, Triller A, Dahan M (2014) Mapping the energy and diffusion landscapes of membrane proteins at the cell surface using high-density single-molecule imaging and Bayesian inference: application to the multiscale dynamics of glycine receptors in the neuronal membrane. Biophysical journal 106:74-83.

Maue RA (2007) Understanding ion channel biology using epitope tags: progress, pitfalls, and promise. Journal of cellular physiology 213:618-625.

Mccutchen CW (1967) Superresolution in microscopy and the Abbe resolution limit. JOSA 57:1190-1190.

Meeks JP, Mennerick S (2007) Action potential initiation and propagation in CA3 pyramidal axons. Journal of neurophysiology 97:3460-3472.

Meisler MH, Kearney JA (2005) Sodium channel mutations in epilepsy and other neurological disorders. Journal of Clinical Investigation 115:2010.

Michalet X, Pinaud FF, Bentolila LA, Tsay JM, Doose S, Li JJ, Sundaresan G, Wu AM, Gambhir SS, Weiss S (2005) Quantum dots for live cells, in vivo imaging, and diagnostics. science 307:538-544.

Mika JT, Poolman B (2011) Macromolecule diffusion and confinement in prokaryotic cells. Current opinion in biotechnology 22:117-126.

Mohler PJ, Rivolta I, Napolitano C, LeMaillet G, Lambert S, Priori SG, Bennett V (2004) Nav1. 5 E1053K mutation causing Brugada syndrome blocks binding to ankyrin-G and expression of Nav1. 5 on the surface of cardiomyocytes. Proceedings of the National Academy of Sciences of the United States of America 101:17533-17538.

Morris CE, Boucher P-A, Joós B (2012) Left-shifted Nav channels in injured bilayer: primary targets for neuroprotective Nav antagonists? Frontiers in pharmacology 3.

Nakada C, Ritchie K, Oba Y, Nakamura M, Hotta Y, Iino R, Kasai RS, Yamaguchi K, Fujiwara T, Kusumi A (2003) Accumulation of anchored proteins forms membrane diffusion barriers during neuronal polarization. Nature cell biology 5:626-632.

Nakamura Y, Nakajima S, Grundfest H (1965) The action of tetrodotoxin on electrogenic components of squid giant axons. The Journal of general physiology 48:985-996.

Narahashi T, Moore JW, Scott WR (1964) Tetrodotoxin blockage of sodium conductance increase in lobster giant axons. The Journal of general physiology 47:965-974.

Narahashi T, Deguchi T, Urakawa N, Ohkubo Y (1960) Stabilization and rectification of muscle fiber membrane by tetrodotoxin. American Journal of Physiology--Legacy Content 198:934-938.

Nernst W (1888) Zur kinetik der in lösung befindlichen körper.

Noda M, Ikeda T, Suzuki H, Takeshima H, Takahashi T, Kuno M, Numa S (1986a) Expression of functional sodium channels from cloned cDNA.

Noda M, Ikeda T, Kayano T, Suzuki H, Takeshima H, Kurasaki M, Takahashi H, Numa S (1986b) Existence of distinct sodium channel messenger RNAs in rat brain.

Noda M, Shimizu S, Tanabe T, Takai T, Kayano T, Ikeda T, Takahashi H, Nakayama H, Kanaoka Y, Minamino N (1983) Primary structure of Electrophorus electricus sodium channel deduced from cDNA sequence. Nature 312:121-127.

Noujaim SF, Kaur K, Milstein M, Jones JM, Furspan P, Jiang D, Auerbach DS, Herron T, Meisler MH, Jalife J (2012) A null mutation of the neuronal sodium channel NaV1. 6 disrupts action potential propagation and excitation-contraction coupling in the mouse heart. The FASEB Journal 26:63-72.

O'Brien JE, Sharkey LM, Vallianatos CN, Han C, Blossom JC, Yu T, Waxman SG, Dib-Hajj SD, Meisler MH (2012) Interaction of voltage-gated sodium channel Nav1. 6 (SCN8A) with microtubule-associated protein Map1b. Journal of Biological Chemistry 287:18459-18466.

O'Connell KM, Tamkun MM (2005) Targeting of voltage-gated potassium channel isoforms to distinct cell surface microdomains. Journal of cell science 118:2155-2166.

O'Connell KM, Rolig AS, Whitesell JD, Tamkun MM (2006) Kv2. 1 potassium channels are retained within dynamic cell surface microdomains that are defined by a perimeter fence. The Journal of neuroscience 26:9609-9618.

Ogawa Y, Rasband MN (2008) The functional organization and assembly of the axon initial segment. Current opinion in neurobiology 18:307-313.

Ohura S, Kamiya H (2015) Excitability tuning of axons in the central nervous system. The Journal of Physiological Sciences:1-8.

Ondrus AE, Hsiao-lu DL, Iwanaga S, Parsons WH, Andresen BM, Moerner W, Du Bois J (2012) Fluorescent saxitoxins for live cell imaging of single voltage-gated sodium ion channels beyond the optical diffraction limit. Chemistry & biology 19:902-912.

Ovesný M, Křížek P, Borkovec J, Švindrych Z, Hagen GM (2014) ThunderSTORM: a comprehensive ImageJ plug-in for PALM and STORM data analysis and super-resolution imaging. Bioinformatics 30:2389-2390.

Pan Z, Kao T, Horvath Z, Lemos J, Sul J-Y, Cranstoun SD, Bennett V, Scherer SS, Cooper EC (2006) A common ankyrin-G-based mechanism retains KCNQ and NaV channels at electrically active domains of the axon. The Journal of neuroscience 26:2599-2613.

Payandeh J, Scheuer T, Zheng N, Catterall WA (2011) The crystal structure of a voltage-gated sodium channel. Nature 475:353-358.

Plummer NW, Galt J, Jones JM, Burgess DL, Sprunger LK, Kohrman DC, Meisler MH (1998) Exon organization, coding sequence, physical mapping, and polymorphic intragenic markers for the human neuronal sodium channel geneSCN8A. Genomics 54:287-296.

Raman IM, Sprunger LK, Meisler MH, Bean BP (1997) Altered subthreshold sodium currents and disrupted firing patterns in Purkinje neurons of Scn8a mutant mice. Neuron 19:881-891.

Rasband MN (2010) The axon initial segment and the maintenance of neuronal polarity. Nature Reviews Neuroscience 11:552-562.

Reinhard K, Rougier J-S, Ogrodnik J, Abriel H (2013) Electrophysiological properties of mouse and epitope-tagged human cardiac sodium channel Na v1. 5 expressed in HEK293 cells. F1000Research 2.

Riedl J, Crevenna AH, Kessenbrock K, Yu JH, Neukirchen D, Bista M, Bradke F, Jenne D, Holak TA, Werb Z (2008) Lifeact: a versatile marker to visualize F-actin. Nature methods 5:605-607.

Ritchie K, Iino R, Fujiwara T, Murase K, Kusumi A (2003) The fence and picket structure of the plasma membrane of live cells as revealed by single molecule techniques (Review). Molecular membrane biology 20:13-18.

ROJAS E, ARMSTRONG C (1971) Sodium conductance activation without inactivation in pronase-perfused axons. Nature 229:177-178.

Rush AM, Dib-Hajj SD, Waxman SG (2005) Electrophysiological properties of two axonal sodium channels, Nav1. 2 and Nav1. 6, expressed in mouse spinal sensory neurones. The Journal of physiology 564:803-815.

Rush AM, Wittmack EK, Tyrrell L, Black JA, Dib-Hajj SD, Waxman SG (2006) Differential modulation of sodium channel Nav1. 6 by two members of the fibroblast growth factor homologous factor 2 subfamily. European Journal of Neuroscience 23:2551-2562.

Rust MJ, Bates M, Zhuang X (2006) Sub-diffraction-limit imaging by stochastic optical reconstruction microscopy (STORM). Nature methods 3:793-796.

Sarmiere PD, Weigle CM, Tamkun MM (2008) The Kv2. 1 K+ channel targets to the axon initial segment of hippocampal and cortical neurons in culture and in situ. BMC neuroscience 9:112.

Schafer DP, Jha S, Liu F, Akella T, McCullough LD, Rasband MN (2009) Disruption of the axon initial segment cytoskeleton is a new mechanism for neuronal injury. The Journal of Neuroscience 29:13242-13254.

Schaller KL, Krzemien DM, Yarowsky PJ, Krueger BK, Caldwell JH (1995) A novel, abundant sodium channel expressed in neurons and glia. The Journal of neuroscience 15:3231-3242.

Schofield GG, Puhl HL, Ikeda SR (2008) Properties of wild-type and fluorescent protein-tagged mouse tetrodotoxin-resistant sodium channel (NaV1. 8) heterologously expressed in rat sympathetic neurons. Journal of neurophysiology 99:1917-1927.

Sharkey LM, Cheng X, Drews V, Buchner DA, Jones JM, Justice MJ, Waxman SG, Dib-Hajj SD, Meisler MH (2009) The ataxia3 mutation in the N-terminal cytoplasmic domain of sodium channel Nav1. 6 disrupts intracellular trafficking. The Journal of Neuroscience 29:2733-2741.

Shimomura O (2009) Discovery of green fluorescent protein (GFP)(Nobel Lecture). Angewandte Chemie International Edition 48:5590-5602.

Shirahata E, Iwasaki H, Takagi M, Lin C, Bennett V, Okamura Y, Hayasaka K (2006) Ankyrin-G regulates inactivation gating of the neuronal sodium channel, Nav1. 6. Journal of neurophysiology 96:1347-1357.

Sieber JJ, Willig KI, Kutzner C, Gerding-Reimers C, Harke B, Donnert G, Rammner B, Eggeling C, Hell SW, Grubmüller H (2007) Anatomy and dynamics of a supramolecular membrane protein cluster. Science 317:1072-1076.

Sigworth FJ (1980) Single Na+ channel currents. Nature 287:447.

Singer S, Nicolson GL (1972) The fluid mosaic model of the structure of cell membranes. Day and Good Membranes and viruses in immunopathology:7-47.

Solé L, Roura-Ferrer M, Pérez-Verdaguer M, Oliveras A, Calvo M, Fernández-Fernández JM, Felipe A (2009) KCNE4 suppresses Kv1. 3 currents by modulating trafficking, surface expression and channel gating. Journal of cell science 122:3738-3748.

St-Pierre F, Marshall JD, Yang Y, Gong Y, Schnitzer MJ, Lin MZ (2014) High-fidelity optical reporting of neuronal electrical activity with an ultrafast fluorescent voltage sensor. Nature neuroscience 17:884-889.

Sun XR, Badura A, Pacheco DA, Lynch LA, Schneider ER, Taylor MP, Hogue IB, Enquist LW, Murthy M, Wang SS-H (2013) Fast GCaMPs for improved tracking of neuronal activity. Nature communications 4.

Susuki K, Rasband MN (2008) Spectrin and ankyrin-based cytoskeletons at polarized domains in myelinated axons. Experimental Biology and Medicine 233:394-400.

Talvenheimo J, Tamkun M, Catterall W (1982) Reconstitution of neurotoxin-stimulated sodium transport by the voltage-sensitive sodium channel purified from rat brain. Journal of Biological Chemistry 257:11868-11871.

Tamkun M, Talvenheimo J, Catterall W (1984) The sodium channel from rat brain. Reconstitution of neurotoxin-activated ion flux and scorpion toxin binding from purified components. Journal of Biological Chemistry 259:1676-1688.

Tamkun MM, O'Connell KM, Rolig AS (2007) A cytoskeletal-based perimeter fence selectively corrals a sub-population of cell surface Kv2. 1 channels. Journal of Cell Science 120:2413-2423.

Tian C, Wang K, Ke W, Guo H, Shu Y (2013) Molecular identity of axonal sodium channels in human cortical pyramidal cells. Frontiers in cellular neuroscience 8:297-297.

Trudeau MM, Dalton JC, Day JW, Ranum LP, Meisler MH (2006) Heterozygosity for a protein truncation mutation of sodium channel SCN8A in a patient with cerebellar atrophy, ataxia, and mental retardation. Journal of medical genetics 43:527-530.

Tsien RY (1998) The green fluorescent protein. Annual review of biochemistry 67:509-544.

Tucker KR, Huertas MA, Horn JP, Canavier CC, Levitan ES (2012) Pacemaker rate and depolarization block in nigral dopamine neurons: a somatic sodium channel balancing act. The Journal of Neuroscience 32:14519-14531.

Van Wart A, Matthews G (2006) Impaired firing and cell-specific compensation in neurons lacking nav1. 6 sodium channels. The Journal of neuroscience 26:7172-7180.

Veeramah KR, O'Brien JE, Meisler MH, Cheng X, Dib-Hajj SD, Waxman SG, Talwar D, Girirajan S, Eichler EE, Restifo LL (2012) De novo pathogenic SCN8A mutation identified by whole-genome sequencing of a family quartet affected by infantile epileptic encephalopathy and SUDEP. The American Journal of Human Genetics 90:502-510.

Waxman SG (2006) Axonal conduction and injury in multiple sclerosis: the role of sodium channels. Nature Reviews Neuroscience 7:932-941.

Weigel AV, Tamkun MM, Krapf D (2013) Quantifying the dynamic interactions between a clathrin-coated pit and cargo molecules. Proceedings of the National Academy of Sciences 110:E4591-E4600.

West JW, Patton DE, Scheuer T, Wang Y, Goldin AL, Catterall WA (1992) A cluster of hydrophobic amino acid residues required for fast Na (+)-channel inactivation. Proceedings of the National Academy of Sciences 89:10910-10914.

Williams SR, Stuart GJ (2000) Action potential backpropagation and somato-dendritic distribution of ion channels in thalamocortical neurons. The Journal of Neuroscience 20:1307-1317.

Wimmer VC, Reid CA, So EYW, Berkovic SF, Petrou S (2010a) Axon initial segment dysfunction in epilepsy. The Journal of physiology 588:1829-1840.

Wimmer VC, Reid CA, Mitchell S, Richards KL, Scaf BB, Leaw BT, Hill EL, Royeck M, Horstmann M-T, Cromer BA (2010b) Axon initial segment dysfunction in a mouse model of genetic epilepsy with febrile seizures plus. The Journal of clinical investigation 120:2661.

Wittmack EK, Rush AM, Hudmon A, Waxman SG, Dib-Hajj SD (2005) Voltage-gated sodium channel Nav1. 6 is modulated by p38 mitogen-activated protein kinase. The Journal of neuroscience 25:6621-6630.

Wu MM, Covington ED, Lewis RS (2014) Single-molecule analysis of diffusion and trapping of STIM1 and Orai1 at endoplasmic reticulum–plasma membrane junctions. Molecular biology of the cell 25:3672-3685.

Xu K, Zhong G, Zhuang X (2013) Actin, spectrin, and associated proteins form a periodic cytoskeletal structure in axons. Science 339:452-456.

Yan H, Pablo JL, Wang C, Pitt GS (2014) FGF14 modulates resurgent sodium current in mouse cerebellar Purkinje neurons. ELife 3:e04193.

Yang Y, Ogawa Y, Hedstrom KL, Rasband MN (2007) βIV spectrin is recruited to axon initial segments and nodes of Ranvier by ankyrinG. The Journal of cell biology 176:509-519.

Zhou D, Lambert S, Malen PL, Carpenter S, Boland LM, Bennett V (1998) AnkyrinG is required for clustering of voltage-gated Na channels at axon initial segments and for normal action potential firing. The Journal of cell biology 143:1295-1304.

Zimmer T, Biskup C, Bollensdorff C, Benndorf K (2002a) The b1 subunit but not the b2 subunit colocalizes with the human heart Na+ channel (hH1) already within the endoplasmic reticulum. Journal of Membrane Biology 186:13-21.

Zimmer T, Biskup C, Dugarmaa S, Vogel F, Steinbis M, Böhle T, Wu Y, Dumaine R, Benndorf K (2002b) Functional expression of GFP-linked human heart sodium channel (hH1) and subcellular localization of the a subunit in HEK293 cells and dog cardiac myocytes. Journal of Membrane Biology 186:1-12.